Reaction Chemistry at the Plasma-Liquid-Solid Interface

Dissertation

zur Erlangung des Grades
"Doktor der Naturwissenschaften"

an der Fakultät für Physik und Astronomie
der Ruhr-Universität Bochum

von
Pia-Victoria Pottkämper
aus Krefeld

Bochum 2026

1. Gutachter: Prof. Dr. Achim von Keudell
2. Gutachter Prof. Dr. Judith Golda

Datum der Disputation: .....

This work was funded by the German Research Foundation (DFG) as part of the Collaborative Research Center (CRC) 1316, "Transient Atmospheric Plasmas: From Plasmas to Liquids to Solids", within subproject B7, "Reaction Chemistry of Plasmas in Liquids interacting with Surfaces".

Contents

1 Introduction

1.1 Motivation

The emission of carbon dioxide into the atmosphere as a waste product of many industrial applications is a known source of pollution, which massively contributes to climate change [1]. A lot of research is dedicated to finding solutions to convert this volatile species into industrially useful products, such as methane and ethylene [2, 3]. The CO_2 reduction Reaction (CO_2RR) is a process, in which carbon dioxide is split into its constituents and then processed into more complex hydrocarbons and alcohols such as ethylene or ethanol. It is therefore the focus of many research projects [4, 5, 6]. Typically, this reaction is performed in an electrolyser, where CO_2 is introduced in gaseous form into a reactor filled with an electrolyte [2]. During the conversion process, corrosion occurs at the electrode surface. To achieve a high reaction rate, catalysts are needed in these processes. One widely used catalyst for this purpose is copper and its oxides [4, 7]. They can be introduced into the system in the form of solvated nanoparticles or bound to a conductive surface where a voltage can be applied.
The catalytic ability and selectivity of these copper oxides is dependent on many factors, such as their size, shape and oxygen content [7, 8]. Cubic copper oxide particles, for instance, exhibit a high selectivity towards ethylene production [9]. Since the CO_2 reduction reaction is catalysed by chemisorption of the CO_2 onto the catalytic surface, the surface morphology and roughness are also of importance [3]. The catalytic effect can also be influenced by tuning the size of the nanostructures, referred to as the catalytic particles size effect [3], especially at sizes below 10 nm [10].
One challenge of these electrochemical reactors is that the definitive efficiency and selectivity of the catalysts depletes over time [11, 12]. The catalysts undergo a multi-step restructuring process, that consists of surface reduction, re-depositioning of material and volume loss [12]. The copper nanostructures gradually decrease in size, affecting their catalytic properties [13]. Therefore, replacement of copper oxide catalysts during the long term operation of a CO_2RR reactor is necessary. To avoid this, a method is needed to re-activate the catalysts, preferably directly inside the reactor. In-liquid plasmas may serve as a tool to achieve the re-activation of such copper oxide catalysts.

In-liquid plasmas have many applications, such as wastewater treatment [14, 15, 16], plasma medicine [17], water purification [18] or manufacturing and decomposing of chemical compounds [19], as they are a flexible tool to initiate (electro-)chemical reactions in a liquid with a wide range of properties. Many different experimental configurations and operational modes exist, depending on their application [20]. They can, for example, be constructed in a pin-to-pin or pin-to-plane configuration, to which a voltage with different temporal characteristics such as AC, DC or pulsed can be applied [21]. The chemical composition of the treated liquid is changed by the plasma treatment. The liquid is then referred to as plasma activated liquid (PAL).

In this work, the plasma is operated in a pulsed mode, where the plasma propagates through the liquid in the form of streamer-like plasma channels. A distinction is made between pulses in the microsecond and nanosecond range. When the rise time of the voltage pulse is in the range in microseconds, Joule heating of the liquid is induced and the plasma is able to ignite within the bubbles inside the gas phase [22]. When a shorter pulse in the nanosecond range is applied, the plasma ignites directly inside the liquid [23]. A broad selection of reactive species, such as solvated electrons, molecular oxygen or hydrogen is created in the system [24]. In-between voltage pulses, those short-lived species undergo different recombination and decomposition reactions [25]. The short-lived species recombine into more long-lived compounds, such as hydroxide or hydrogen peroxide, resulting in a chemically complex activated liquid. Many of the plasma-created compounds are able to reduce or oxidize a metal surface such as copper [26]. Therefore, an in-liquid plasma may be a useful tool to produce a suitable copper oxide catalyst for the CO_2 reduction reaction or reactivate such a copper catalyst. The introduction of a plasma into a CO_2RR reactor may prolong the lifetime of the catalyst and optimize production rate of the products in this way. In this thesis, a method of production of copper oxides through in-liquid plasma is explored by investigating the reaction chemistry at the plasma-liquid-solid interface.

1.2 Research Questions

In this thesis, the interaction between the in-liquid plasma, the chemically activated liquid medium and solid copper is investigated. As the plasma activated liquid is a complex medium, it needs to be characterized to determine its suitability for an electrochemical application. A pulsed in-liquid plasma is used in this work. This pulsed operational mode introduces many possibilities for variation of the plasma properties and optimization of the liquid chemistry. The plasma characteristics such as applied voltage, frequency, pulse length and treatment time have an influence on the liquid chemistry. In particular, the plasma can be operated using voltage pulses with lengths in the microsecond range and in the nanosecond range. The ignition mechanisms differ for these two operational modes and incite different liquid properties. All these factors lead to the first research question:

1. Which chemical properties does the liquid treated by an in-liquid plasma possess and under which conditions is the production of reactive species in the liquid maximized?

The plasma and the plasma-activated liquid are supposed to induce changes on a copper surface. The reactive species produced by the plasma have varying lifetimes because of their different reactivities. Some species quickly react and decompose and therefore exhibit a limited ability to have an influence on the copper surface. Others posses lifetimes in the range of hours and may react with the copper surface on longer timescales. The chemical reactions triggered by the PAL are also diverse, as some of them are oxidizing agents and some are reducing agents. For this reason, a differentiation is made between direct plasma treatment, where the metal is placed in the vicinity of the plasma, and indirect plasma treatment, where the metal only comes into contact with the previously treated liquid. During the direct treatment, short lived species are continuously produced and are able to react with the copper. When the plasma treatment ends, the more stable, long-lived species remaining are able to induce chemical reactions. In this way, the effect of the long-lived reactive species can be separated from the effect of the short-lived species. The second and third research questions are expressed as follows:

2. How does the in-liquid plasma affect the oxidative state and morphology of a copper surface?

3. How does the effect of direct plasma treatment differ from the effect induced by indirect treatment using only plasma-activated liquid?

Many groups have studied the constituents of PAL in the past [21, 24, 27] and some of the individual compounds of the plasma-activated liquid can arguably be produced by more straightforward means than plasma treatment. Chemical compounds such as hydrogen peroxide can be easily be diluted to the desired concentration. For a practical application in an electrochemical system, the question arises whether the plasma actually has advantages over these more simple approaches. This leads to the final research question:

4. Does a liquid medium with similar chemical composition as the PAL, such as a solution of the individual chemical compounds, have the same effect on the copper as the plasma treatment or PAL treatment?

The answers to these questions lead to a better understanding of the complex interactions between in-liquid plasmas and metals. In the future, they may serve as a foundation for implementing an in-liquid plasma into an electrochemical system for an industrial application.

2 Fundamentals

In the following chapter, the theoretical background of the underlying physical concepts of this work is presented. First, an introduction on in-liquid plasmas is given. Many different discharges in and in contact with liquids have been developed and explored for different applications [21]. In this thesis, the focus is placed on pulsed discharges in liquids. A distinction is made between pulsed operation with long and short pulse durations. The former have pulse durations in the range of microseconds, and the later in the range of nanoseconds. The application of in-liquid plasmas in the context of plasma electrolysis is also discussed. Then, the chemistry induced by a plasma and chemical properties of plasma-activated liquid are described. Next, the physical and chemical properties of copper and different oxidation and reduction mechanisms induced by liquids are discussed. Many different factors such as chemical composition, temperature and pH value of the (plasma-activated) liquid, but also the composition of the copper samples, age and storage conditions all have an influence on the oxidation mechanism and surface structure. Lastly, the theoretical background of the different diagnostic methods used to obtain the experimental results of this work are presented. This section includes a description of Fourier Transformed Infrared Spectroscopy (FTIR), Cyclic Voltammetry (CV) and X-ray Photoelectron Spectroscopy (XPS).

2.1 Characterization of In-Liquid Plasmas

The interactions between plasmas and liquids have been widely studied and numerous different experiment configurations have been established by many research groups over time, depending on application and research goal [19, 28]. An effort has been made by Bruggeman et al. [21] to define some categories for the different configurations and some common types relevant for this work are shown in figure 1:

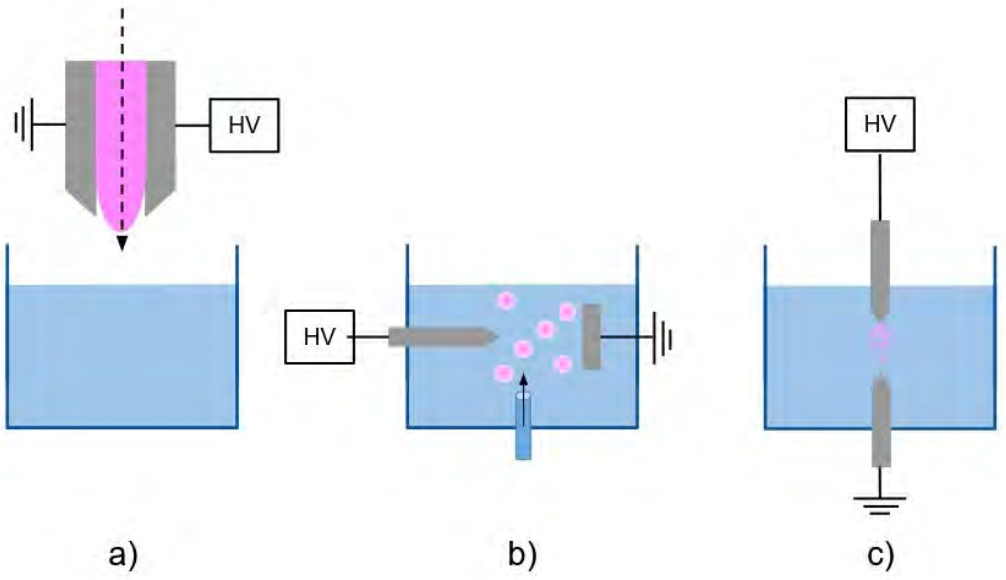

Figure 1: Schematic Overview of different discharge configurations in contact with liquids: a) plasma jet above liquid b) discharge within gaseous bubbles c) discharge directly inside the liquid.

The most commonly implemented method to transform a liquid using a plasma is to create a gaseous discharge and place it above the liquid surface. Many approaches for this method exist, but one popular device is a plasma jet, as shown in figure 1 a). In this application, the plasma is ignited along a gas flow between two electrodes. The plasma can be ignited by applying voltages with varying excitation frequencies, depending on the application [29]. The tip of the jet is placed at a distance to the liquid so the plasma does not come into contact with the liquid surface, but reactive species produced in the discharge are transported to the surface by convection. The reactive species interact with, and can be absorbed by, the liquid. In this manner, a chemically complex and reactive liquid is produced. In this work, it is referred to as plasma activated liquid (PAL) or plasma activated water (PAW).

Due to the electrode configuration of the plasma jet, the ions formed in the plasma are confined between the electrodes of the jet and only neutral species are able to interact with the liquid [21]. To increase the transport efficiency and variety of reactive species to the PAL, the plasma can also be ignited inside the liquid. In-liquid plasmas are commonly ignited in a pin-to-pin or pin-to-plate configuration.

The electrodes are submerged in the liquid and a voltage is applied. The voltage waveform depends on the target application and an in-liquid plasma can principally be operated in an AC, DC or pulsed mode. In the case of pulsed plasmas, as investigated in this work, the distinction is made between discharge in a bubble, as shown in figure 1 b) and a discharge directly inside the liquid figure 1 c). Bubbles can be created by either guiding a gas into the liquid or by evaporating the liquid itself by Ohmic heating. This can be achieved by applying a voltage to the electrode on a timescale sufficient for the evaporation of the medium. The plasma ignites in the gas bubbles and the reactive species created from the plasma dissolve into the liquid. The transport efficiency is higher in this case, since the contact area of the bubbles to the liquid is larger and the distance between plasma and liquid is smaller than in the jet configuration. To ignite a plasma directly inside a liquid, heating and consequent bubble formation need to be avoided. This can be achieved by operating the plasma in a pulsed mode with sufficiently short voltage pulses. In this work, the distinction is made between pulsed in-liquid plasmas operated on a microsecond and a nanosecond timescale, corresponding to the ignition in bubbles and directly in the liquid, respectively. In the following section, these two operational modes are described in more detail.

2.1.1 Pulsed In-Liquid Plasmas and their Ignition Mechanisms

For voltage pulses with rather slow rise times, microsecond pulses are needed to reliably ignite the plasma. Typically, these plasmas are generated by discharging a capacitor [20]. Two ignition mechanisms are generally accepted. The first is based on the assumption, that the long high voltage pulse causes Joule heating of the liquid surrounding the electrode tip which initiates evaporation [21]. The other widely accepted mechanism is based on pre-existing bubbles or impurities in the liquid [30]. Once gaseous bubbles are present in the vicinity of the electrode tip, the Paschen criterion is reached and a plasma ignites in the gas phase. Afterwards, the bubble expands further and a streamer-like gas channel is formed which propagates through the medium, by transferring from bubble to bubble. The molecules of the liquid and gas dissociate and a wide range of dissolved reactive species with different lifespans are created. The formation of bubbles has been found to have an effect on the electrical breakdown, especially over longer operation times [31]. In water, a high electric field is needed for an ignition, if the plasma is ignited in an electrolyte with higher conductivity lower voltages can be sufficient [20].

Nanosecond pulses are typically too short to cause the necessary Joule heating for vapour formation, therefore a plasma is ignited directly inside the liquid [21, 32]. The exact ignition mechanism for nanosecond plasmas has not been sufficiently understood yet. Two prevalent theories exist currently: the ignition via field effects and the ignition via nanovoids resulting from electrostriction.

The cavitation theory is based on the assumption, that the surface tension at the electrode tip is changed when a voltage is applied. Dielectric liquids, such as pure water, experience electrostriction when in contact with a non-uniform electric field, as it forms at a pin-shaped electrode [33]. The electric field gradient is highest at the electrode tip and the ions from the water start following the electric field in this region. This leads to low density regions, so-called nanovoids or microcavities form in close proximity to the electrode tip. These nanovoids are not to be confused with bubbles, as they are ruptures in the liquid and not gas-filled. The electric field gradient then cause the voids to elongate along the field lines [34, 35]. Electrons within the nanovoids are accelerated by the electric field and are able to ionize. The ignition by cavitation is limited by the rise time of the pulse, as on longer timescales the hydrodynamic forces in the liquid dominate and counteract the formation of the voids [35].
The other widespread theory for the ignition process is based on field emission or field ionization [36], depending whether a positive or negative voltage is applied. In case of a positive potential, electrons tunnel from the liquid in the direct vicinity of the electrode into the electrode tip, leaving an excess of positive ions behind. At the same time the electric field ionizes the water and free electrons move towards the electrode heating the liquid locally [37]. In case of a negative potential, the electrons in turn tunnel out of the electrode, ionizing the water molecules and creating negative ions. One finding in favour of this ignition theory is the fact, that the electron densities at ignition differ between positive and negative voltage [37]. Due to the high electric field gradient, the ionization front is able to propagate through the liquid.

The pulsed in-liquid plasmas are able to propagate through the medium. They can be divided into different categories, based on their physical properties [31]. The categories are depicted in figure 2.

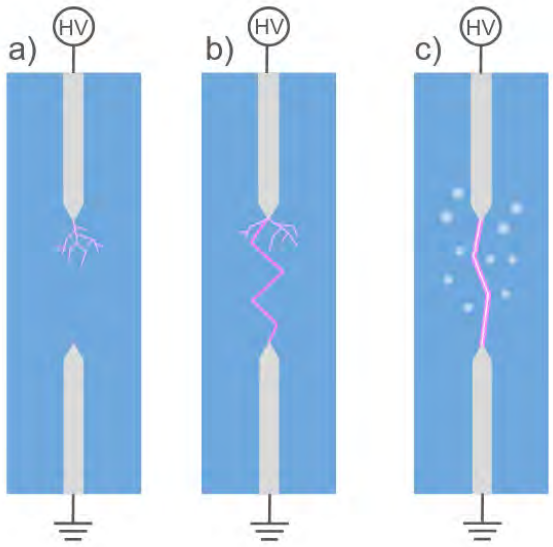

Figure 2: Schematic visualisation of the discharge modes of a pulsed in-liquid plasma. The plasma can be categorized as a streamer-like discharge a), a spark discharge b) and an arc discharge c) [31].

a) In a **streamer-like discharge**, a small luminous discharge channel is formed at the electrode tip. The plasma does not extend far into the medium. The streamer-like discharge is typically produced by an energy pulse of 1 J/pulse [38]. In this discharge mode, the current is transported by ions [39]. At lower voltages, slow streamers, also called primary streamers, with propagation velocities of 100 m/s -1 km/s have been observed, while at higher voltages fast streamers, or secondary streamers, with velocities of 10 - 100 km/s can form [20]. The length of the fast streamers is also larger than of the slow streamers and their length increases with increasing voltage. When the plasma is ignited, a pressure wave is emitted traversing through the liquid.

b) When the filamentary streamer reaches from the driven electrode to the grounded electrode, a transition into a **spark discharge** occurs. This results into a conductive channel connecting the two electrodes [31]. The transition between streamer mode and spark mode occurs abruptly and is dependent on many factors

such as applied voltage, pulse length, electrode distance and conductivity of the liquid medium [20]. In the spark discharge mode, the current is transported by electrons [39]. Once the discharge transitions into a spark, the resistance between the electrodes rapidly decreases, which results in a drop in voltage and an increase in current [20]. The formation of a spark can be provoked by decreasing the distance between the electrodes. The plasma channel is not in a fixed location and quickly disperses after ignition, reforming in a new location with every applied voltage pulse. The streamer-like discharge and spark discharge are also able to form simultaneously [39].

c) In a pulsed **arc discharge**, again filaments form at the driven electrode and a channel is formed between the electrodes. However, in this case the discharge is maintained for longer periods of time and the discharge channel maintains its position. A long pulse duration is needed to achieve an arc discharge. The energy needed for this discharge mode lays in the range of 1 kJ/pulse [38]. The arc discharge generates high electron densities [40] and emits a high amount of UV light and a large amount of thermal energy, which is advantageous in many applications, such as wastewater treatment [16, 39]. For this reason, it is considered a thermal [20] or almost thermal plasma [39].

Both ignition mechanisms discussed above, the ignition via field effects and the ignition via nanovoids have one commonality: for ignition to be possible, a certain threshold of electric field strength needs to be surpassed. The field strength depends on the applied voltage per electrode radius, therefore it is advantageous to choose an electrode with the smallest possible diameter and apply a high voltage. In addition, the conductivity of the liquid is a limiting factor [41]. If the medium is too conductive, the electric field is not able to be established before the charges can traverse the liquid. In this case, no plasma can ignite. Of course, electrons emitted into the liquid are still able to trigger chemical reactions as they do in the in-liquid plasma. This process is referred to as electrolysis. Since the liquid chemistry induced by the in-liquid plasma and electrolysis are similar, understanding the underlying process is crucial to this work and the physical background of electrolysis is described in the following section.

2.1.2 Plasma Electrolysis

In common electrolysis, a two-electrode configuration is typically used. Both electrodes are submerged in an electrolyte and a low voltage is applied, commonly in DC mode. At both electrodes, the cathode and the anode, chemical reactions occur due to charge transfer. The water molecules dissociate and positively and negatively charged species, cations and anions, migrate through the liquid to their respective electrodes. The two half reactions at the anode and cathode depend on the acidity of the liquid. In an acidic aqueous medium, the two half reactions are:

$$\mathrm{H_2O} \longrightarrow \frac{1}{2}\,\mathrm{O_2} + 2\,\mathrm{H^+} + 2\,\mathrm{e^-}\,(\text{Anode}) \tag{1}$$

$$2\,\mathrm{H^+} + 2\,\mathrm{e^-} \longrightarrow \mathrm{H_2}\,(\text{Cathode}) \tag{2}$$

The first is an oxidation reaction, the second a reduction reaction. The complete reaction that takes place in electrolysis is the water splitting reaction [42]:

$$2\,\mathrm{H_2O} \longrightarrow 2\,\mathrm{H_2} + \mathrm{O_2} \tag{3}$$

The voltage needed to trigger the water splitting is called decomposition voltage. At higher voltages, the reaction rates increase and an overpotential is reached. Typically, a voltage of 1.23 V is needed to split water molecules by electricity [43]. This process can be performed in a broad range of aqueous solutions. When an electrolyte is introduced into water, it too undergoes decomposition reactions and a variety of chemical species can be produced by this method. The anode is often dissolved during the electrolysis process, as it undergoes oxidation and is more susceptible to corrosion. In addition to chemical species, particles from the anode material can be produced.

Another application of electrolysis is the modification of metal workpieces by placing them in the electrolyser between the anode and cathode. The process is depicted in figure 3. As a voltage is applied to the working electrode, an electric field is created, that decreases linearly across the solution [44]. This is called the solution potential. Along this potential, the workpiece is placed. A current within the workpiece occurs, which induces the two half reactions at its edges, analogous to the electrolysis process described above [45].

The work piece undergoes both a reduction and an oxidation on either side and different reactive species form in these areas, oxygen at the anode and hydrogen at the cathode [45]. For this reason, this technique is called bipolar electrolysis and the workpiece a bipolar electrode.

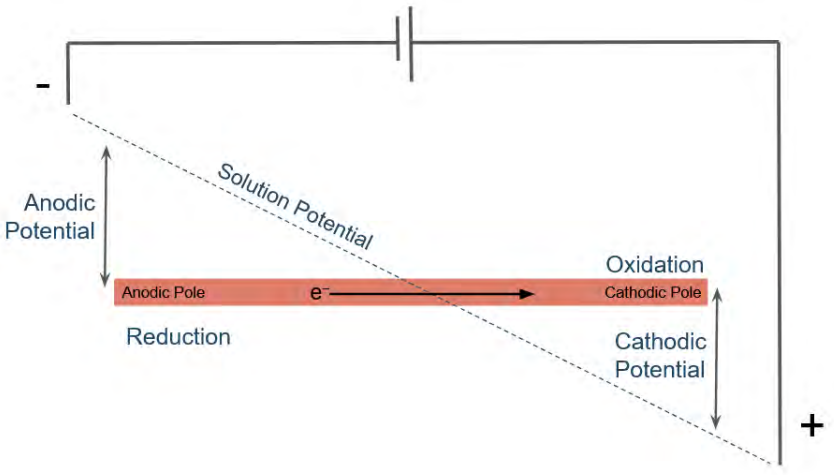

Figure 3: Visualisation of the bipolar electrolysis process. The bipolar electrode undergoes reduction on one side and oxidation at the other. Sketch based on [45].

The yield of reactive species during electrolysis is described by Faradays first law of electrolysis, which states that the molar amount of a product of electrolysis is proportional to the current passing through the cell:

$$m \propto Q. \tag{4}$$

This is a limiting factor of this methods productivity. However, heating and bubble formation also occur during electrolysis. By increasing the voltage to reach the Paschen criterion in the gas phase of these bubbles, a plasma can be ignited and the chemical yield is increased [22]. This method is named **plasma electrolysis** or glow-electrolysis. Plasma electrolysis is known to enhance the effects of the common electrolysis technique [46]. Hereby, the breakdown voltage, and therefore the transition point from classical electrolysis to plasma electrolysis is dependent on the conductivity of the electrolyte. Higher conductivities lead to a breakdown at lower voltages, since the higher current causes greater Joule heating, increased bubble formation and therefore ignition in the gas phase [22].

2.2 Chemistry of Plasma Activated Liquid

The liquid in which the plasma is ignited is fundamentally changed by the treatment. Many liquids used for in-liquid plasma treatment, especially those for biomedical applications are water-based [17], and hence are the focus of this work. In such aqueous solutions, many reactive species are created by the plasma breaking down the water molecules [22].
The reactive species of the in-liquid plasma treatment can be broadly divided into two categories: short- and long-lived. The former are very reactive and have a half-lives below $1s$, depending on liquid properties such as temperature and pH [17]. They are therefore not able to accumulate in the PAL but rather reach a steady state concentration during treatment [25]. Some common short-lived molecules found in PAL are hydrogen, atomic oxygen and molecular oxygen [47].
The short-lived species quickly recombine to more long-lived species via a wide range of reactions. The latter are less reactive and thus have much longer lifetimes and are able to accumulate in the solution. The most long lived species produced from aqueous solutions by the plasma is hydrogen peroxide. When stored properly, this species can remain detectable inside the solution for a long time depending on the initial concentration.

The breakdown of an aqueous solution by in-liquid plasma is more complicated than that in a common electrolysis system, since the voltage applied is much greater than the decomposition voltage. The chemical reactions in the plasma zone are temperature and pressure dependent. A prevalent approach to understand the species production is to distinguish between a core region and a recombination region of the streamer-like discharge [21, 24]. In the hot core region the water molecules are broken down, initiated by high energy electrons produced by the plasma. The electrons are able to dissociate water molecules into their constituents, atomic hydrogen and oxygen [20, 24]. It has been found, that the majority of the produced hydrogen is formed in this region [24]. Some dominant reactions breaking down the water include [25]:

$$H_2O + e^- \longrightarrow H_2O^* + e^- \tag{5}$$

$$H_2O + e^- \longrightarrow H^+ + OH^- e^- \tag{6}$$

$$H_2O^* + H_2O \longrightarrow H + OH + H_2O \cdot \tag{7}$$

In this way, the water molecules are both split and excited and the short-lived species are created. After breakdown of the water molecules, recombination reactions take place in the colder recombination region [25]:

$$H_2 + O \longrightarrow OH + H \tag{8}$$

$$O + OH \longrightarrow O_2 + H \tag{9}$$

$$H + H_2O^* \longrightarrow H_2 + OH \tag{10}$$

$$H^- + H_2O^+ \longrightarrow H_2 + OH\cdot \tag{11}$$

The produced species are also able to diffuse into the bulk of the liquid [48]. As is evident from the dominant reactions displayed above, a prominent reactant and product of the system is hydroxide. This very reactive, short-lived compound is involved in creating the most stable, long-lived species found in the PAL: hydrogen peroxide [48]. Especially reaction 12 is the dominant reaction process in which H_2O_2 is formed [24, 49]. It is a third body reaction, where the collision partner M is typically a water molecule [48]. In addition, back-reactions of the species resulting in water also exist in the system:

$$OH + OH + M \longrightarrow H_2O_2 + M \tag{12}$$

$$O + OH \longrightarrow H_2O \tag{13}$$

$$OH + OH \longrightarrow H_2O + O \tag{14}$$

$$OH + H_2O^* \longrightarrow H + H_2O_2\cdot \tag{15}$$

In short, the in-liquid plasma process results in a plasma activated, reactive liquid, containing an abundance of different species, such as H_2, O_2, OH, and H_2O_2 [47].

The detection and distinction of the species is challenging, and many techniques would need to be employed to characterize the PAL fully. An advantageous quality of the short-lived species is that many of them are ionised, leading to a change in pH in the treated solution. Typically, a decrease in pH is reported [17]. The pH is one property that can easily be detected, which is necessary because the stability of the reactive species in the PAL is also dependent on the pH of the solution. For example, hydrogen and H_2O_2 are more stable in acidic environments, where as OH is more stable in alkaline media [22]. An increase in pH over longer treatment times may therefore be

disadvantageous, if the goal is to produce a large amount of H_2O_2.

Another crucial factor for the composition of the plasma activated liquid is the temperature of the solution, since the formation and lifetime of the reactive species is dependent on it. Both short- and long-lived species decay via many chemical reactions. For example it has been found, that hydrated electrons decay via reactions with H, OH and H_2O_2 [50]:

$$e^-_{aq} + H + H_2O \longrightarrow H_2 + OH^- \tag{16}$$

$$e^-_{aq} + OH \longrightarrow OH^- \tag{17}$$

$$e^-_{aq} + H_2O_2 \longrightarrow OH + OH^- \cdot \tag{18}$$

The rate constants of all three mechanisms increase with temperature, meaning that the reactions are accelerated [51]. This would result in the increase in the successive reactions and a higher concentration of especially the long-lived species. This is not the case for the decomposition of H_2O_2, which decomposes via the following process [52]:

$$H_2O_2 + (M) \longrightarrow 2\,OH + (M) \tag{19}$$

$$OH + H_2O_2 \longrightarrow H_2O + HO_2 \tag{20}$$

$$OH + HO_2 \longrightarrow H_2O + O_2. \tag{21}$$

The first step is a thermal decomposition reaction [51] where the collision partner M is again H_2O [52]. The half-life of this decomposition of H_2O_2 decreases with temperature. At 150°C the half-life lays in the range of a few minutes [53]. It has been found, that the H_2O_2 concentration in solution decreases more steeply at higher temperatures [52]. To produce a reactive liquid with a high concentration of H_2O_2, the temperature can not be neglected, but needs to be kept relatively low. In practice, a stabilizer is introduced into the solution to increase the longevity of the H_2O_2.

In this work, the in-liquid plasma also has been ignited in aqueous solutions containing a base, namely KOH. The introduction of an electrolyte into the system has an impact on ignition and increases the number and complexity of chemical reactions in the liquid. The electrolyte KOH is split by the plasma treatment and forms potassium ions. Potassium ions posses a high ionic conductivity and therefore are able to transport a greater electrical charge. This is why KOH solutions are commonly used as electrolyte in conventional electrolysis. Additionally, potassium hydroxide lowers the overpotential necessary for water splitting and increases the efficiency of the hydrogen production in this way. Unfortunately, an increase in conductivity and a lower overpotential may facilitate the electrolysis process, but hinder the plasma ignition simultaneously. The introduction of the alkaline KOH also impacts the chemical composition of the plasma treated liquid and the lifetimes of the reactive species, as described above.

2.3 Needle Electrode Erosion of Pulsed In-Liquid Plasmas

Another element that adds to the complexity of plasma activated liquid is the corrosion of the electrode material. Many groups have observed the destruction of the driven electrode and have investigated the corrosion process and the dissolution of the material into the liquid [28, 38, 54]. Multiple factors have been found to influence the erosion, such as electrode material, electrode shape, conductivity of the liquid medium and electrical discharge properties. It is assumed, that the dominant effect leading to the corrosion of the material is a thermal process [28, 55]. Therefore, a material with high thermal stability, such as tungsten, is typically chosen as the electrode material. Tungsten possess a melting point of 3695 K and a boiling point of 6203 K and is well suited for this application.
Due to the localized high electric field at a pin-shaped electrode, plasma ignition and subsequent heating of the electrode are also highly localized [56]. After plasma operation, characteristic structures can be found on the surfaces of the electrodes that are associated with different corrosion mechanisms [28]. Often times, crater-like structures form on the electrode [57]. In case of a tungsten electrode, small protrusions have been observed [38, 54]. This has led to the assumption, that the local melting of the material results in a small area of liquefied metal, a so-called hot spot, that is expelled into the liquid medium in form of a metal vapour. The metal vapour then condensates into particles [28].

It has been found, that the erosion of the electrode material increases with time and solution conductivity [38]. The corrosive effect of the in-liquid plasma can be exploited for intentional nanoparticle production [48, 58]. Many groups have investigated different metals and alloys such as platinum, iron, titanium, gold and copper [28, 59].

The electrode material also has an influence on the liquid chemistry, especially in regards to the stability of hydrogen peroxide. In the presence of tungsten, the H_2O_2 acts as an oxidizing agent, causing formation and dissolution of tungsten oxides [60]. This consequently accelerates the decomposition of the H_2O_2. The production efficiency and stability of hydrogen peroxide in plasma activated water in the presence of tungsten nanoparticles was investigated by multiple groups [54, 57, 61] and it has been found, that the tungsten acts as a catalyst in the H_2O_2 decomposition. A plateau in the H_2O_2 concentration after long operation times has been found by multiple groups [57, 61], which has been attributed to the production mechanism and loss mechanism equalizing. This has not been observed when other materials were used. The use of a tungsten electrode in an in-liquid plasma experiment therefore influences the reactivity and chemical composition of the produced PAW.

To conclude, the liquid chemistry of the plasma-treated liquids is very complex and many factors play a role in its composition at any given time. Since this work deals with the influence of in-liquid plasmas on copper, the following section discusses the impact such a complex liquid may have on a copper surface.

2.4 Oxidation and Reduction of Copper

Copper oxides have a wide range of applications, catalysis of carbon dioxide reduction for instance [4, 11]. In this electrolysis process, CO_2 is converted into more useful hydrocarbons, such as methane or ethylene [8]. The selectivity of the catalysts towards a desired product is dependent on the oxide content and its nanostructure. The size and morphology of copper oxide structures play a critical role [3]. Many methods exist for manufacturing of copper oxide catalysts, such as electrochemical synthesis or thermal oxidation of bulk copper. Depending on the chosen method, the resulting oxides differ in their morphology and properties.

When copper oxides are used as catalysts, the oxygen content of copper decreases, which in turn decreases the activity and selectivity of the catalyst. Therefore, copper oxides have a limited lifetime in this application. An in-liquid plasma application may solve this by (re-)oxidizing a catalyst in-situ during the process. In this work, copper films with thicknesses ranging between $10 - 200$ nm are explored as a precursor for such oxide crystals. Depending on the conditions, both bulk and thin film systems need to be considered to accurately analyse the results.

Complex copper surfaces, consisting of a combination of metallic copper and multiple copper oxides were investigated over the course of this project. Before discussing the formation and properties of these surfaces, the naming conventions are briefly explained: Metallic copper is described chemically as Cu or Cu^0, as it holds no charge. When oxidized once, cuprous oxide, expressed as Cu_2O is formed. In this compound, one oxygen atom is bound to two copper atoms. The copper transferres one electron to the oxygen to form the bond, therefore it is positively charged and the cuprous oxide can also be expressed as Cu^+ or Cu(I) oxide. When the oxidative state is increased again, more oxygen is incorporated. One oxygen atom is then bound to one copper atom by a double bond. This is called cupric oxide and is expressed as CuO. Because of the double bond, the copper atom relinquishes two electrons and is doubly charged, it can be expressed as Cu(II) oxide or Cu^{2+}. When two hydroxide molecules bind to copper across their oxygen atoms, copper hydroxide or $Cu(OH)_2$ forms. Here, the copper atom enters two bonds, one with each OH molecule. This is why both CuO and $Cu(OH)_2$ can be expressed as Cu^{2+}, as the copper atom holds the same positive charge in the chemical bonds.

Before the influence of (plasma activated) liquid on copper is considered, the oxidation of copper in ambient air is discussed, since this is the initial state of the copper examined in this work. The oxidation of copper in air is a time and temperature-dependent, multi-step process. The initial oxidation of a copper surface in a dry oxygen atmosphere is well understood. According to Zhou et al. [62], first oxygen molecules impinge on the surface and dissociate. They diffuse over the surface and chemisorb. At lower temperatures, the copper surface quickly oxidizes following the reaction:

$$2\,\mathrm{Cu} + \frac{1}{2}\,\mathrm{O_2} \longrightarrow \mathrm{Cu_2O}\cdot \tag{22}$$

Initially Cu_2O nuclei form across the surface. These impinge on each other and eventually merge to Cu_2O islands. More oxygen is captured by these islands which causes lateral growth. The growth of the islands has been found to be temperature dependent [62]. At high temperatures, the mobility of the oxygen increases which results in the oxygen capturing being more likely than the nucleation process. Therefore, at high temperatures, fewer larger islands form, at lower temperatures many small islands can be found. The copper oxidation layer reaches a few nm into the bulk [63]. Additionally, it was found, that the orientation and roughness of the underlying metal has an influence on the orientation of the oxide growth [63]. At elevated temperatures oxidation to a higher oxidative state is possible following [64]:

$$Cu_2O + \frac{1}{2}O_2 \longrightarrow 2\,CuO\,\cdot \tag{23}$$

On longer timescales and in the presence of water, both in the ambient air and when placed inside a liquid, oxidation and corrosion of the copper sets in. In both processes, the electrons from the copper relocate to the copper-liquid interface and then transfer into the liquid, leaving behind Cu^{2+} copper ions in the bulk [65] following:

$$Cu \longrightarrow Cu^{2+} + 2\,e^- \tag{24}$$

Then oxidation ours via:

$$Cu + Cu^{2+} + H_2O \longrightarrow Cu_2O + 2\,H^+\,\cdot \tag{25}$$

Simultaneously during the corrosion process, the (bulk or vaporized) water is ionized following:

$$O_2 + 2\,H_2O + 4\,e^- \longrightarrow 4\,OH-, \tag{26}$$

the electrons originating from the bulk metal [66]. This leaves solvated hydroxide ions in the vicinity of the interface. In the last step, the hydroxide oxidises the surface:

$$Cu_2{}^+ + 2\,OH^- \longrightarrow Cu(OH)_2\,\cdot \tag{27}$$

The resulting copper hydroxide is insoluble in water but more susceptible to removal through mechanical influences than the bulk copper. Submersion of a copper sample into a water-based solution therefore converts the surface into a combination of Cu_2O and $Cu(OH_2)$. This oxide layer is typically present in a continuous or amorphous form [66].

The temperature of the aqueous solution the copper is placed in has an impact on the oxidation mechanism and composition of the oxidized metal [66, 67]. At higher temperatures, the formation of higher oxidation states becomes favoured, just like under the influence of dry oxygen. The cuprous oxide is transformed into cupric oxide:

$$Cu_2O + 2\,OH \longrightarrow 2\,CuO + H_2O\,\cdot \tag{28}$$

In an electrochemical reactor, the desired reaction is rarely if ever performed in pure water. Instead the process is operated in an electrolyte. The pH of the aqueous solution the copper is placed in, has a significant impact on the composition of the oxidized metal. This is illustrated by a Pourbaix diagram as shown in figure 4:

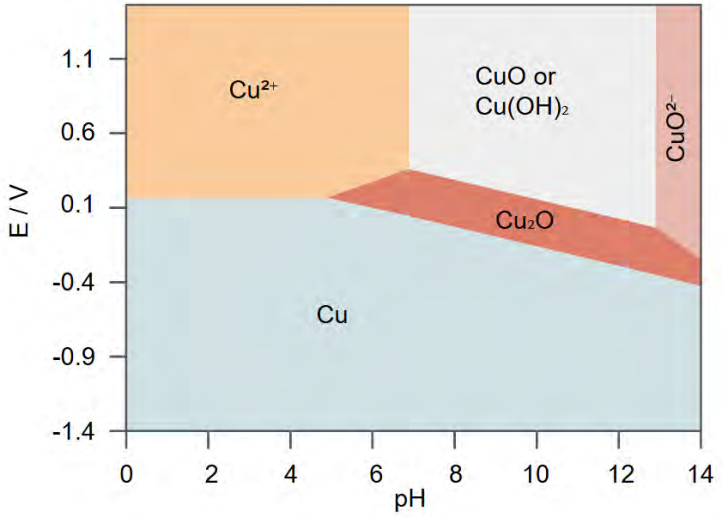

Figure 4: Pourbaix diagram showing the different stable oxidation states of copper in H_2O for different pH values at 25°C based on [68].

Here, the relationship between solution pH and applied voltage to a metal is illustrated. In an electrochemical reactor, a voltage would be applied to a catalyst. The process is described in more detail in section 2.5.2. When a copper sample is simply placed in water at a pH of 5, and no voltage is being applied, the sample would consist of pure copper. Only at higher pH, higher oxidative states like CuO and $Cu(OH)_2$ become stable compounds. In this work, experiments were performed in a potassium hydroxide (KOH) solution, which increases the pH of the solution and therefore has an influence on the copper. The creation of Cu_2O would be favoured.

In industrial applications, a common oxidant used to generate copper oxides in a targeted way is hydrogen peroxide [26]. This is can be done by the Chemical Mechanical Planarization (CMP) process. In this procedure, a bulk copper work piece is oxidised by H_2O_2 and the oxide is removed by abrasion [26]. At low pH the copper becomes susceptible to corrosion, at high pH the process becomes non-selective, as depicted in the Pourbaix diagram. Therefore, a pH-neutral solution is needed to perform the oxidation step. Hydrogen peroxide is a suitable oxidant for this reason. The CMP process is based on the assumption, that the oxidation of copper begins with nucleation of oxides in certain seed regions. These oxide seeds grow into oxide islands. This is analogous to the oxidation process in a dry oxygen atmosphere, with the distinction that the chemisorbed precursor is a electronegative oxidising species such as OH, OH^- or H_2O_2 instead of oxygen. DeNardis et al. have developed a model for the subsequent oxidation mechanism via cation migration [26]:
The chemisorbed H_2O_2 attracts electrons from the copper bulk that travel to the Cu/H_2O_2 interface and a potential difference develops. The negatively charged H_2O_2 ions are now considered the anions and the copper ions in the bulk are considered the cations, hence the name of the mechanism. The copper cations can now move along the potential to the interface and react with the H_2O_2 to copper oxide. This is illustrated in figure 5.

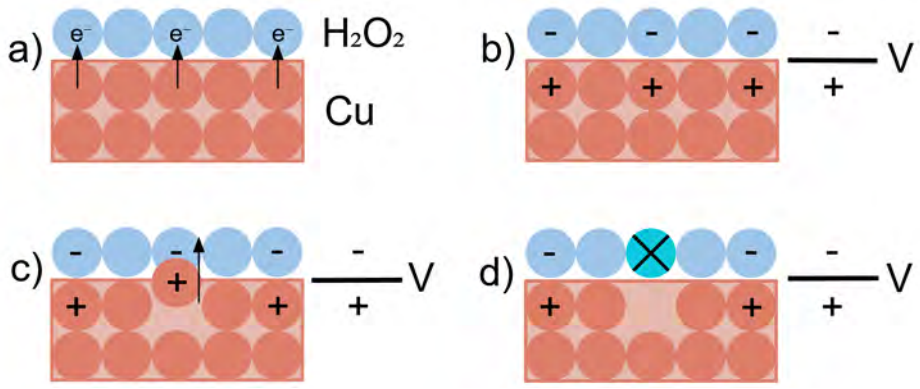

Figure 5: Illustration of the oxidation model by DeNardis et al. First, electrons propagate to the interface a), then a potential difference is established b), then a copper anion propagates towards the interface c) and lastly a copper oxide is formed d). Based on [26].

The group has found, that the oxide islands formed by the H_2O_2 solution consist only of Cu_2O after a few minutes of treatment time, while no CuO could be found and that the oxide film growth is faster at higher H_2O_2 concentrations [68]. The group does not explain the subsequent chemical reactions that would lead to the formation of the different copper oxides, however the dominant reaction in this system is known to be:

$$Cu^+ + H_2O_2 \longrightarrow Cu^{2+} + OH^- + OH^- \longrightarrow Cu(OH)_2. \tag{29}$$

Therefore, a reduction of the surface must take place to create the Cu^+ oxide islands. It is likely, that the process then follows the mechanism induced by water analogous to reaction 25 and 27.

In summary, the interaction between plasma-activated liquid and a copper surface is a complex system, consisting of oxidation, reduction and corrosion mechanisms involving many chemical species on different timescales. The process is influenced by factors such as solution concentrations, temperature, pH value and treatment times. Consequently, the analysis of the plasma-liquid-solid system requires multiple diagnostic methods. The physical background of the main techniques used in this work is described in the next section.

2.5 Primary Diagnostics and Methods

In the following section, the physical background of the used diagnostic methods is described in more detail. To monitor the changes of the copper under direct plasma influence, Fourier Transformed Infrared Spectroscopy and X-Ray Photoelectron Spectroscopy were employed. To investigate the effect of the plasma activated liquid on the copper, Cyclic Voltammetry and Scanning Electron Microscopy were used.

2.5.1 Fourier Transformed Infrared Spectroscopy

Fourier Transformed Infrared Spectrometry (FTIR) is a non-destructive diagnostic method to determine the chemical composition and chemical bonds of solid, liquid and gaseous samples [69]. One advantage of this technique is that it can be performed in-situ and in this work the technique is used to monitor the changes of the copper immediately after the plasma is ignited.
In FTIR spectrometry the vibrations of molecular bonds are exploited. The molecular vibrations are categorized into six types: the symmetric stretch, the asymmetric stretch, bending mode, rocking mode, wagging mode and twisting mode, as depicted in figure 6. The only vibrational mode usually not detectable by infrared is the symmetric mode [70]. Therefore this method allows the detection of almost all chemical groups and is widely used in many disciplines.

Stretching modes of the molecular bonds occur along the direction of the bond, causing the bond lengths to change. The bending and rocking mode modes are vibrations of atoms along the bond angles within one plane [70], the fist moving in opposite directions and the second in the same direction. The wagging and twisting modes are movements of atoms within multiple planes, the fist again being in one direction and the second in multiple different directions. The vibrational frequency is dependent on the mass of the atoms and bond strength, resulting in distinct vibrational energy differences between single, double and triple bonds [70].

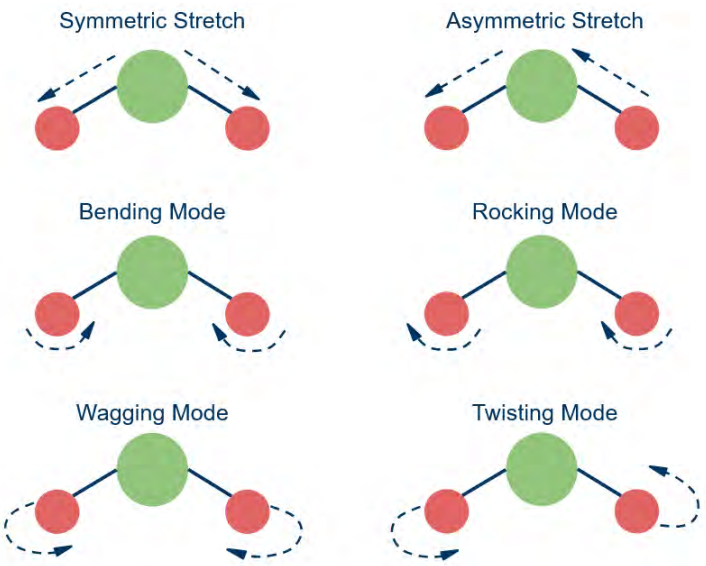

Figure 6: Schematic image of the different possible vibration modes. The atoms are able to move along the direction of the atomic bond, along the bond angles or within multiple planes.

These vibrational states can be induced by infrared (IR) radiation. Samples are illuminated with wavelengths matching the vibration frequencies of the molecule of interest. The molecules vibrations are stimulated and the radiation is absorbed. By dispersing the remaining light after the interaction with the molecules into its spectrum, information about the atomic vibrations and composition of the sample can be collected. This is done through Fourier-transformation. The method is performed using an interferometer, its working principle is illustrated in figure 7.

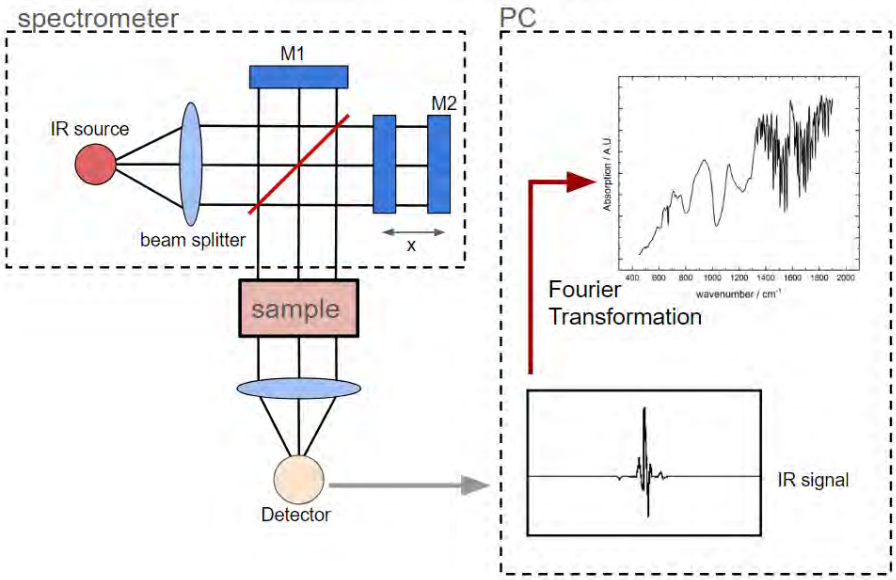

Figure 7: Schematic image of the FTIR setup based on [71]. It includes the interferometer, the external sample and a PC for processing of the spectra.

The infrared beam generated by the IR source, a black body radiator, is focused by a lens on a semi-transparent beam splitter, which reflects the two partial beams on a fixed mirror M1 and a moving mirror M2. The two beams reflect at the mirrors and then merge and interfere. By moving M2, the optical path length of the partial beam is changed, a phase difference between the two partial beams is induced and thus results a change in the interference amplitude. The re-combined IR-beam then is oriented onto the sample, where molecular vibrations are induced. The transmitted light is then focussed onto the detector by another lens. The intensity curve at the detector as a function of the optical path difference, corrected by a constant component, is called an interferogram. The IR spectrum is then Fourier-transformed and converted into a spectrum.

Typically, the resulting spectrum is displayed as the absorption or transition versus wavenumber. The spectrum is divided into four regions: the single bond region (2500-4000 cm^{-1}), the triple bond region (2000-2500 cm^{-1}), the double bond region (1500-2000 cm^{-1}) and the fingerprint region (500-1500 cm^{-1}) [69]. The characteristic bonds of copper and its oxides absorb IR radiation in the range of 500 - 1200 cm^{-1} and therefore in this work only the fingerprint region is of interest.

2.5.2 Cyclic Voltammetry

Cyclic voltammetry is an electrochemical diagnostic method, used for the analysis of the redox potentials of conductive materials. It can be used to determine the oxidative state of copper. Another advantage of this technique, is that it is possible to investigate the morphology of the copper oxides. The oxidation and reduction of a metal is an electron transfer process that can be initiated by applying a material specific oxidation or reduction potential. By applying a positive voltage, the metal releases electrons and is elevated into a higher oxidative state. On the contrary, in case of a negative voltage, electrons are absorbed and the oxidative state is reduced. The reduction reaction can simply be expressed as:

$$a\,\mathrm{Ox} + n\,\mathrm{e}^- \rightleftharpoons b\,\mathrm{Red} \tag{30}$$

Here, the term aOx and bRed refer to the stoichiometric amounts of the reactant and product, respectively. Additionally n indicates the number of electrons involved in the oxidation or reduction.
During a redox reaction the applied potential is connected to the concentration of the reactant and the product by the Nernst equation:

$$E = E^0 + \frac{2.303RT}{nF} log\Big(\frac{[A]^b}{[B]^a}\Big) \tag{31}$$

In this equation, E is the electrode potential, E^0 is the formal potential, R is the gas constant, T is the temperature and F the Faraday constant. This relationship defines the equilibrium potential of an electrode in an electrolyte. These voltammetry experiments are performed an electrochemical cell, a scheme of which is shown in 8.

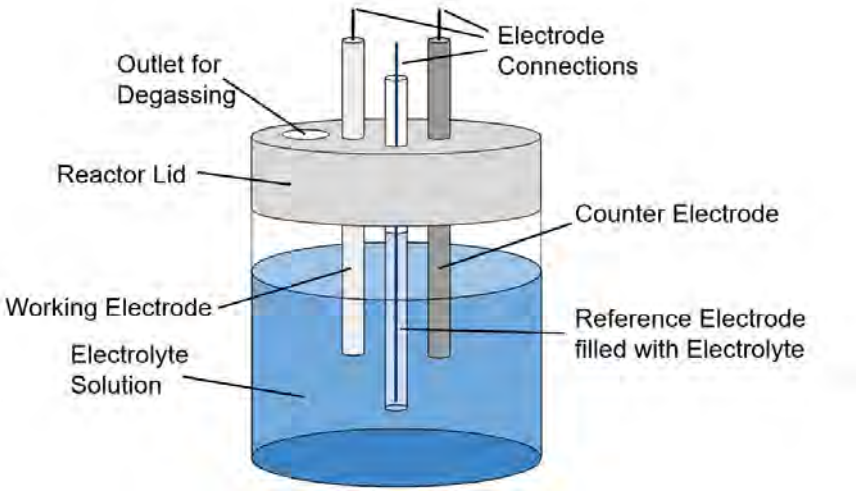

Figure 8: Schematic image of a standard three electrode electrochemical cell. It includes a working electrode, counter electrode and reference electrode, all of which are placed inside an electrolyte.

Conventionally, the CV experiment is set up in a three electrode system, consisting of a working electrode, counter electrode, and reference electrode [72]. Typically, for the measurement the electrodes are submerged in the same electrolyte. At the working electrode, a voltage is sweeped linearly over time in a cyclical fashion. This causes electron transfer both at the working and counter electrode which initiates a current between the two electrodes. At the counter electrode, the current density is then measured in response. The oxidation or reduction also create a layer of ions, called an electrochemical double layer (EDL), at the electrode. The EDL consists of a dense layer at the electrode interface and one diffuse layer in the electrolyte. The reference electrode possesses a known electrode potential and is used to control the voltage at the working electrode. The voltage-current-measurements are recorded in the form of a voltammogram, where the current density is plotted against the potential. The sweeped voltage generates a reduction or oxidation reaction both at the surface of the sample and of the electroactive species in the liquid, which is measured in the current. Through this, the composition of the samples can be determined.

Before interpretation, the voltammograms are corrected for the ohmic drop. This drop is generated by the electrolyte in which the measurement is performed. Over the distance between the working and reference electrode, the electric potential decreases due to the finite resistance of the liquid. The current-voltage curves need to be shifted accordingly. For this, Electrochemical Impedance Spectroscopy (EIS) can be employed. During this supplementary measurement, a sinusoidal AC current or voltage varied over a range of frequencies is applied to the working electrode and the response of the system is measured [73]. From the response, an equivalent electrical circuit can be constructed. In the electrochemical cell, multiple different processes such as charge-transfer, mass-transfer or adsorption and desorption at surfaces, take place on different time scales. Varying the frequency ensures the detection of those different processes and a more accurate simulation of such a circuit. The construction of the equivalent electrical circuit is a function of most electrochemical analyser software [73]. The impedance is included in the circuit as an equivalent resistance. The voltage response recorded during the CV measurement is then shifted using Ohm's law.

In this work, cyclic voltammetry is used to investigate changes in the plasma-treated copper samples. The sample represents the working electrode. Since the goal of this work is the oxidation of the samples by in-liquid plasma, only the reduction of the samples is investigated using this method. Under the influence of the electrolytic potential, a reduction of the copper oxide occurs following the reaction [64]:

$$\mathrm{Cu_2O + H_2O + 2\,e^- \longrightarrow 2\,Cu + 2\,OH^-} \tag{32}$$

$$\mathrm{CuO + H_2O + 2\,e^- \longrightarrow Cu + 2\,OH^-} \tag{33}$$

This leads to the method having a destructive effect on the used copper samples. Only one cycle can be applied before the effect of the plasma is reversed.
From the resulting voltammogram, the composition of the copper oxide sample can be deduced, since the reduction potential is specific to the oxidative state of the sample. The current density and therefore the height of the peaks in the CV provide insight into the amount of the oxides present. Additionally, the morphology of copper oxides can be extracted from this method [74], since the reduction potential is dependent on the crystalline structure of the oxide. In this work, cyclic voltammetry has been used to identify Cu, CuO_2, CuO and $Cu(OH)_2$ as constituents of the samples.

2.5.3 X-Ray Photoelectron Spectroscopy

X-ray photoelectron spectroscopy (XPS) is a spectroscopic method which can be used to gain insight into the chemical composition of the first few nanometres of a solid surface [75, 76]. In this work, the technique is used to separately investigate the effect of the direct plasma effects and the effects of the plasma activated liquid. In this method, the photoelectric effect is exploited by directing X-rays with a known energy onto a sample. The energy is transferred to a core level electron of an atom, which is then expelled from the sample with a specific kinetic energy E_k . The photoelectrons are detected in a multi-channel detector, which sorts them according to their kinetic energy, resulting in an energy spectrum. The process is depicted in figure 9 a).
The kinetic energy of the photoelectrons is connected to their binding energy E_b according to:

$$E_b = h\nu - E_k - \phi_{sp}. \tag{34}$$

Here, ϕ_{sp} is the work function of the XPS device, $h\nu$ the energy of the X-rays. Since the binding energy is specific to each element and their orbital, the XPS method provides information about the elements which the sample consist of.
The photoelectron peaks in the XPS spectrum are named according to the orbitals they originate from [75]. In this work XPS was used to investigate the plasma treated copper and the nanoparticles formed by electrode erosion. The primary energy regions of interest are the Cu2p region and the W4f7/2 region. The names indicate, that the photoelectrons stem from the 2p orbital of the copper atom and the 4f orbital of the tungsten atom, respectively.

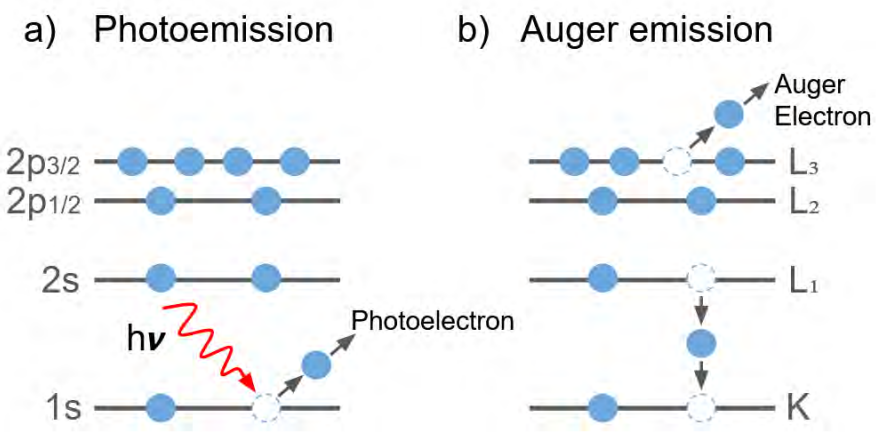

Figure 9: Schematic sketch of the emission processes of a photoelectron a) and an Auger electron b).

The binding energies of the electrons are influenced by the molecular structure in which the atom is bound and, in the case of a metal, the oxidative state of the material. As oxidation is the transfer of an electron of a metal to an oxygen atom, the metal atom becomes positively charged. More energy is then needed to remove an additional atom from an inner orbital which results in a shift of the photoelectron peak [75]. Therefore, the XPS spectrum holds information about the oxidative state of a metal.

The Cu2p energy region of copper lies around a binding energy of 970 - 930 eV [76, 77]. In the case of metallic copper, two peaks are visible in the Cu2p region, one at 933 eV and one at 953 eV. They originate from the two spin orbit components $Cu2p_{3/2}$ and $Cu2p_{1/2}$. They are very pronounced and can be easily distinguished. If the copper is partially oxidised, a so-called shake up structure, at around 942 eV and 962 eV can be found. Inconveniently, the binding energies of the different oxidation states are very similar. The signal originating from metallic copper and Cu_2 as well as the two signals from CuO and $Cu(OH)_2$ look alike as shown in figure 10. If a sample consists of multiple oxidative states, they can not be distinguished. The Cu2p region indicates, whether a copper surface is oxidised, but not which oxides are present and in which amounts. In order to to determine the exact composition of the sample, another method needs to be applied.

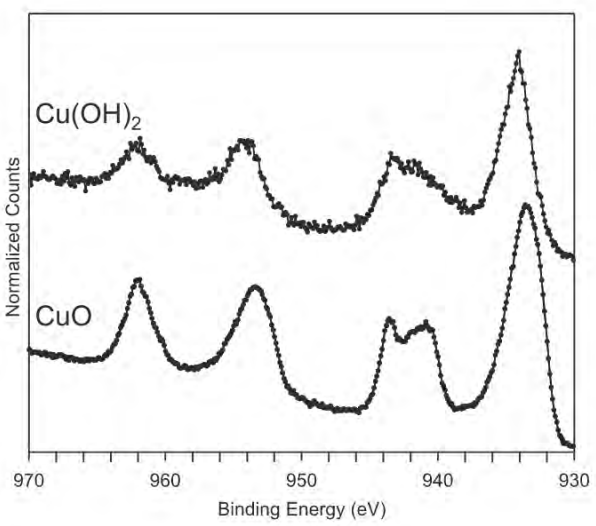

Figure 10: Cu2p spectra of $Cu(OH)_2$ and CuO adapted, from [77]. The XPS spectra of the two Cu(II) states are very similar.

To gain further insight into the composition of a sample, the Auger effect is exploited. When a photoelectron is removed from a core orbital, a hole is left behind. The hole is then filled with another electron from an outer orbital. The excess energy from this transition is equal to the difference in binding energies between the two involved orbitals. If the energy difference is greater than the binding energy of an outer shell, another electron is expelled from the atom. The Auger process is pictured in figure 9 b). The kinetic energy E_k of the expelled Auger electron can be described as:

$$E_k = E_C - E_A - E_B, \tag{35}$$

where E_C is the orbital energy of the core level, E_A the energy of the shell from which the transitioning electron originates and E_B the energy of the shell from which the expelled electron originates. In Auger spectroscopy, the Auger electrons kinetic energy is recorded and interpreted. The spectrum is named after the orbitals of the involved electrons. In this work, the CuLMM spectrum is investigated. Here, the first electron is expelled by the X-rays from the L orbital of a copper atom, the hole is filled by an electron from an M orbital and the Auger electron also originates from an M orbital.

The $CuL_3M_{4,5}M_{5,5}$ region lies between 906 eV and 925 eV, as seen in figure 11. In the Auger spectrum, the oxidative state and oxide composition can clearly be distinguished. The binding energies of the Auger electrons are also influenced by the oxidative state of the surface and the spectrum changes according to the oxygen content.

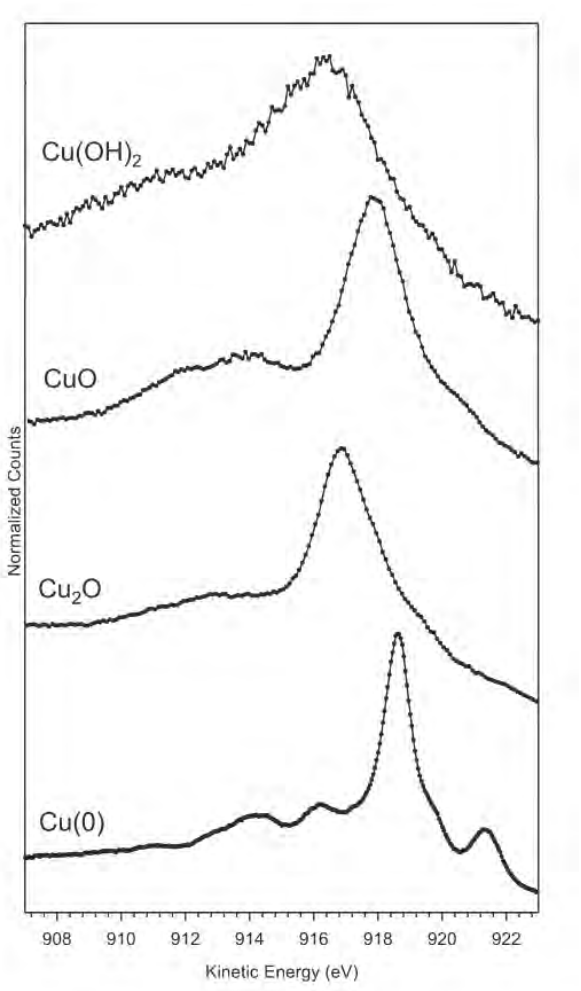

Figure 11: $CuL_3M_{4,5}M_{5,5}$ peak of metalic copper, Cu_2O, CuO and $Cu(OH)_2$, adapted from [77]. The Auger spectra can be used to identify the composition of a copper sample.

3 Experimental Setup and Diagnostics

3.1 Electrical Setup

In this work, a distinction is made between pulsed in-liquid plasmas operated with pulse lengths in the microsecond range and in the nanosecond range. Two experimental setups were used and compared. In addition to the electrical setups, there are some significant differences between the voltage and current measurements between the microsecond and nanosecond pulsed plasma setups. The two electrical setups and the differences between them are described in the following section.

3.1.1 Microsecond Plasma

In figure 12 a schematic of the electrical setup of the microsecond pulsed plasma experiment is shown. The plasma is operated using a generator by Heinzinger, model PNC 40000-5ump. The voltage can be varied between 0 and 30 kV. The plasma is ignited by discharging a capacitor. A function generator (HP 8116A Pulse/Function Genrator), delivers the trigger signal for the discharge frequency, which is varied between 1-100 Hz. The pulses have a full width half maximum (FWHM) of 200 µs and a rise time of 0.5 µs.

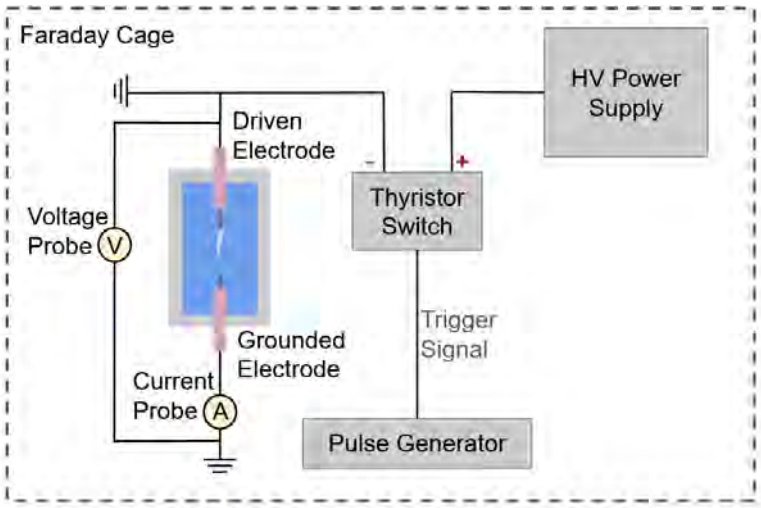

Figure 12: Schematic of the electrical setup of the µs pulsed plasma experiment. The plasma is ignited by discharging a capacitor, triggered by a pulse generator and charged by a high voltage power supply. The setup is placed inside a faraday cage.

For the microsecond setup, the voltage and current is measured directly using a voltage probe and a Rogovski coil around the grounded electrode of the setup, respectively. The voltage and current curves are recorded with an oscilloscope (Teledyne LeCroy GmbH model HD6104A). The absorbed power is calculated with $P = U \cdot I$ and the dissipated energies can be determined by integrating the power over time.

3.1.2 Nanosecond Plasma

Figure 13 shows a schematic of the electrical setup of the nanosecond pulsed plasma experiment. The generator used in this setup is by FID Technology GmbH and produces high voltage pulses in the nanosecond range. The pulses have a FWHM of approximately 12 ns and a rising time of 2-3 ns. The voltage can be varied between $\pm$0-30 kV and the frequency between 1-100 Hz. The plasma ignites reliably in distilled water at voltages upwards of 16 kV.

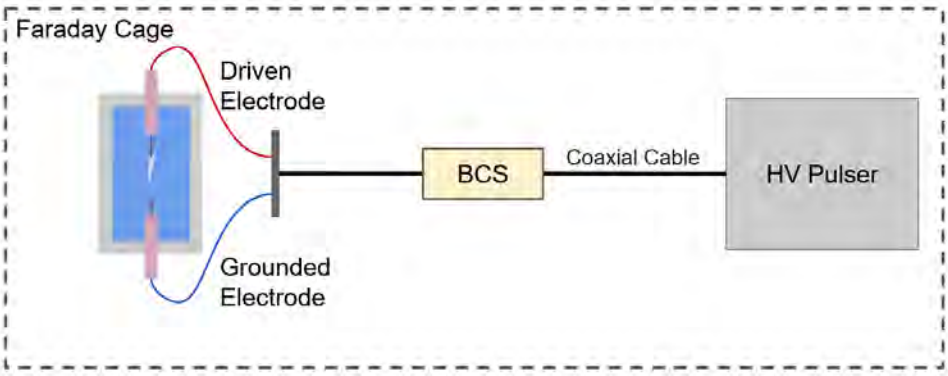

Figure 13: Schematic of the electrical setup of the ns pulsed plasma experiment. The plasma is ignited by a high voltage power supply delivering voltage pulses in the ns range. A back current shunt is integrated in the coaxial cable. The setup is placed inside a Faraday cage.

The voltage of the nanosecond setup is indirectly measured using a back current shunt (BCS) integrated in the coaxial cable of the electrode. The current can not be measured directly but can be derived from the voltage measurement using the equation:

$$I = \frac{R_{out} + R_{scope}}{R_{scope}} \cdot \frac{\gamma}{R_{shunt}} \cdot U, \tag{36}$$

where $R_{out} = 50\ \Omega$ is the resistance of the shunt connector, $R_{scope} = 50\ \Omega$ the resistance of the oscilloscope, $\gamma = 31.623$ the attenuation factor of three attenuators coupled in series at the oscilloscope and $R_{shunt} = 0.3\ \Omega$ the resistance of the BCS cable. The measurement method and calculation is based on the work of Seepersad et al. [78]. In both experimental setups a Faraday cage is included to shield the surrounding devices from the electrical noise of the plasma.

3.2 Reactor Setup

The in-liquid plasma reactors used in the microsecond and the nanosecond setup are identical. The plasma reactors are connected to their respective power supplies with a RG217 coaxial cable. The reactor chamber shown in figure 14 is made out of polymethyl methacrylate (PMMA) and can contain a liquid volume of approximately 25 ml. It has inlets on all edges to fill the reactor. Two optical windows are installed on each side for optical access. The electrodes are set up in a pin-to-pin configuration, with the grounded electrode consisting of a stainless steel cannula and the driven electrode of a wire with a diameter of 50 μm consisting of tungsten wire from Goodfellow. The distance between the electrode tips is typically about 1.5 cm as depicted in figure 14 a). One of the side walls of the chamber consists of a substrate holder where the samples can be placed. The samples are mounted in the reactor with the copper surface facing towards the plasma. The distance between the electrode tip and the samples is approximately 1 cm. This distance varies due to the inevitable curling of the electrode wire during plasma treatment. A second side wall without a sample holder can also be used for liquid treatment only.

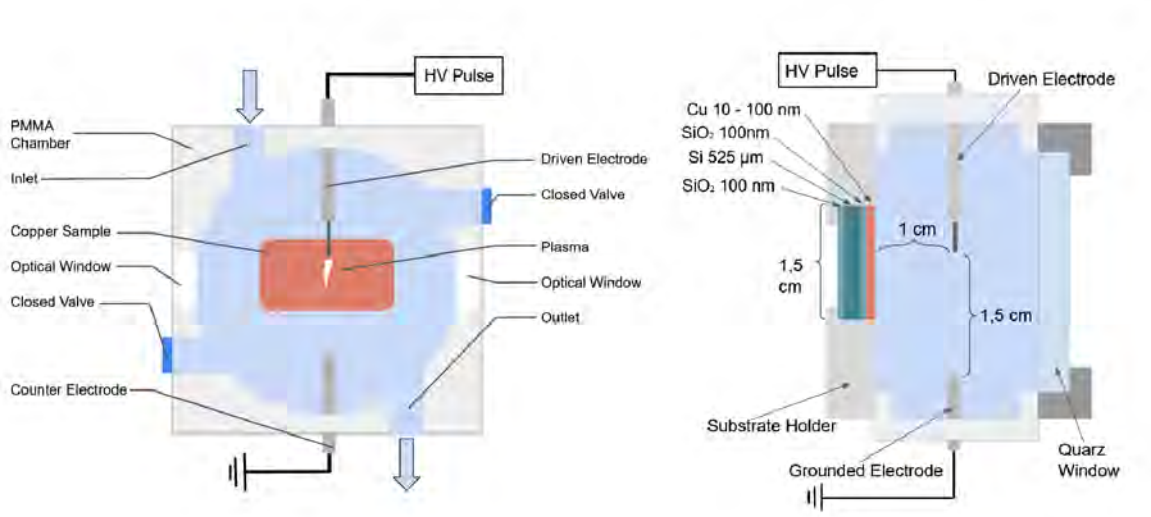

Figure 14: Schematic of the plasma reactor, a) side view and b) front view. The copper sample is installed in the front wall of the reactor. It is placed approximately 1 cm from the tip of the electrode, the site of plasma ignition.

3.3 Production and Analysis of Liquids

The majority of measurements were performed in distilled water with an electrical conductivity of 2µS/cm and a pH of 5.5. In addition, KOH solutions were used as a reference electrolyte. The in-situ surface changes were monitored in distilled water and in KOH solution of 0.01, 0.05, 0.1 mmol/l. The temperature, electrical conductivity and pH are measured directly after PAW generation. The temperature and conductivity were measured using a thermocouple and conductivity meter by Greisinger (model GLF100). Hydrogen peroxide concentrations were measured using photometric spectroscopy with a Merck 118789 assay kit by Spectroquant, which can detect hydrogen peroxide in concentrations of 0.015 to 6.00 mg/l. The test kit works as follows: the assay contains a compound which reacts with H_2O_2, namely neocuproine. After the liquid is treated by the plasma, it is diluted with distilled water in ratio 1/9 and then combined with the assay.

The samples are left for a few minutes to ensure the reduction reaction has taken place and are then placed into a commercial photometer. The photometer has been adjusted to detect hydrogen peroxide by producing light with the absorption wavelength of the reduced neocuproine. The photometer then measures the transmitted signal from which the concentrations are calculated. For this, a calibration curve determined from solutions with known H_2O_2 concentrations has been used. Additionally, test strips by ITS Europe sensitive in the range of 0.5 - 500 mg/l have been used as an alternative and swift way to monitor the H_2O_2 concentrations.

3.4 Shadowgraphy Imaging

To determine the erosion of the electrodes tips of the nanosecond-pulsed plasma producing nanoparticles, shadowgraphy imaging was performed. All nanoparticle measurements were performed in distilled water. A sketch of the setup is shown in figure 15. A xenon arc-lamp is positioned facing towards one of the optical windows of the reactor. The electrode tip creates a shadow in the path of the light passing through the chamber. The image of the electrode tip is focused onto an intensified charge-coupled device (ICCD) camera (Andor iStar ICCD camera model DH734-18U-03) using a lens with a focal length of $d = 12$ cm. The camera is connected to a computer where the images are recorded.
The repeated ignition of the plasma causes erosion of the electrode due to explosive heating of the material. During the process, the electrode wire moves and curls. For this reason, accumulated shots are taken. The change in length and shape of the tungsten wire are monitored via shadowgraphy images. For this, the loss in length is compared to the known thickness of the 50 μm wire visible in the images.

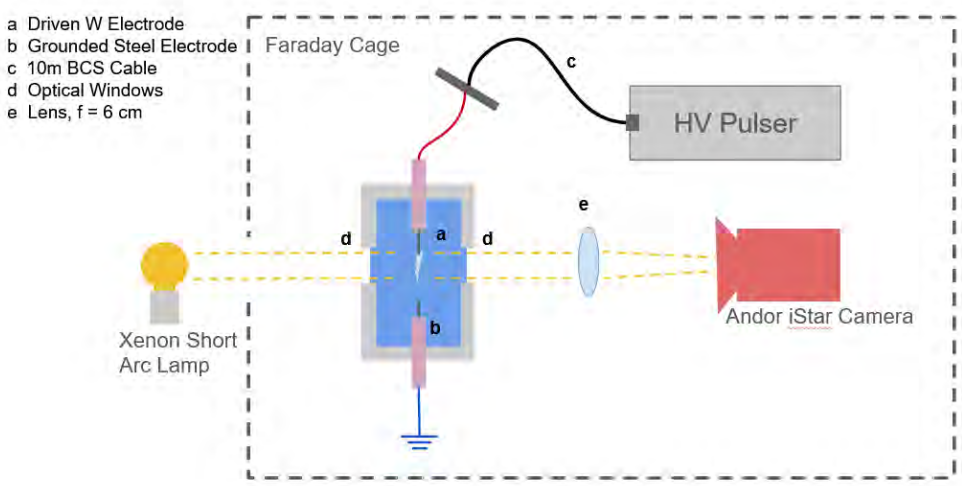

Figure 15: Illustration of the shadowgraphy imaging setup. The driven electrode is connected to the high voltage pulser. The electrode is being backlit by a xenon short arc lamp and the shadow of the electrode tip is focussed on an Andor iStar camera. The beam path passes through the optical windows of the plasma reactor on opposite sides of the chamber.

3.5 Transmission Electron Spectroscopy (TEM)

In this work, Transmission Electron Spectroscopy (TEM) was used to examine the nanoparticles that are generated from the electrode of the nanosecond-pulsed plasma. The device is located at the Center for Solvation Science (ZEMOS) at Ruhr-University Bochum. The TEM device is of the model JEM-2800 operating with a Schottky field emission cathode by the company Jeol. It can be operated at acceleration voltages between 100 kV and 200 kV. The maximum voltage was used to generate the images presented in this work. The technique generates a chromatic aberration of 1.3 mm and a spherical aberration of 0.7 mm.

The images were recorded by Paolo Cignoni, who prepared the samples and operated the device: First the liquid volume of the sample was reduced by rotary evaporation in vacuum from approximately 25 ml to 1 ml. The sample volume was then increased again by adding 1 ml of ultra pure water. From this solution 100 µl were taken and drop-cast onto an ultra-thin lacey carbon support film with a 400 mesh copper grid on top of a ultra-thin carbon film. In the TEM images, the metallic nanoparticles contrast well with the organic carbon support structure.

3.6 Copper Sample Preparation

The samples consist of silicon wafers by Si-Mat Silicon Materials with a thickness of 525 µm. The majority of the used samples were Optical Cavity Substrates (OCS), comprised of the silicon layer at the centre and 1000 nm oxide layers on both sides of the substrate. The OCS substrates were used to enhance the sensitivity of the FTIR method at 2000 cm^{-1} at an angle of incidence of 70°. Additionally, the low conductivity of the substrate enables the examination of the effect of electrolysis on the copper surface only. Some measurements were performed using a unoxidised Si wafer also with a thickness of 525 µm.

The samples were coated with copper using a High Power Impulse Magnetron Sputtering (HiPIMS) system. The silicon and OCS wafers were first cut to a suitable size of 2 cm times 3 cm and then placed under the copper target of the HiPIMS chamber. An argon plasma is ignited at the target at a pressure of 0.5 Pa. The deposition rate was periodically verified using a profilometer and was typically laid in the range of 0.9 - 1.3 nm/s.

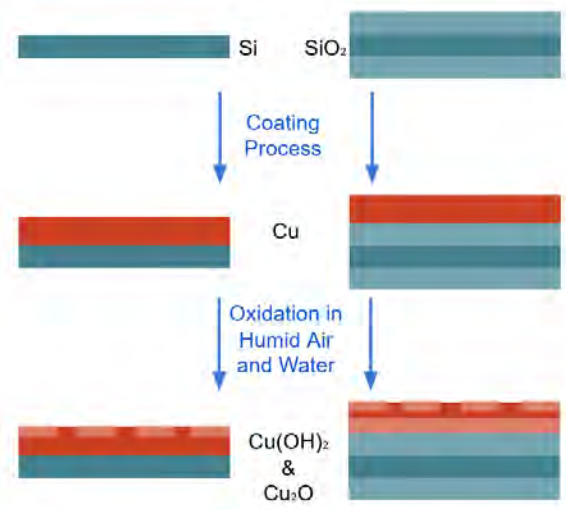

Figure 16: Schematic of the samples before treatment. The Si or SiO_2 wafers are coated with a copper layer varying between 10 an 100 nm in thickness. When removed from the coating reactor they come into contact with ambient air and oxidize.

Typical settings for the HiPIMS operation were 740 V, 109 A, 1 kW, 35 Hz and a pulse time of 50 µs. The thickness was customized depending on the diagnostic, varying between 10 and 100 nm. For the FTIR measurements, thin films with 10-15 nm were used, thicker films of 50-100 nm were needed for SEM, CV and XPS measurements to increase conductivity of the surface.
Once removed from the HiPIMS chamber, the copper surface comes into contact with humid air, therefore a thin oxide layer is formed on all samples analysed in the following results. This is illustrated in figure 16. Additionally, an oxide layer will inevitably form once the sample is mounted in the reactor chamber and the samples comes into contact with the electrolyte.

3.7 Fourier Transformed Infrared Spectroscopy

As shown in figure 17 the copper samples can be accessed by the IR beam from the backside. For in situ analysis, a FTIR spectrometer by Bruker (IFS 55 Equinox) is used. The device is operated in reflection mode. Since the electrical noise from the plasma generation disturbs electrical devices in close proximity to the experiment despite the Faraday cage, the FTIR can not be operated while the plasma is running. Therefore, the FTIR spectra are recorded in-between surface plasma treatments and in operando measurements could not be performed.

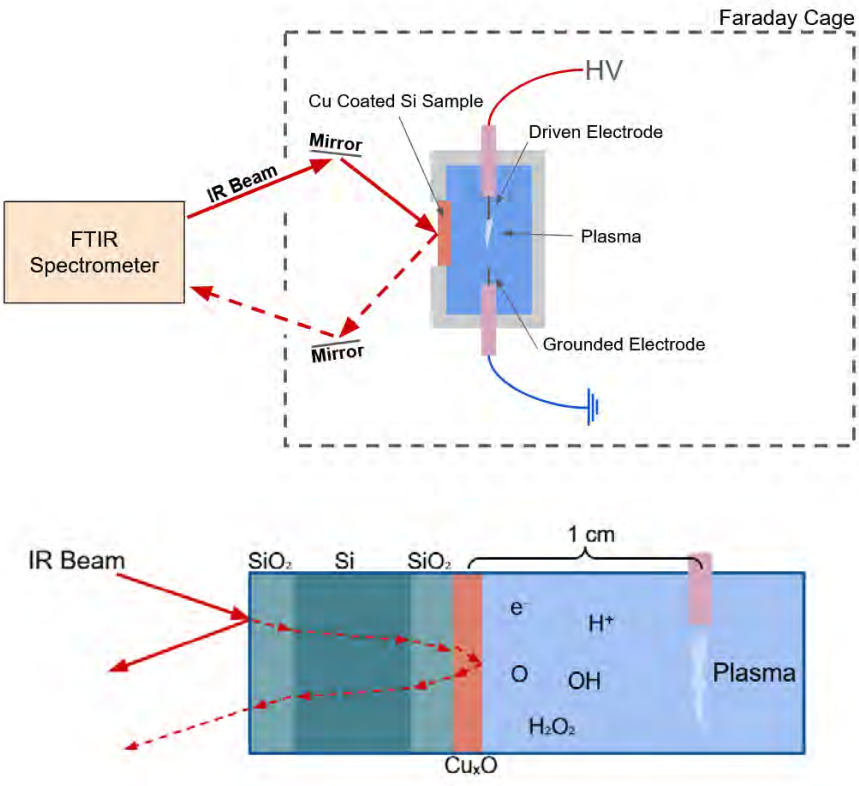

Figure 17: Schematic of the FTIR treatment. The IR beam is orientated to the backside of the wafer, the copper coated side is facing the plasma. The plasma reactor and its power supply is positioned inside a Faraday cage, the FTIR spectrometer is outside to protect it from the electrical noise emitted by the plasma setup.

In the FTIR spectra, the expression of different absorption lines for the constituents of the samples are monitored. Below 500 cm^{-1}, additional lines of the copper oxide species have been recorded but due to the poor sensitivity of the detector in this range, they have not been interpreted. The absorption lines are listed in table 1.

Table 1: Selection of absorption lines present in the fingerprint region of copper oxide.

species	wavenumber cm^{-1}	Source
CO_2	668	HITRAN
CuO	478-480	[79, 80]
CuO	527-536	[79, 80, 81]
Cu_2O	610-619	[79, 80, 81]
Cu_2O	617	[80, 81, 82, 83]
$Cu(OH)_2$	628	[84]
SiO_2	1000-1300	[85, 86]

From the values in table 1 it becomes clear, that the absorption line of copper hydroxide overlaps with one of the primary lines of cupric oxide and therefore can not be easily distinguished. In addition to the copper oxide lines, signals from other sources can be seen in the FTIR spectra that need to be discussed. In all FTIR spectra the absorption line of CO_2 is visible due to the ambient air in the beampath. Furthermore, the signal originating from the underlying SiO_2 layer can also be clearly seen in the spectra.

3.8 Cyclic Voltammetry Setup

To further investigate the state of the surfaces ex-situ, cyclic voltammetry is used. The measurements are performed using a potentiostat by BioLogic (model VSP 300). It is operated using the accompanying software EC-Lab by BioLogic. A scheme of the setup is shown in figure 18. Here, the pre-treated copper sample is placed at the bottom of the reactor and connected to the potentiostat. A Hg/HgO electrode is used as the reference electrode containing a 0.01 M KOH solution, as it is suitable for alkaline environments [87, 88].

The sample now functions as the working electrode. The reactor is then filled with an electrolyte. For this purpose a solution of 0.01 M KOH and 0.1 M K_2SO_4 is used. The electrolyte is then degassed for approximately 20 minutes using a low flow of argon. Otherwise, the remaining oxygen in the electrolyte would result in a background signal during the measurement. Next, the argon inlet is removed and the counter- and reference electrode are placed in the reactor. A negative voltage is applied and ramped over time. The sample is reduced and the responding current density is measured via

the counter electrode.

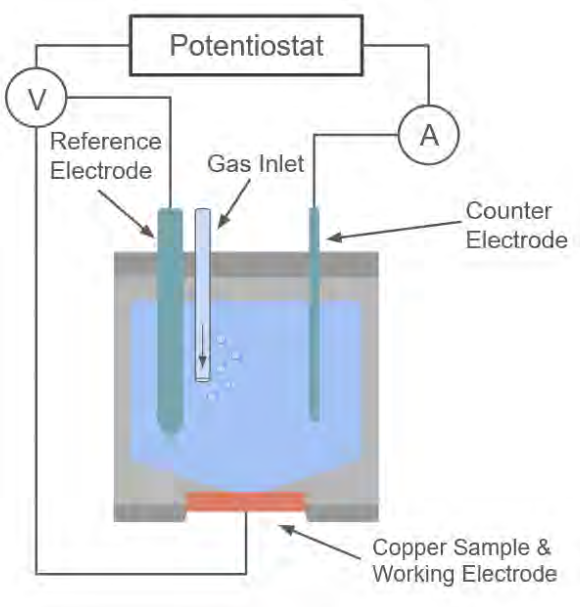

Figure 18: Schematic of the cyclic voltammetry setup. [89]. The sample functions as the working electrode. The measurement is performed in a solution of 0.1 M K_2SO_4 and 0.01 M KOH.

With this setup, the open-circuit voltage (OCV), a cyclic voltammogram (CV) with a scan rate of 20 mV/s and an electrical impedance measurement (EIS) were recorded. From the CV curve, information about the chemical characteristics like the oxidation state can be deduced as described in 2.5.2. The raw CV data is then processed for evaluation using the EIS measurement. The inherent resistance of the setup and electrolyte results in a shift of the reduction potentials in the CV curve, called the Ohmic drop. To correct this, the potential shift is calculated using EIS and then subtracted from the CV data.

3.9 X-Ray Photoelectron Spectroscopy

The surface modifications of the copper samples and the tungsten nanoparticles generated from the electrode material were analysed ex-situ with X-ray photoelectron spectroscopy (XPS). This method can be used to determine the surface composition of the samples. In the XPS device multiple locations on one sample can be investigated. The copper samples were prepared by dropcasting the PAW onto a copper sample, the tungsten nanoparticles were fixed onto carbon support film in the same fashion as described in the previous section on the TEM method 3.5.
For the analysis of these measurements the advanced analysis method of Biesinger et al. [77] is used. They provide quantification methods for pure copper, cupric oxide, cuprous oxide and copper hydroxide, which are applied to the CuLMM Auger peaks of the spectra. Additionally, the Cu2p peaks of both the copper and tungsten samples were analysed. From these measurements, the presence of oxides can be derived. A downside of the Cu2p peak analysis is, that Cu_2O and CuO can not be distinguished, since the binding energies of these species overlap. For this reason the $CuL_3M_{4,5}M_{5,5}$ peak, recorded using Auger electron spectroscopy, needs to be considered.
Before the quantifications can be applied, the spectra need to be charge corrected. This is done via reference spectra. A linear background is applied to the C 1s area of the measured spectra and the reference data is then compared to the sum of the properly weighted reference, taken from literature [77]. The spectra are shifted in such a way, that the binding energies of the C 1s peak lies at 284.8 eV.

3.10 Scanning Electron Microscopy

In this device, an electron beam produced with and electron gun is focussed on and scanned over the sample by electromagnetic lenses. At the sample, both elastic and inelastic scattering of the electrons with the sample occurs. Electrons with similar energies as the initial beam energy are produced by elastic scattering at the sample. These electrons are scattered at an angle larger than 90° and are called backscattered electrons or (BSE). The scattering angle of the electrons is dependent on the atomic number of the material and carries information of the atomic composition.
Electrons with lower energies result from inelastic scattering, where the electrons of the sample are exited and emitted as secondary electrons or SE. Secondary electrons are released from the topmost atomic layers and are therefore suited for imaging of a surface.

In this work, the images shown have been constructed from measuring the secondary electrons using a lower electron detector (LED) [90]. This detector is positioned at an angle in relation to the sample and consist of a scintillator followed by a photomultiplier, therefore producing a current proportional to the number of electrons emitted from the sample. By scanning the electron beam over the sample, images can be created. The measurements are performed inside vacuum to avoid interaction with the ambient air. The technique is limited to conductive samples, since on a non-conductive surface the electrons have no means to escape and a charging effect occurs.
Both the appearance of the electrode tip and the composition of the copper samples were examined ex-situ using Scanning Electron Microscopy (SEM). The SEM device used in this work is located at the Center for Interface-Dominated High Performance Materials (ZGH) at Ruhr University Bochum. It is of the model JSM-7200F by Jeol and provides a resolution between 1.6 nm at 1 kV acceleration voltage and 1 nm at 30 kV [90]. The low electron detector (LED) was used to detect the secondary electrons. Typically, an acceleration voltage of 10 kV and a probe current of 2 nA were used.

4 Results and Discussion

The following chapter first discusses the characterization of the microsecond- and nanosecond-pulsed plasma. The distinctive discharge properties are investigated. Then, the plasma activated liquid will be characterized, taking temperature, conductivity, pH and hydrogen peroxide production into account. Additionally, the electrode erosion and production of nanoparticles from the electrode material is presented. Then, the influence of the PAL on the copper is discussed. Here, a distinction is made between direct and indirect treatment, based on the short- and long-lived reactive species produced by the plasma. Lastly, reaction schemes based on these findings are presented.

4.1 Discharge Characteristics of Microsecond and Nanosecond-Pulsed Plasmas

In this thesis, the influence of in-liquid plasmas is investigated considering two different ignition mechanisms: by pulses in the microsecond and the nanosecond range. In case of the microsecond-pulsed plasma, the ignition takes place in bubbles originating from the evaporation of liquid in the vicinity of the electrode. In the nanosecond-pulsed case, the ignition occurs directly inside the liquid. These different ignition mechanisms lead to different PAL properties and may therefore have different effects on the copper oxidation.

To evaluate the plasma chemistry and the effect of the PAL on copper, the two plasma types need to be characterized. In figure 19a) and figure 19b), the two voltage and power curves from igniting a plasma in distilled water at a voltage of 20 kV can be seen.

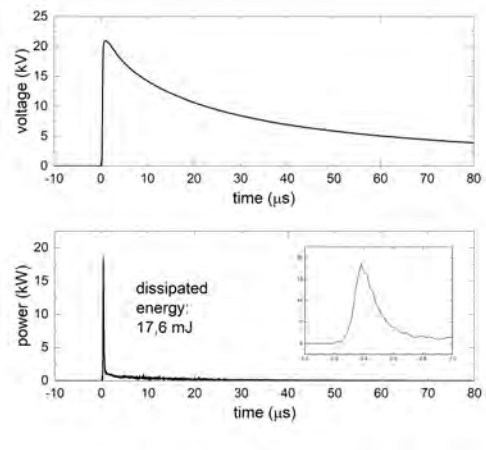

(a) Microsecond voltage pulse and dissipated power, ignition at 20 kV in distilled water with a 50 μm electrode. Adapted from [89, 91].

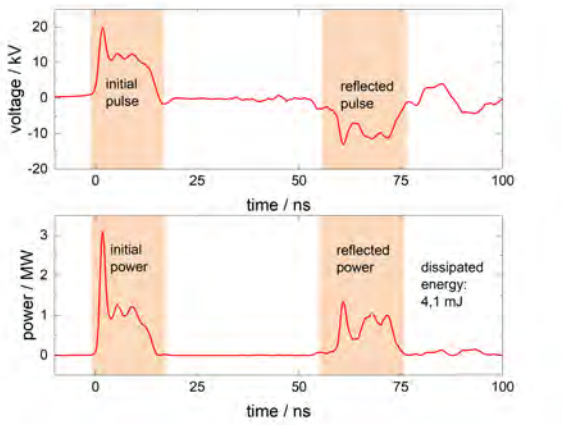

(b) Nanosecond voltage pulse and dissipated power, ignition at 20 kV in distilled water with a 50 μm electrode. Adapted from [89].

The µs pulse possesses a length of 200 µs with a rise time of 0.5 µs. The ns pulse has a pulse length of 12 ns with a rise time 2-3 ns. Since the former is measured directly and the latter is measured indirectly via a back current shunt (BCS) as described in 3.1, there is a noticeable difference between the shapes of the two voltage curves. The microsecond pulse shows a steady decay over time. The nanosecond pulse has two distinct peaks, the initial and the reflected pulse. The reflection originates from the impedance mismatch of the setup. The HV pulse is partially reflected and travels back and forth between the electrode tip and the power generator and is detected multiple times at the BCS.
From the voltage measurements, the power and dissipated energies can be deduced as described in section 3.1. In the case of the nanosecond setup this results in an initial and a reflected power, the dissipated power is calculated by subtracting $P_{reflected}$ from $P_{initial}$. To determine the dissipated energies, the power is integrated over time. The two plasmas yield different dissipated energies at the same applied voltage. In the ns case it has been calculated to be 4.1 mJ, one order of magnitude smaller than the 17.6 mJ for the µs plasma. Both plasmas can be operated within a voltage range of about 16 to 30 kV at either positive or negative polarity.

It has been found, that the dissipated energies for both setups increase with voltage, as shown in figure 20:

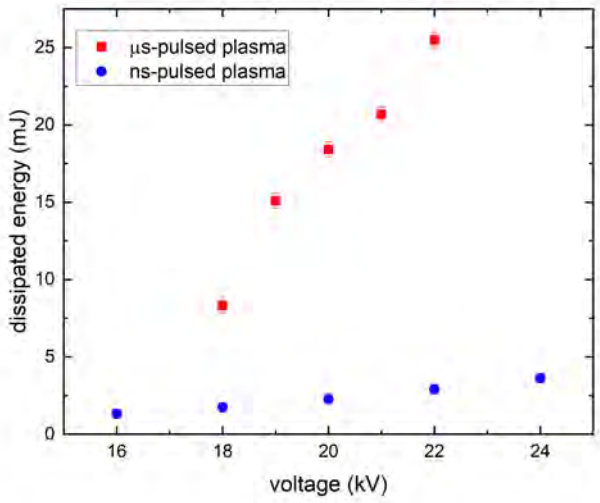

Figure 20: Dissipated energies of the microsecond pulsed plasma (red) and the nanosecond pulsed plasma (blue) at varying voltages.

Here it becomes clear, that the energy dissipated by the microsecond pulsed plasma is not just higher than the nanosecond pulsed plasma at the same voltage, but the rise in energy with applied voltage is more steep as well. A higher dissipated energy entails a higher degree of dissociation of the liquid in which the plasma is ignited. Therefore it is presumed, that the microsecond plasma produces a more reactive liquid. At high voltages, the electrical noise emitted by the setup becomes increasingly disruptive to external electrical devices, which can not be completely contained by the Faraday cage surrounding the plasma setup. Therefore, an operating voltage of 20 kV was chosen to ensure reliable ignition and minimize electrical disturbances for a lot of the following measurements.

The energy dissipated by the plasma is converted into the production of reactive species. To produce a chemical reaction between the plasma-activated water and the copper at the solid-liquid-interface, it is advantageous to prepare PAL with a high concentration of reactive species. It can be presumed that a long treatment time of the liquid is necessary to achieve this. For this reason, it is examined how the ignition and the dissipated energies develop over time. This is shown in figure 21:

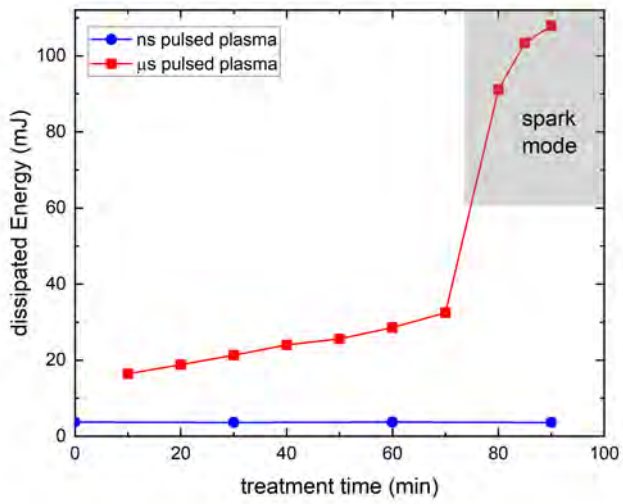

Figure 21: Dissipated energies of the microsecond pulsed plasma (red) and the nanosecond pulsed plasma (blue) at 20 kV over time. The transition into spark mode of the microsecond plasma is highlighted in gray. Adapted from [89].

Here, both plasmas were operated at 20 kV in distilled water. In the µs case, the initial dissipated energy is 16 mJ, while in the ns case it is at only 3 mJ. Over time, the dissipated energy of the ns plasma remains stable over the course of 90 minutes. In the µs plasma however, the energy steadily increases to 32 mJ after 20 minutes. Strikingly, the dissipated energy increases significantly after about 75 minutes in case of the microsecond plasma. At this point, the plasma transitions from the streamer-like mode to a spark mode. This can be explained by an increase in conductivity of the plasma treated water and the increasing bubble formation over such long treatment times. The plasma causes an increase in charged reactive species and solvated electrons on short time scales.

When a critical conductivity is reached, the streamer is able to extend to the counter electrode, a voltage drop occurs and a spark is initiated. The same observation has been made by other groups with similar setups [20]. Other factors like electrode distance and temperature of the liquid also have a significant influence on this transition and the critical conditions for the transition are hard to determine. Due to electrode erosion, the electrode distance increases over time. Additionally, due to Joule heating at the ignition site, the temperature increases with time. An effort was made to keep the electrode distance at 1 cm where the spark mode was achieved at a conductivity of 8-11 μS/cm. To produce the plasma-activated water for chemical and surface analysis and ensure consistency in the process, the plasma is typically operated for one hour. In the next section, the plasma activated water is characterized. Temperature, conductivity, and electrode erosion are investigated.

4.2 Properties of the Plasma Activated Water

The treated water is changed during plasma treatment. Since the plasma induces water splitting, ionization and recombination, the liquid contains many reactive species with varying lifetimes. These new neutral reactants and ions increase the chemical reactivity and the conductivity of the liquid. Bubble formation and a change in temperature also need to be taken into account, especially for long treatment times. The chemical properties of the PAL generated by both the microsecond and nanosecond plasma are presented in this section.

4.2.1 Temperature, Conductivity and pH Value

The temperature of the liquid influences the chemistry in the liquid and at the liquid-solid interface, as some decomposition reactions of important reactive species are temperature dependent. The conductivity reflects the presence of ions and can be an indication of the reactivity of the liquid. The nanosecond and microsecond plasma are therefore compared in this regard. In figure 22 a) and b) the change in temperature and conductivity of distilled water during the plasma treatment is shown. The first was operated at 20 kV and 50 Hz and the later at 20 kV and 100 Hz, for 90 and 50 minutes, respectively. The measurements are presented in dependence on the applied plasma pulses.

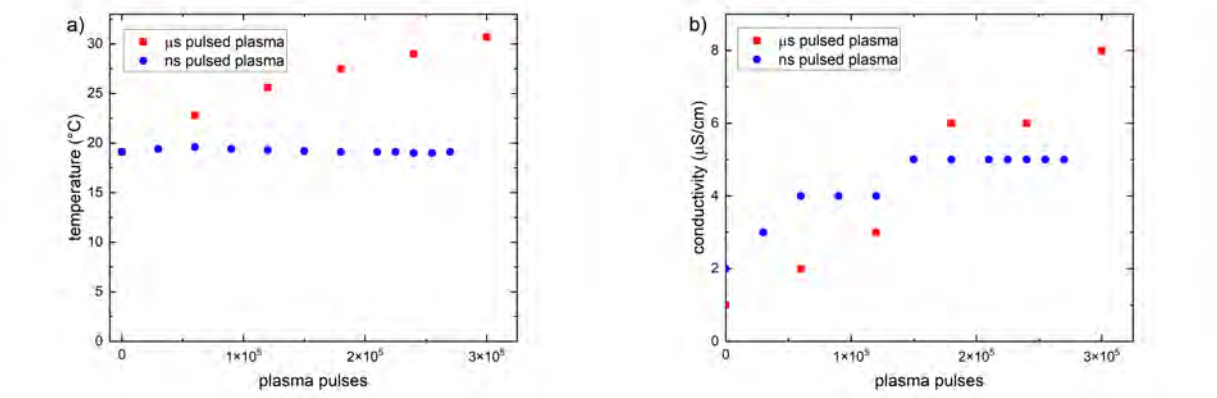

Figure 22: Development of the global temperature a) and conductivity b) of the microsecond (blue) and nanosecond (red) pulsed plasmas in dependence of the applied plasma pulses. Both plasmas were operated at 20 kV.

In both cases, the temperature of the liquid before plasma treatment is 19°C since the liquid is stored at room temperature. When the the microsecond plasma is used, the temperature steadily increases from 19°C to 30°C. In contrast, the nanosecond plasma does not heat the liquid significantly and the temperature remains at 19°C. This can be easily explained by the different pulse lengths. While the high voltage pulse is applied to the electrode, the electrode material locally heats up. This in turn causes heating and evaporation of the surrounding liquid. A longer pulse length therefore results in a longer heating time and increased evaporation.
With this, the energy converted heating the liquid can be calculated. The energy required to heat a liquid can be calculated according to:

$$E = \Delta T \cdot m_{liquid} \cdot c_{H_2O}. \tag{37}$$

Here, ΔT is the difference in temperature, m_{liquid} the mass of the heated liquid and c_{H_2O} = 4184 J/kg/°C the specific heat capacity of water. Over the $3{\cdot}10^5$ pulses, the microsecond plasma delivers 6300 J to the system, while in the nanosecond plasma case, 900 J are dissipated at the same pulse number. If all energy was converted into heat, the microsecond plasma could increase the temperature of the liquid over ΔT= 60 °C and the nanosecond plasma over ΔT = 8 °C . However, the microsecond plasma causes a temperature increase of ΔT = 11 °C while the ns plasma causes no temperature increase. This suggest, that not all energy is consumed by heating and loss mechanisms counteract the heating.

To heat the liquid volume of 25 ml over the 11°C, 1150 J are required. This is 18 % of the dissipated energy from the microsecond plasma over the $3{\cdot}10^5$ pulses. If the nanosecond plasma can also convert 18 % of the energy into heat as the same loss mechanisms would be present, it would expend 162 J to heating. To heat the 25 ml of water 1 °C, 105 J are needed. However, the temperature does not increase even one degree. This suggests that the nanosecond plasma does not just dissipate less energy than the microsecond plasma but that it also converts less of its energy into heat.

A distinctive difference between the two plasmas can also be seen when comparing the conductivity of the liquids. The distilled water has a conductivity of 1 µS/cm before plasma treatment. In the microsecond case, the conductivity increases to 8 µS/cm over the treatment time while the nanosecond PAW only increases to 5 µS/cm. This indicates, that both plasmas cause the generation of ions but the microsecond-pulsed plasma induces more water dissociation due to its higher dissipated energy. The increase in conductivity indicates an accumulation of reactive species over time in the plasma activated liquid. This includes both long-lived and short-lived species.
Distinguishing the types of reactive species in the liquid is an elaborate task, but species that are of interest and easily detected by a pH test are hydrogen ions. In figure 23 the development of the pH value of the plasma-treated distilled water for both plasmas is shown. The pH was monitored over the course of one hour. Both plasmas were operated at 20 kV and 15 Hz. The pH was measured with pH indicator strips from Supelco, sensitive in the range of pH 0-14. Their sensitivity is specified as pH 0.5.

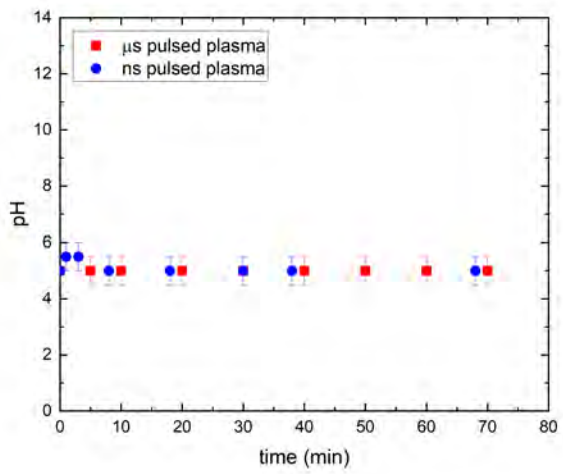

Figure 23: Development of the pH value of the microsecond pulsed plasma (blue) and nanosecond pulsed plasma (red). Both were operated at 20 kV and 15 Hz. Microsecond measurement adapted from [92].

Notably, an increase in pH could not be detected for either experimental setup. This may indicate that the increase in conductivity is not caused by an accumulation of hydrogen ions in the liquid. As a short-lived species, H^+ may have already decomposed in the time it takes to drain the reactor and to perform the pH test, most likely via

$$H_2O + H^+ \longrightarrow H_3O^+. \tag{38}$$

Therefore, H^+ also has no influence on the conductivity measurements, as the reactor also needs to be drained for this measurement. The hydrogen ions can therefore be excluded as possible reactants in later long-term treatments of copper samples, as discussed in a later section. Measuring the pH value is also relevant for the influence of the PAW on the copper, since it also has an influence on the reactivity and oxidative state of the metal.

The most abundant long-lived compound created by the plasma, and therefore the most easily detected compound, is hydrogen peroxide. The measurement of H_2O_2 and the comparison of the two plasmas in regards to its production are discussed in the following section.

4.2.2 Hydrogen Peroxide Production

Even though hydrogen peroxide is considered a long-lived species by PAL standards, it is still reactive and its concentration decays over time. This process is facilitated at increased temperatures. A decay constant of 1.5 µmol/l/h has been found for the storage conditions used over the course of this project.
In figure 24 the hydrogen peroxide concentrations produced by the microsecond and nanosecond pulsed plasma are compared. Distilled water was used in both cases and the plasmas were operated at 20 kV for one hour for each sample. The frequency was varied between 10 - 100 Hz in the microsecond case and 10 - 50 Hz in the nanosecond case.

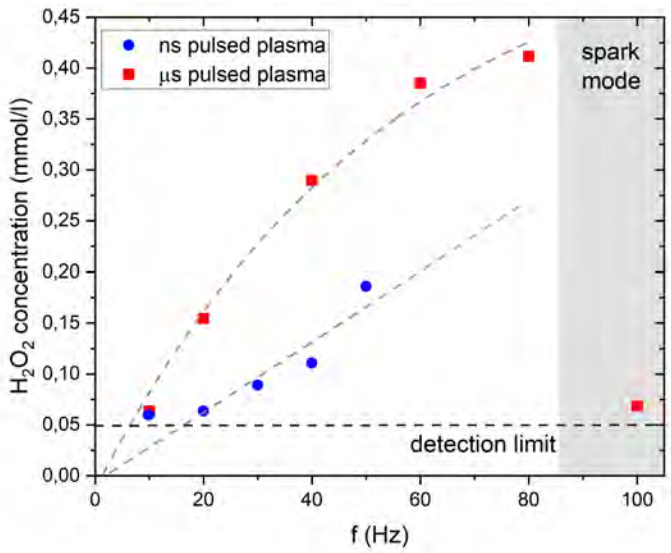

Figure 24: Hydrogen peroxide concentrations of the plasma activated water of the nanosecond pulsed plasma (blue) and microsecond pulsed plasma (red) at varying frequencies. The spark mode is highlighted in gray. In both cases, the samples were treated for one hour at 20 kV [89].

For both the nanosecond plasma and the microsecond plasma a concentration of 0.06 mmol/l H_2O_2 was measured at 20 kV and 10 Hz after one hour of treatment time. However, since the detection limit of the used detection method is 0.05 mmol/l it can not be assumed, that the production of both plasmas is the same at these settings. With increasing frequency, the concentrations increase for both cases. It is possible to produce more hydrogen peroxide using longer plasma pulses. However, when the

dissipated energies are taken into account and we calculate the production efficiency, we arrive at 0.5 g/kWh for the nanosecond plasma and 0.2 g/kWh for the microsecond plasma. The nanosecond plasma produces H_2O_2 more efficiently, while the higher absolute concentration is reached by the microsecond plasma.

Notably, in the microsecond case the concentration sharply decreases when the plasma is operated at 100 Hz. For this particular measurement, the plasma had transitioned into a spark mode, as described above. With this change in plasma conditions, the heating of the liquid also drastically increases. As hydrogen peroxide is sensitive to high temperatures, it can be assumed, that in the spark mode, a large amount of the previously produced H_2O_2 is quickly destroyed, leading to the sharp decrease in concentration.

The H_2O_2 production of the nanosecond plasma has previously been investigated by Chauvet et al.[47]. For their study, the same plasma setup was used while the detection method, absorption spectroscopy using a non-commercial self-assembled detection setup, was different. The group determined a linear increase of the H_2O_2 concentration with time, voltage and frequency, concluding that the hydrogen peroxide production is the same for each plasma pulse. In contrast, for the microsecond pulsed plasma the concentration does not increase linearly but seems to reach a plateau above a frequency of 80 Hz. The concentration saturating at 0.4 mmol/l may be caused by to the steady increase in temperature. As the frequency increases the temperature of the liquid increases and the decomposition of the hydrogen peroxide counteracts its production. The H_2O_2 yield of the nanosecond plasma was determined to be 2 g/kWh by Chauvet et al., four times higher than in this work. This can be attributed to the difference in detection methods. Regardless, it can be stated that the nanosecond plasma has a higher production efficiency, the microsecond plasma, however, yields the higher absolute concentration. To maximize the reactivity of the liquid, the microsecond plasma needs to be operated at high frequencies for long times while avoiding the transition into the spark mode as to not destroy hydrogen peroxide by the rapid increase in temperature.

Within the scope of this work, an effort was made to begin the investigation of the spark conditions of the microsecond plasma to optimize the hydrogen peroxide production. It is suspected, that the transition depends on the evaporation and bubble formation of the liquid. In figure 25a) an image of the plasma reactor after 27 minutes is shown. The bubbles were photographed over the course of 30 minutes, the plasma was operated at 20 kV and 100 Hz. The bubbles were highlighted by hand and their size and the bubble count and were determined using ImageJ and are depicted in 25b).

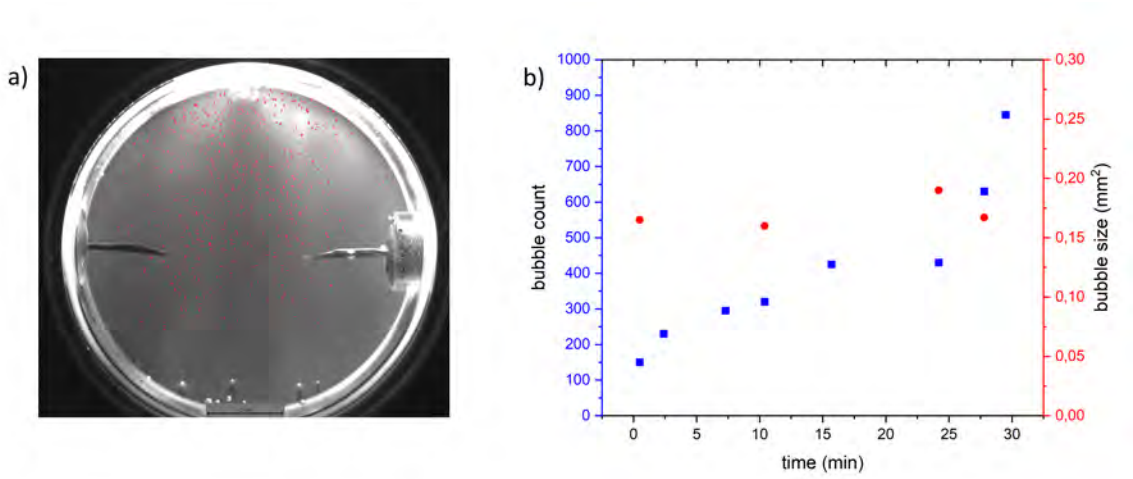

Figure 25: Bubble formation in the microsecond plasma. In order to determine the number and size of the bubbles, they were photographed and highlighted by hand a). The bubble count and size were recorded over a treatment time of 30 minutes at 20 kV and 100 Hz b). Adapted from [92].

The amount of bubbles continuously increases over the course of the treatment time, while their size remains between 0.15 mm^2 to 0.19 mm^2. At these parameters, the spark is typically observed after about one hour of treatment time. This leads to the assumption, that a critical number of bubbles needs to be present in the electrode gap. In the future, this subject should be explored further to determine the spark conditions.

4.2.3 Nanoparticle Production

Another influence on the hydrogen peroxide concentration that needs to be discussed is the presence of metallic electrode material in the treated liquid. While operating the in-liquid plasma over longer periods of time, it quickly becomes evident, that the electrode tip shortens and regularly needs to be replaced. It is assumed, that the material must be present in the liquid in the form of particles in the size range of some nanometres. It is possible, that these metal particles influence the liquid chemistry as tungsten oxides are able to catalyse the decomposition of H_2O_2. Additionally, the nanoparticles may deposit onto the copper surfaces. This is discussed in the following section.

In figure 26, SEM images of some tungsten electrode tips before and after plasma operation are shown. When preparing a fresh electrode, the tungsten wire is cut at an angle to create a sharp edge to facilitate the ignition. This can be seen clearly under the SEM. Over time, the plasma operation causes the electrode tip to reshape itself into a hemispherical surface. After plasma operation, small protrusions with a diameter of 5-10 nm can be seen. This effect increases at higher voltages. The creation of these protrusions can be explained by the rapid heating and cooling of the electrode. During each ignition, the boiling temperature of the material, in the case of tungsten 6203 K, is reached locally [56]. The electrode material boils and some of the metal is released into the surrounding liquid. The liquid in turn cools the electrode and the metal solidifies again, leaving behind a protrusion.

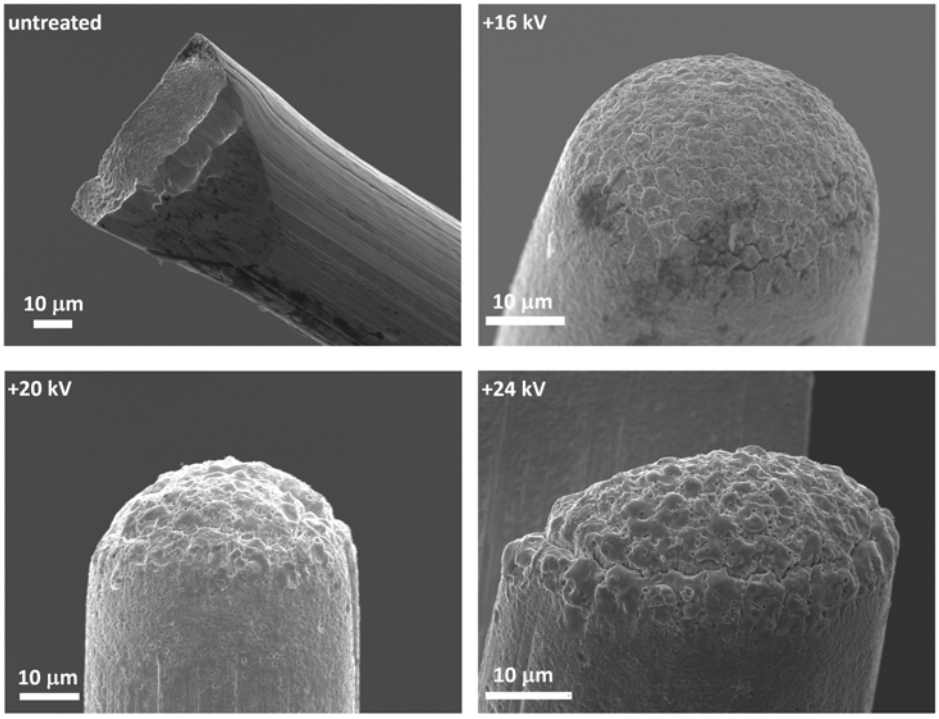

Figure 26: SEM images of the tungsten electrode tips before and after nanosecond pulsed plasma operation at different voltages. Splitting of the wire was frequently observed. Adapted from [93, 94].

To create a 5 µm wide and 1 µm thick protrusion, $3 \cdot 10^{-4}$ mJ are necessary to melt the material and an additional $8 \cdot 10^{-4}$ mJ are needed to evaporate the tungsten [93]. This lies far below the dissipated energies of $1 - 5$ mJ determined from the measurements as shown in the previous section. To evaporate and dissociate the water surrounding the presumed protrusion area, energies of 0.14 mJ and 3.5 mJ are needed, respectively [93]. This estimation implies that the majority of the energy dissipated by the plasma is converted into water dissociation.

In figure 27 a), the average removal of electrode material in nm/per ignition over 30 minutes of treatment time at +24 kV and -24 kV is shown. These rates were measured for the nanosecond plasma. It is evident, that the erosion is a relatively steady process and remains at 2-5 nm/ignition for both polarities. Only in the first few minutes, more material seems to be removed. This can also be explained by the preparation process of the electrode tips. When the tip of the tungsten wire is still sharp, as shown in figure 26, the electric field and therefore the dissipated energies are high. After the first few

minutes of operation have gone by, the electrode tip has been reshaped by the melting process and the erosion rate equalizes.

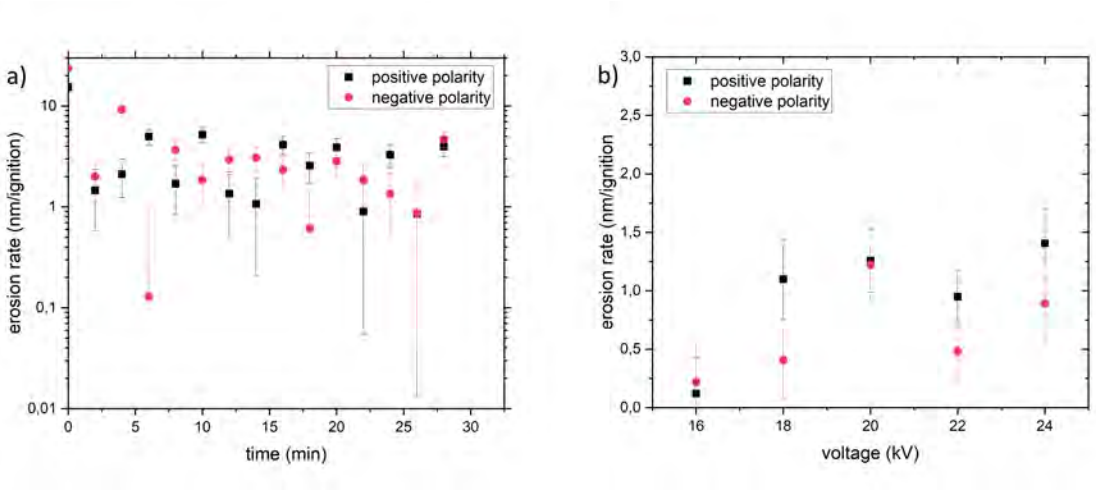

Figure 27: Erosion rates of tungsten electrodes in removal of nm per ignition: a) erosion for +24 kV and -24 kV over 30 minutes of treatment time and b) erosion for varying voltages between 16 and 24 kV for both polarities at 3 hours of treatment time. The frequency was set to 15 Hz in both measurements. Adapted from [93, 94].

In figure 27 b), the average erosion rate of the electrode is depicted at varying voltages. The nanosecond plasma was operated for three hours at 15 Hz and the voltage was varied between 16 and 24 kV at positive and negative polarity. It can be seen, that the erosion of the electrode material is higher for positive voltages. Additionally, the erosion increases for both polarities for increasing voltage. The highest erosion rate was achieved at +24 kV with 1.4 nm/ignition.
In figure 28 some nanoparticles produced by the nanosecond plasma are shown. The plasma was operated for three hours at 15 Hz and each sample was produced at different voltages, namely 20, 22 and 24 kV at positive polarity. From the images, it is evident that the size of the nanoparticles varies with voltage. At 20 kV, the particles have sizes of around 25 nm, the largest being 50 nm. At 24 kV, they appear to be much smaller, between 5-10 nm.

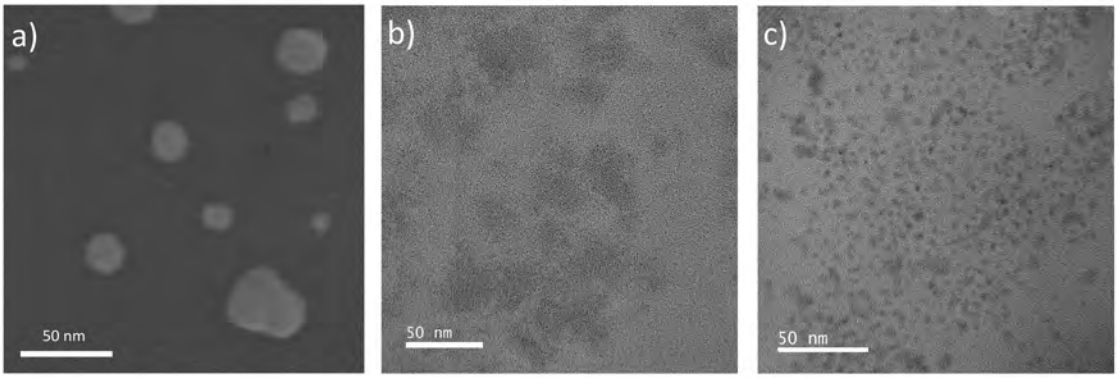

Figure 28: TEM images of nanoparticles created by the nanosecond-pulsed in-liquid plasma operated at 15 Hz for 3 hours at varying voltages: a) 20 kV, b) 22 kV and c) 24 kV. Adapted from [93]. Measurements performed by Dr. Paolo Cignoni.

The size distribution of the nanoparticles can also be quantified from the TEM images, which is shown in figure 29. It becomes clear, that higher voltages cause the formation of smaller nanoparticles.

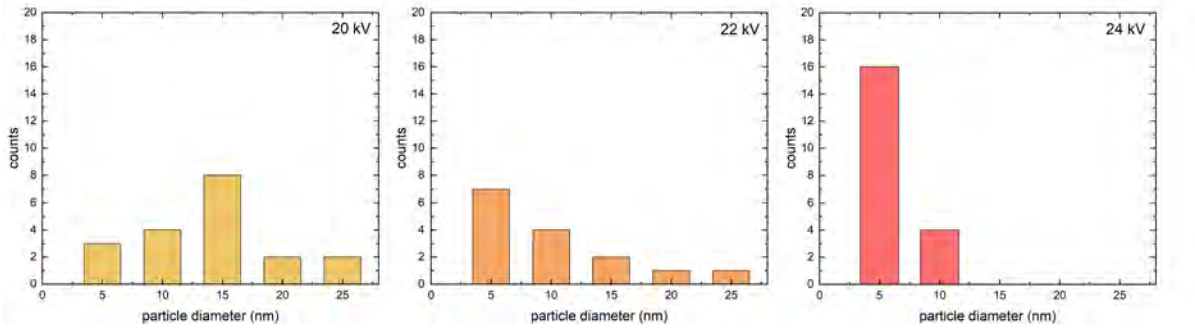

Figure 29: Particle distributions of the tungsten nanoparticles determined from the TEM images at 20 kV, 22 kV and 24 kV produced at 15 Hz and 3 hours treatment time.

To verify that the found nanoparticles consist of tungsten, XPS analysis was performed on the samples. For this purpose, the $4f_{7/2}$ peak was observed. The resulting spectrum is shown in figure 30. It shows, that both tungsten and tungsten oxide can be found in the plasma activated water. In addition, both copper and carbon can be found on the samples, as these are the constituents of the carbon support film. It could be

determined, that the nanoparticles consist of about 35% of metallic tungsten and 65% of tungsten trioxide (WO_3).
It can be assumed, that the surface of the electrode is oxidized by the water or PAW. In the PAW, plenty of oxidizing species are present causing the reaction. The expelled electrode material originates from the electrode tip and therefore mainly consists of WO_3. The bulk material quickly re-oxidizes as it is repeatedly heated and cooled. This oxidation may occur in between the plasma pulses and after plasma treatment.

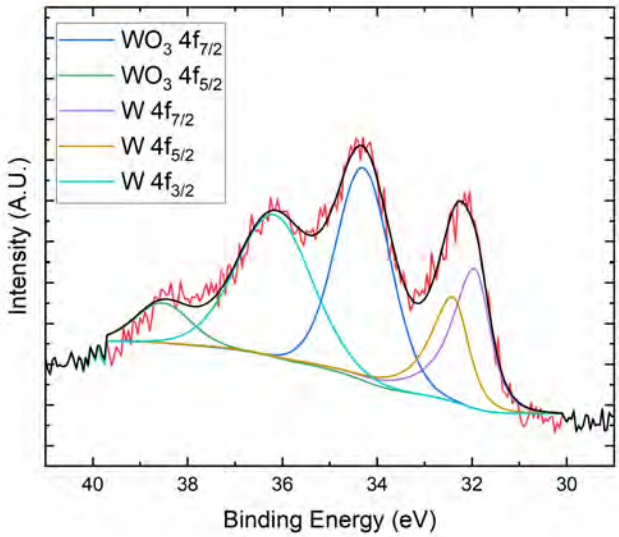

Figure 30: XPS spectra of W 4f 7/2 lines of tungsten nanoparticles produced at 24 kV for 3 hours. Adapted from [93].

Based on these observations, a production mechanism for the tungsten nanoparticles can be derived [93]: As the plasma is ignited, rapid heating of the electrode causes the formation of a bubble at the electrode tip. A high pressure region in the range of 1 GPa forms at this location. This assumption is made based on shock wave behaviour and velocities investigated in previous work on the setup [23]. The temperature during this initial bubble state is assumed to be at least 7000 K, the boiling temperature of tungsten and surpassing the boiling temperature of tungsten trioxide. At these conditions, the water vapour is initially in a supercritical state and evolves into a subcritical state as the bubble expands. As the topmost layer of the electrode is locally reaching boiling temperature, the material is expelled into the rapidly expanding vapour

bubble. A supersaturated vapour develops. In this state, first nucleation and then coagulation of the tungsten and tungsten oxide can occur. For both processes, the temperature of the vapour is a limiting factor, so as the bubble expands and the temperature decreases the coagulation process diminishes and the size of the nanoparticles reaches a maximum. The applied voltage has an indirect influence on the particle size by influencing the bubble formation and expansion. At higher voltages, the vapour bubble expands faster and the time for coagulation of the tungsten is shortened, leading to smaller tungsten nanoparticles.

4.3 Direct Plasma Treatment of Copper

The main goal of this work is to explore the pulsed in-liquid plasma as a possible tool for copper oxide nanocrystal creation. The influence of the microsecond and the nanosecond plasma on copper is presented in the next section. A distinction is made between direct plasma treatment, where the samples are placed in the vicinity of the plasma and indirect treatment, where the copper is treated using PAW. In this way, the effect of the long-lived reactive species in the PAW can be distinguished from the effect of the short-lived species. The direct plasma influence was investigated using FTIR spectroscopy and XPS analysis. To examine the PAW influence, XPS, cyclic voltammetry and SEM imaging is used.

4.3.1 In-Situ Surface Monitoring

FTIR spectroscopy is used to monitor the influence of the nanosecond plasma. One advantage of this method is the possibility to monitor the surface changes in-situ. In figure 31, the effect of the direct plasma treatment on a copper surface is shown. In figure 31 a) the measurement was performed on a 15 nm copper sample deposited on a silicon wafer and in 31 b) on a silicon oxide substrate. The measurements illustrate the impact of the chosen substrate on the surface changes. Both samples were treated at 20 kV and 1 Hz, the number of plasma pulses is indicated at the respective spectrum.

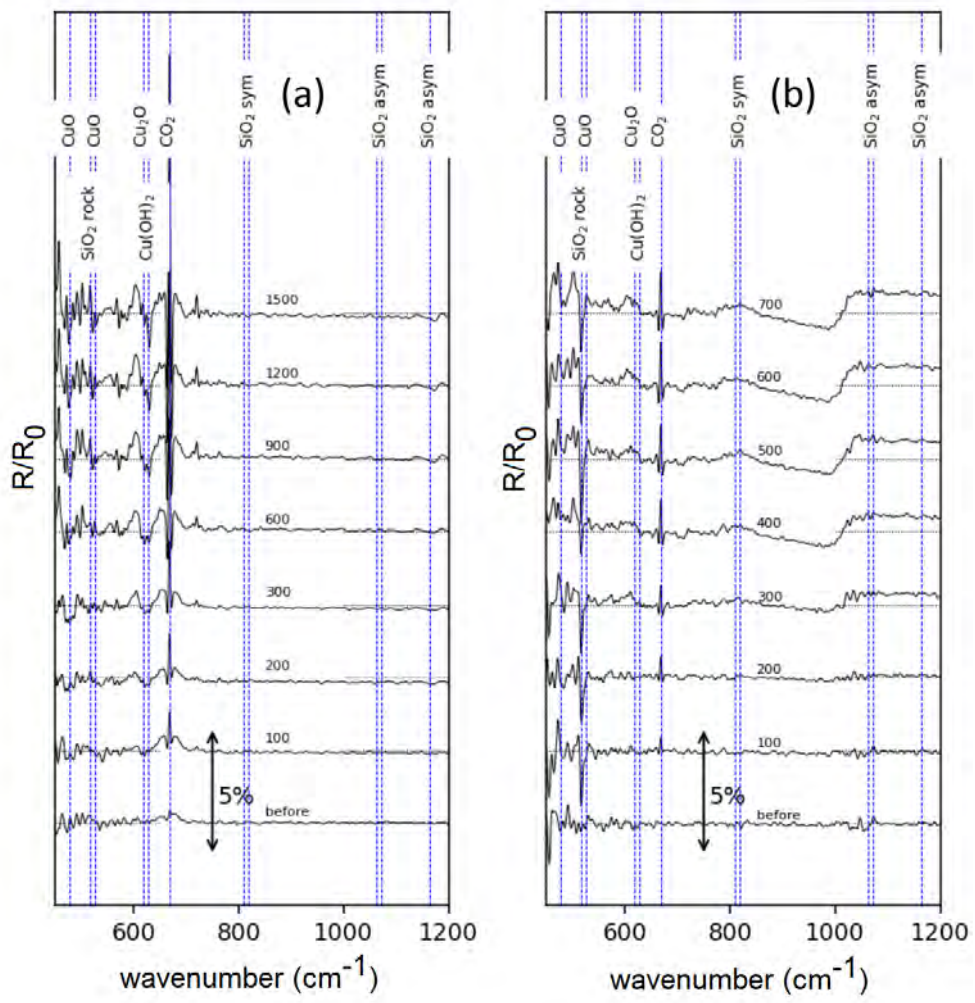

Figure 31: IR spectra for the in-situ plasma treatment of a 15 nm copper film deposited on a) a silicon substrate and b) a silicon oxide substrate. The applied voltage is +20 kV in both measurements and the labels indicate the number of plasma pulses delivered to the sample. Adapted from [95].

A distinct difference between the two cases can be seen in the wave number range of 1000 - 1300 cm^{-1}. In this range lies the rocking and stretching mode of the silicon oxide. When a silicon oxide substrate is used, an increase in signal can be seen in that range. In the case of pure silicon substrate, the signal in this range remains inconspicuous since no oxides are present. The appearance of the broad peak in the SiO_2 range indicates a removal of species. It is possible that the underlying SiO_2 substrate is reduced by the

plasma treatment or that the change in the copper layer that is in direct contact with the liquid, causes a change in reflectivity of the sample, making the silicon oxide visible in the spectrum.
In both scenarios, a peak at around 600 - 630 cm^{-1} appears, which corresponds to the line position of both Cu_2O and $Cu(OH)_2$, as they are positioned closely together and cannot be distinguished. An increase in signal indicates a removal of species.
First, this measurement establishes, that oxides must be present on the samples before plasma treatment. This can easily be explained by the manufacturing process of the samples: The copper coating is deposited onto the substrate via the HiPIMS process. After the coating is completed, the sample is removed from the HiPIMS reactor and installed in the plasma reactor. The copper sample is exposed to ambient air and to distilled water for some time before the plasma treatment can be initiated and has ample time to oxidize under these conditions. By the time the in-situ measurements have begun, a thin oxide layer has already formed on the surface and can be removed by the plasma.
Second, the measurements show, that the direct plasma treatment causes either a removal or reduction of oxides. No oxidation can be detected. A possible reaction pathway of the plasma-surface interaction was originally expected to be a conversion of CuI oxide into CuII oxide, increasing the oxidative state of the copper. However, in this case, the formation of a valley in the wavenumber range of 480 cm^{-1} and at 527 cm^{-1} should become visible. This could not be detected in either case, although the signal-to-noise ratio at the lowest detectable wavenumbers may have been too high to reliably measure in this range. The absence of CuO has been verified by other methods and will be discussed in a later section.

In figure 32, the FTIR signals of two copper samples on silicon substrate are compared, the first in 32a) was treated with the plasma at 20 kV and 32b) was installed in the reactor and only affected by distilled water and monitored for 15 minutes.

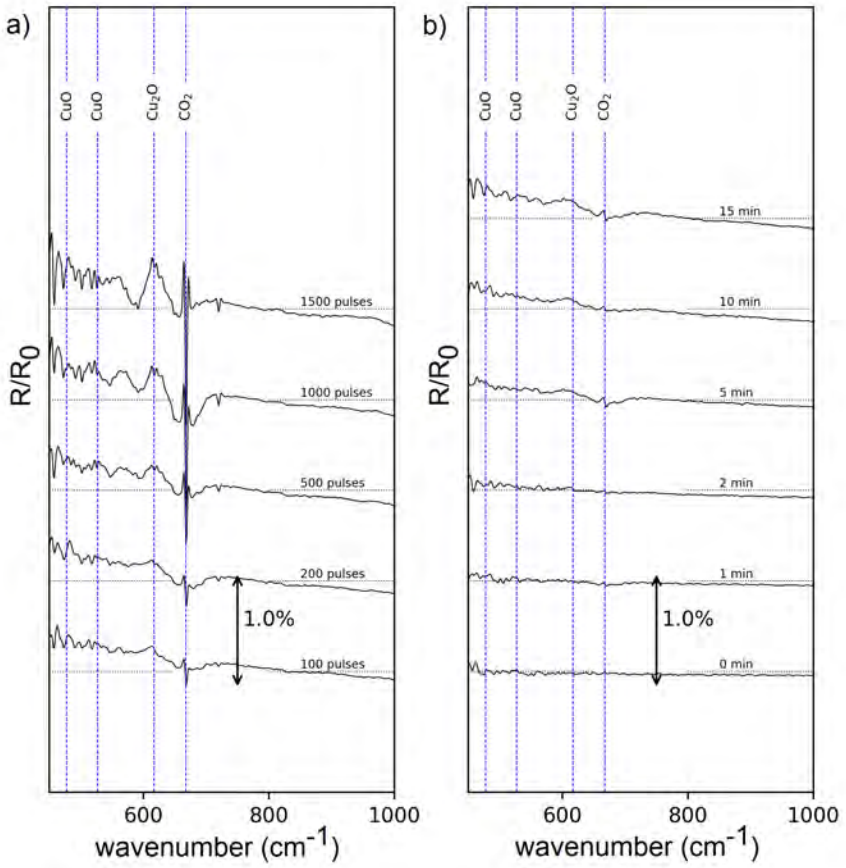

Figure 32: IR spectra for a) the in-situ plasma treatment of a 15 nm copper film on an Si substrate, the labels indicate the number of plasma pulses delivered to the sample, and b) treatment by distilled water for 15 minutes. Adapted from [95].

In both measurements the baseline of the signal seems to shift over time. This is attributed to the change in atmosphere in the beam path over time and is to be expected during all FTIR measurements. In the plasma treated sample, again the rise of the Cu_2O signal can be observed. However in the water treated sample, only a slight removal of the oxide is recorded. The removal of the copper oxide seems to be an effect that is provoked by the direct plasma treatment. It can be assumed, that the thin copper layer should oxidize in contact with water. However, this can not be confirmed in

this measurement. Additionally, there is a time window between the installation of the sample in the reactor and the beginning of the FTIR measurement. Apparently, the oxidation process happens on such a short time scale immediately after the copper comes into contact with water, that the process is already completed at the beginning of the measurement. The corrosion that sets in after full submersion is otherwise a slow process which becomes only slightly visible after 15 minutes.
To interpret the effect of the plasma treatment on the copper surface, a distinction needs to be made between the effect of common electrolysis and of plasma electrolysis. In the system used in this work, the plasma ignition is achieved at an applied voltage of 16 kV. Therefore, a measurement is next presented, where a 15 nm copper sample was treated first at +10 kV to mimic common electrolysis and then +24 kV to mimic plasma electrolysis. This is presented in figure 33.
For the first half of the experiment, where a voltage below the ignition threshold is applied, the experiment possesses a strong similarity to a bipolar electrolysis system [44, 45], where a floating metal workpiece is placed between the electrodes of an electrolysis setup. In this system, the electric field created between the working electrodes induces a current in the workpiece and causes the production of reactive species at the cathodic and anodic side. This causes half of the bipolar electrode to be oxidized and the other half to be reduced.

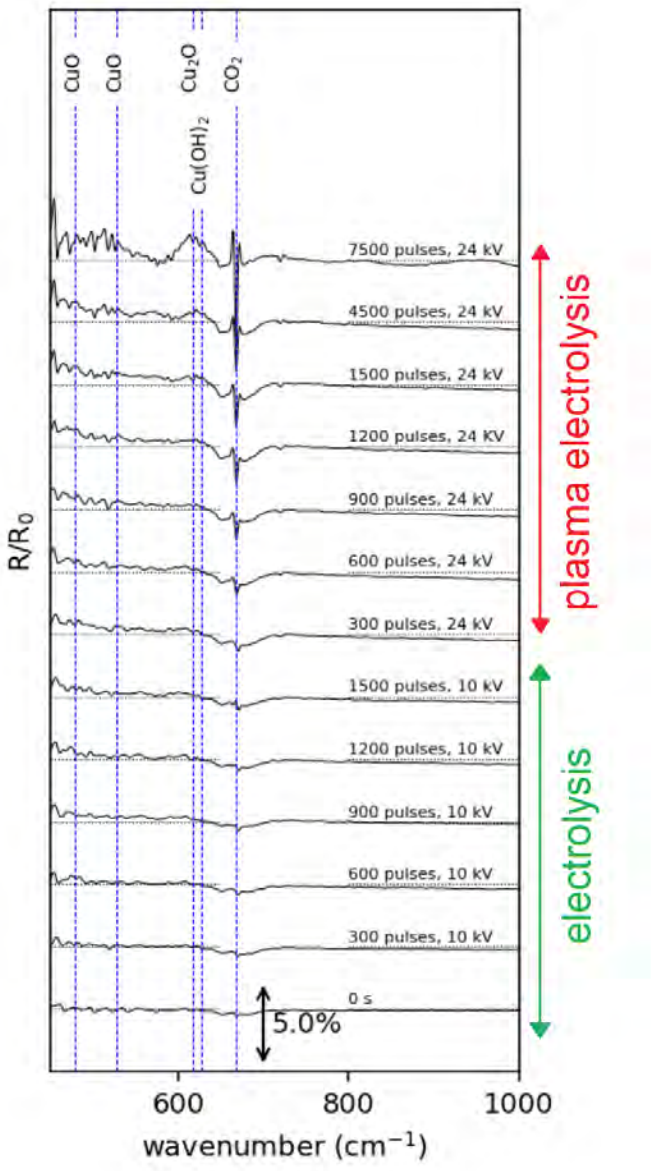

Figure 33: IR spectra for the in-situ treatment of a 10 nm copper film on silicon oxide by electrolysis at +10 kV and 10 Hz followed by plasma electrolysis at +24 kV at 10 Hz. Adapted from [95].

In the first half of the measurement, where the experiment is performed under electrolysis conditions, the signal does not change significantly, besides the slight baseline shift. No Cu_2O or $Cu(OH)_2$ seems to be formed or removed under these conditions. However, when the voltage is increased above the ignition threshold, after 1200 pulses, the typical copper oxide signal appears and oxide is removed. It is known that in plasma electrolysis the production of reactive species is enhanced compared to

regular electrolysis [46]. Additionally, the pressure waves originating from the plasma ignition accelerates the transport of reactive species to the copper sample. This may explain why the sample remains unchanged under electrolysis conditions, at least on the timescale investigated in this section. On the basis of these findings, the presence of bipolar electrolysis can be ruled out. If the experiment of this work resembled a bipolar electrolysis system, a change in the sample would be apparent even at 10 kV and both an oxidation and reduction could be detected in dependence of the electrode position. This dependence was also investigated, however not presented here because no connection was found between electrode position and surface changes.

4.3.2 Ex-Situ Surface Monitoring

The second method that was used to explore the direct plasma effects on copper was XPS analysis. The method is used to support the findings from the FTIR measurements and investigate the composition of the copper before it comes into contact with any liquid, which is unavoidable during the FTIR measurements. Additionally, the XPS method makes it possible to distinguish between $Cu(OH)_2$ and Cu_2O, which can not be done when using FTIR. In figure 34 the Cu2p spectra of an untreated copper surface and a surface exposed to direct plasma treatment are depicted. In figure 34 a), the untreated sample shows the $Cu2p_{3/2}$ and the $Cu2p_{1/2}$ peaks including a shake-up structure at around 942 eV. This shake-up indicates the presence of oxides on the surface. In 34 b), where the copper was treated by the ns plasma, the shake-up is absent. This indicates, that the plasma causes the removal of the oxide layer just as the FTIR spectra have previously displayed.

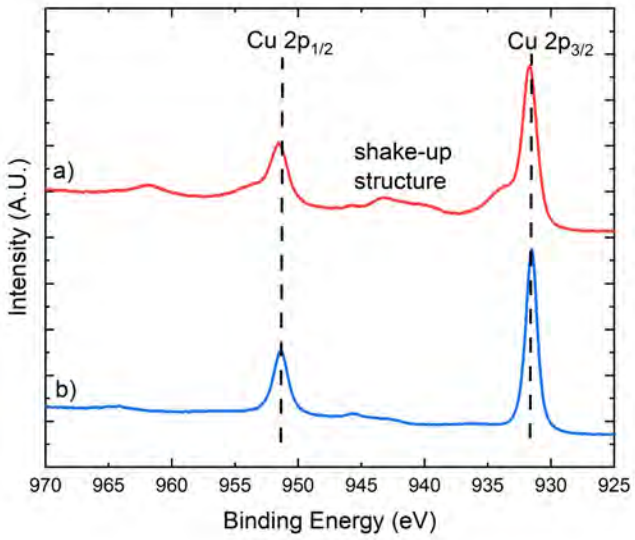

Figure 34: Cu2p spectra measured by XPS of a 50 nm copper film before plasma treatment a) and after 3 min of plasma treatment at 20 kV and 10 Hz for 3 minutes b). The spectra were shifted for legibility adapted from [95].

Notably, no signal originating from tungsten and its oxides could be found on the copper samples, indicating that the nanoparticles created from the electrode are present only at a low concentration in relation to the chemistry at the liquid-solid-interface of the copper samples.

Figure 35 depicts XPS measurements of two samples treated only by liquid. Here, 35 a) is a copper surface treated by ns PAW and 35 b) a control using distilled water. In both measurements, the spectra depict the $Cu2p_{3/2}$ and $Cu2p_{1/2}$ peaks including again the shake-up peak. Both surfaces have been oxidized by the liquids.

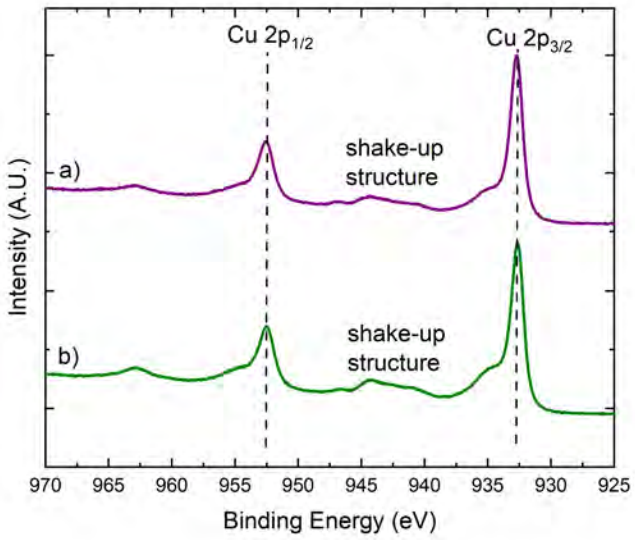

Figure 35: $Cu2p_{3/2}$ spectra measured by XPS of induced surface changes caused by a) treatment with plasma activated water and b) distilled water as control on a 50 nm copper film with a treatment time of 15 hours overnight. The spectra were shifted for legibility. Adapted from [95].

From the Cu2p spectra the presence or absence of oxides can be deduced, the oxidative state of the copper however can only be determined from an analysis of the Auger peaks of the samples. This is presented in the following section. In figure 36 the Auger spectra corresponding with the previously shown Cu2p spectra. The spectrum in 36 a) corresponds to an untreated copper sample, b) to a sample treated directly with the nanosecond pulsed plasma, c) to a sample treated with distilled water and d) to a sample treated with plasma activated water produced with the nanosecond setup.

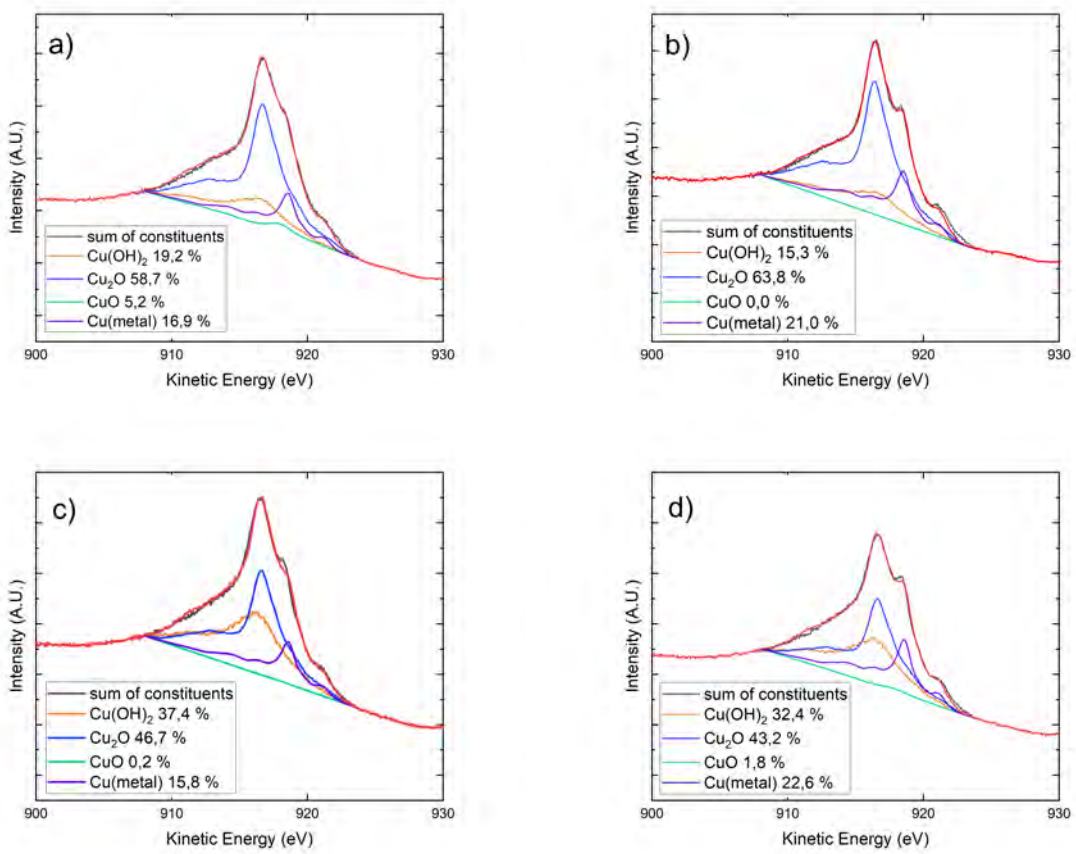

Figure 36: Auger spectra measured by XPS of four 50 nm samples film a) before treatment, b) after direct plasma treatment at 20 kV, 10 Hz and 3 minutes, c) after treatment with distilled water for 15 hours and d) treatment with nanosecond plasma activated water for 15 hours produced at 20 kV, 10 Hz for one hour. Adapted from [95].

From the Auger spectra the constituents of the samples can be quantified: The untreated samples consist mostly of Cu_2O namely 59%, 17% is metallic copper, 19% is $Cu(OH)_2$ and lastly 5% of CuO. When the sample is treated directly with the plasma, the proportion of metallic copper increases to 21%, the amount of CuO decreases to 0% and the oxides Cu_2O and $Cu(OH)_2$ increase to 64% and decrease to 15% respectively. The treatment with distilled water depicted in 36 c) causes no significant change in the amount of metallic copper when compared to the untreated sample, the amount being 16%. The amount of CuO again decreases to 0%. In this case, the amount of copper hydroxide increases to 37 % and Cu_2O decreases to 47 %. Lastly by treating the copper

with the PAW, the amount of metal is increased to 23%, the CuO again decreases to 2%, the $Cu(OH)_2$ increases to 32% and the amount of CU_2O decreases to 43%.
For a more straightforward comparison of the different treatment methods the proportions of the copper and the copper oxides are depicted in figure 37:

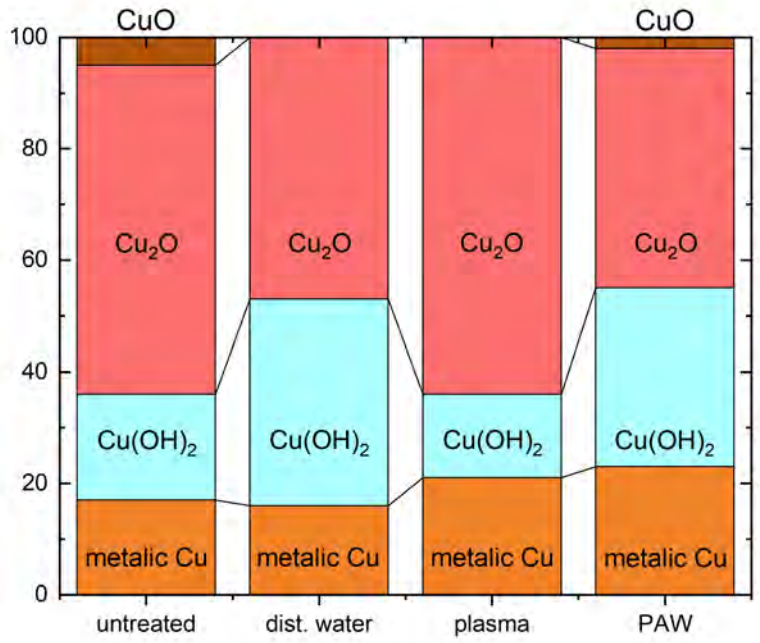

Figure 37: Quantification of the different constituents on the copper surface before treatment, after treatment with distilled water, direct plasma treatment and PAW influence. Adapted from [95].

On the untreated sample, the copper oxides most likely are created by oxidation through the samples coming into contact with ambient air after sample preparation. When the sample is treated with distilled water, the $Cu(OH)_2$ concentration increases while the Cu_2O decreases. The copper is oxidized further by the water. Since the water treatment takes place over many hours and the plasma treatment is performed quickly after installing the sample in the reactor, leaving the water only little time to influence the surface, the sample undergoing direct plasma treatment is compared to the untreated case. In this case, the amount of metallic copper on the surface increases, possibly due to $Cu(OH)_2$ being converted into Cu. This is confirmed by the FTIR measurements. However, the removal of the Cu_2O which was evident in the FTIR spectra, can not be

corroborated. A reason for this discrepancy may be the difference of information depth of the two techniques, since XPS only samples from the surface while the FTIR beam traverses trough the sample. A slight etching process may be elicited by the plasma (and its products) at the solid-liquid interface. It is possible, that the etching causes the total amount of Cu_2O to decrease, as seen in the FTIR spectra. At the surface, the sample is re-oxidized by the oxidizing species in the liquid and no change in the Cu_2O content is detected by XPS on the surface. When the sample is treated with the plasma activated water, both reduction and oxidation occur compared to the untreated sample. In this case the measurement is compared to the distilled water case, since both treatments happen on the same timescale. The amount of metallic copper increases while the $Cu(OH)_2$ decreases. In this scenario, the long-living species produced by the plasma must have a dominant influence, since the treatment is performed over multiple hours.

From the XPS measurements two things become evident: First, the treatment time has an influence on the modification of the copper samples. Second, the plasma and the plasma activated water need to be considered separately. The long term changes induced by the PAW are investigated by cyclic voltammetry and Scanning Electron Microscopy, which is presented in the following chapter.

4.4 Influence of Plasma Activated Liquid on Copper

In the following section, the effects of the PAW on copper are presented. Cyclic voltammetry and SEM imaging are used to determine the copper surface composition and morphology.

4.4.1 Composition and Surface Morphology

The long-term influence of the plasma activated liquid on copper can be investigated with the cyclic voltammetry measurements and the XPS results can be verified. Additionally, this method does not just give insight into the surface composition but can also give indications of the structure of the copper oxide.

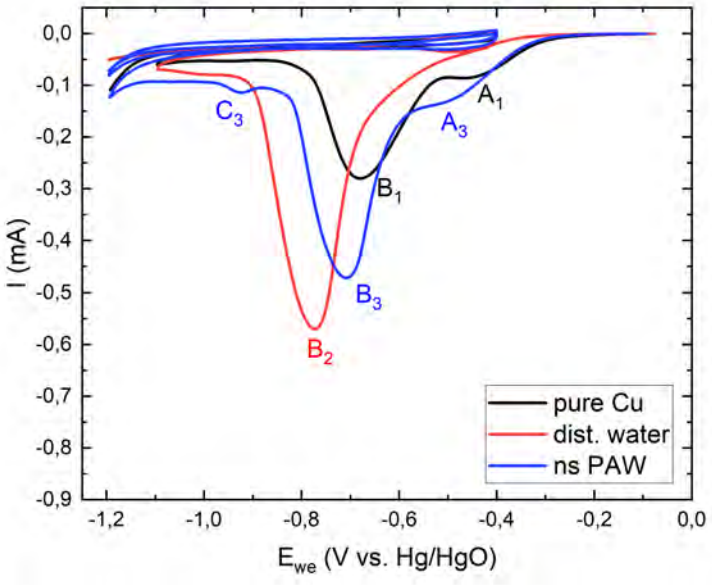

Figure 38: Voltammograms of an untreated copper sample (black), a sample treated with distilled water (red) and a sample treated with PAW produced with the nanosecond-pulsed plasma (blue). All samples have a thickness of 50 nm. Adapted from [89].

In figure 38, three voltammograms are shown: one has been recorded using an untreated copper sample, one was treated with distilled water and one was treated with plasma-activated water from the nanosecond-pulsed plasma. The untreated sample has been oxidised from contact with the ambient air and the voltammogram shows two

peaks. The main peak B_1 is located at -0.65 V vs. Hg/HgO and a smaller peak A_1 can be seen at -0.45 V vs. Hg/HgO. The A_1 peak has been attributed to different reduction processes in literature. It has been assigned to the reduction of Cu^{2+} to Cu^{+1}, however it can not be determined from the CV experiment alone, whether the initial oxidative state is CuO or $Cu(OH)_2$ [67, 96, 97, 98]. Based on the XPS results presented in figure 37, some amounts of of CuO and $Cu(OH)_2$ can be found on an untreated sample. Therefore the A_1 peak may be an indication of the reduction of either species.
The main peak B1 is attributed to the reduction of Cu_2O to Cu [96, 97, 98], most likely via the reaction:

$$Cu_2O + H_2O + 2\,e^- \longrightarrow 2\,Cu + 2\,OH^- \tag{39}$$

The height of the peaks is an indication of the amount of each species on the sample. The CV results corroborate the results from the XPS analysis, where the amount of Cu_2O found on the untreated sample was the largest, followed by $Cu(OH)_2$ and a small amount of CuO.
The curve from the sample treated with distilled water in red shows a shift of the main peak B_2 towards more negative voltages, at -0.8 V vs. Hg/HgO. In addition, the signal from Cu^{2+} reduction is absent here.
This second observation does not agree well with the results from the XPS analysis, as presented in figure 37. Here, the amount of CuO does decrease under the influence of distilled water in comparison to an untreated surface, but the amount of $Cu(OH)_2$ increases. The voltammogram shows only the reduction of Cu_2O. One explanation for this may be that the A_1 peak does only indicate the reduction of CuO, as some literature indicates [67, 99], as the absence of the signal does not signify the absence of the species. Some $Cu(OH)_2$ may be present on the sample and just not be detected in the CV in this range. Under the consideration of the complex water-copper system described in section 2.4, the presence of $Cu(OH)_2$ alongside CuO is very likely.

Some groups, Tran et al. and Gil et al., have related the shift in the Cu_2O reduction peak to a change in morphology of the copper [74, 100]. According to them, a CV at -0.65 V vs. SCE indicates the presence of Cu_2O in an amorphous state and at -1.0 V vs. SCE in a crystalline state. A signal between these two positions with a maximum at -0.81 V vs. SCE indicates the copper oxide is in an intermediate state. However, the groups performed their measurements in an acidic environment, while in this work a

basic electrolyte was used. In addition, different reference electrodes as in this work were used. The differences in electrolyte and pH lead to certain reactions being favoured or disadvantaged, and the results are therefore not directly comparable. Still, they show that the method can give insight into the surface structure of the copper, since a crystalline oxide is more stable and has a different reduction potential as an amorphous oxide.
When the copper is treated with plasma-activated water, as depicted in figure 38 in blue, the main peak B_3 shifts back to more positive voltages and the Cu^{2+} reduction signal reappears. This is in agreement with the XPS results, where the amount of CuO and $Cu(OH)_2$ increases in comparison to an untreated sample. Notably, a small peak appears at -0.95 V vs. Hg/HgO. At this voltage, Tran et al. and Gil et al. have also reported a signal that they have attributed to the presence of crystalline Cu_2O. This may indicate that the growth of copper oxide crystals is caused by the plasma activated water and is not induced by contact with water alone.

Since the plasma treatment seems to have a unique effect on the copper surface, it is plausible that the effect can be increased by varying the experimental parameters such as treatment time, frequency, voltage and pulse length. The later is presented in the following experiment.
In figure 39 the voltammograms of two PAW treated copper samples are shown: one was produced using the microsecond plasma in green and one using the nanosecond plasma in blue. The plasmas were operated at 20 kV and 10 Hz for one hour. At these operating settings, the H_2O_2 concentration of the nanosecond plasma is assumed to be below the detection limit, as depicted in figure 24.

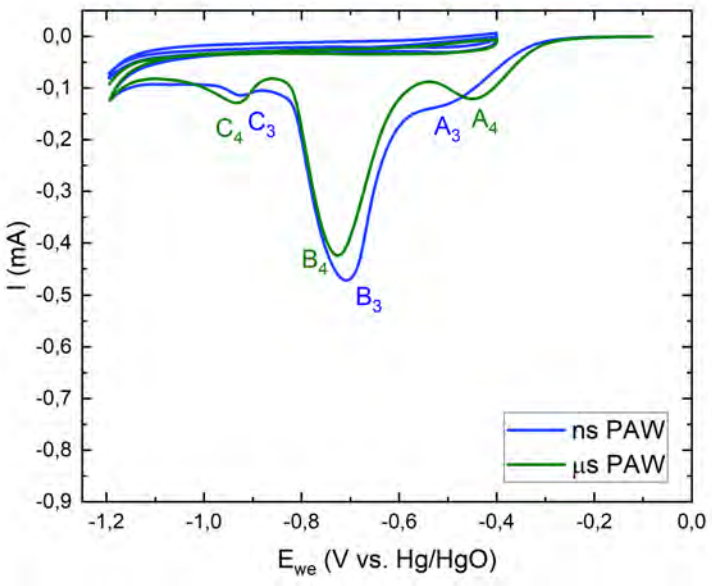

Figure 39: Voltammograms of two copper samples, one treated with nanosecond plasma activated water (blue) and one treated with microsecond plasma activated water (green). Both samples have a thickness of 50 nm, the PAW was treated at 20 kV and 10 Hz for one hour. Adapted from [89, 91].

It can be estimated, that the H_2O_2 concentration of the microsecond PAW is roughly twice the amount as in the nanosecond PAW. Both measurements show the main peaks B_3 and B_4 at a similar height and position and both show the Cu^{2+} reduction peak. The particular difference between the two voltammograms lies at around -0.95 V vs. Hg/HgO: The microsecond PAW treated sample shows a more pronounced peak in this region.

When comparing the characteristics of the two plasmas and the different liquid properties it becomes evident, that the PAW produced by the microsecond pulsed plasma contains a higher amount of reactive species. This effect is linked to the difference in dissipated energies between the two experiments: the higher the dissipated energy, the higher the reactivity of the liquid. This may be the reason, why the PAW from the microsecond plasma has a larger effect on a copper surface.

Since the dissipated energies of the in-liquid plasma increase for higher voltages, the effect of the voltage applied to the PAW is displayed in figure 40. Due to the microsecond plasma seemingly influencing the copper more severely, only the CVs of the microsecond plasma is presented here, since the changes on copper seem to be more easily detected and interpreted by the method.

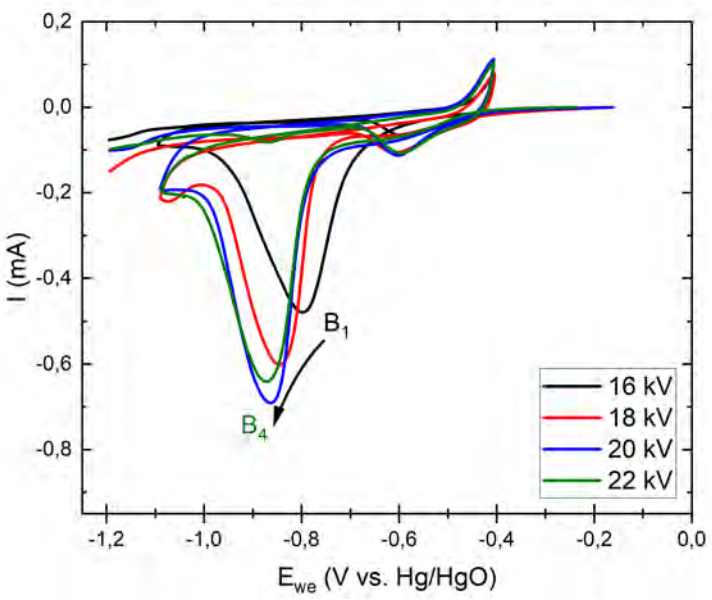

Figure 40: Voltammograms of four PAW treated copper samples. The liquid was treated using the microsecond plasma for 30 minutes and 50 Hz at 16 kV (black) 18 kV (red) 20 kV (blue) and 22 kV (green). All samples have a thickness of 50 nm. Adapted from [92].

In figure 40 it can be seen that the main Cu_2O reduction peak of the voltammogram shifts toward the crystalline region for higher voltages, being positioned at -0.79 V vs. Hg/HgO for the 16 kV curve and at -0.89 V vs. Hg/HgO for the 22 kV curve. This can again be explained by the increase in dissipated energy. More reactive species and primarily more hydrogen peroxide are being created at higher voltage, making the PAW more reactive and causing a larger change of the copper surface.

In the range of -0.4 V vs. Hg/HgO, a positive peak can be seen in these curves. The positive current is evidence of an oxidation reaction [99]. This peak is associated to the formation of Cu_2O via:

$$2\,Cu + 2\,OH^- \longrightarrow Cu_2O + H_2O + 2\,e^-. \tag{40}$$

As the measurement is first performed in the negative direction and then the positive direction, this oxidation reaction does not influence the analysis of the main peaks B_1 to B_4.
Since there is evidence of structural changes on the copper surface due to the indirect plasma treatment, it is necessary to investigate the copper using an imaging method, such as scanning electron microscopy. These SEM results are discussed in the next chapter.

4.4.2 Imaging of the Copper Oxide Crystals

Before considering the nanostructure of copper, a baseline for the condition of the samples before treatment is established by examining an untreated sample. In figure 41 a) an untreated copper surface, as deposited by HiPIMS, can be seen. The sample is evenly coated with the copper film and seems to be amorphous. Small, light coloured specs can be found on the sample, which most likely are composed of dust or debris either on top of the sample or underneath the copper layer, which are not removed prior to the coating process. The impurities can be found on most if not all samples and can not be completely avoided, as excessive cleaning of the sample before or after treatment can negatively impact the adhesion of the copper film or damage the copper oxide nanostructures. Besides, the impurities may play a role in the formation of the nanostructures.

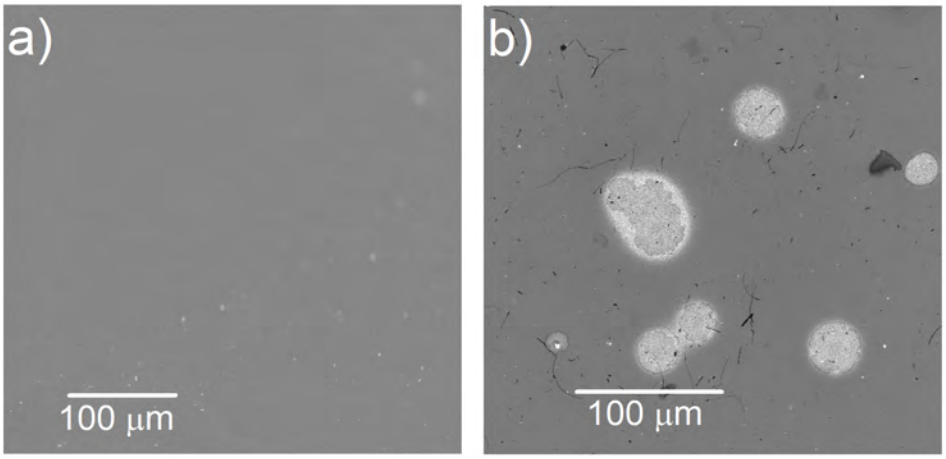

Figure 41: SEM images of a) a copper sample before treatment and b) oxidized copper surface treated with ns plasma activated water with the parameters 20 kV, 10 Hz, 30 minutes. Surface treated for 16 hours. Adapted from [95].

When the copper is treated with the plasma activated liquid, oxide islands can be found on the surface only in certain areas while the surrounded by copper rather than copper oxide. This can be seen in the SEM image 41 b), where a copper sample was treated with PAW (ns plasma, 20 kV, 10 Hz ,30 min) for 16 hours. These oxide islands suggest the presence of pre-existing seed regions on the surface such as impurities or irregularities, as observed in the CMP process, where H_2O_2 is used as an oxidant [26]. A dissolution mechanism and a subsequent precipitation of the copper (oxides) in those seed regions leads to the formation of the islands. Without the dissolution of the material, a consistent oxide film should form, which has not been observed in the PAW case.

In the next SEM images, the effect of distilled water on the copper surfaces is compared to the nanosecond PAW effect. In figure 42 a) the water-treated sample is shown. Here, clusters of copper oxide crystals can be found. They are irregularly structured and have a size between 0.1 to 0.5 µm. This is unexpected at first, since the cyclic voltammetry measurements did not indicate the presence of crystalline structures.
In figure 42 b) and c) two images of one sample treated with PAW are presented. Here, copper oxide crystals can be found as well. However, the structures are much more regular, one being tetrahedral and one hexahedral. They are about 1 µm in size, slightly larger than the crystals formed by distilled water. This may be the reason for the

discrepancy between the SEM and CV results: The smaller structures formed by the distilled water may have been detected in the voltammogram in the intermediate range while the larger structures from the plasma-activated water have a reduction potential in the crystalline range. Notably in figure 42 c), some smaller oxide crystals next to the large structure can be seen. This again points towards the presence of a seed region caused by an irregularity in this area, since the oxide structures seem to cluster in this spot.

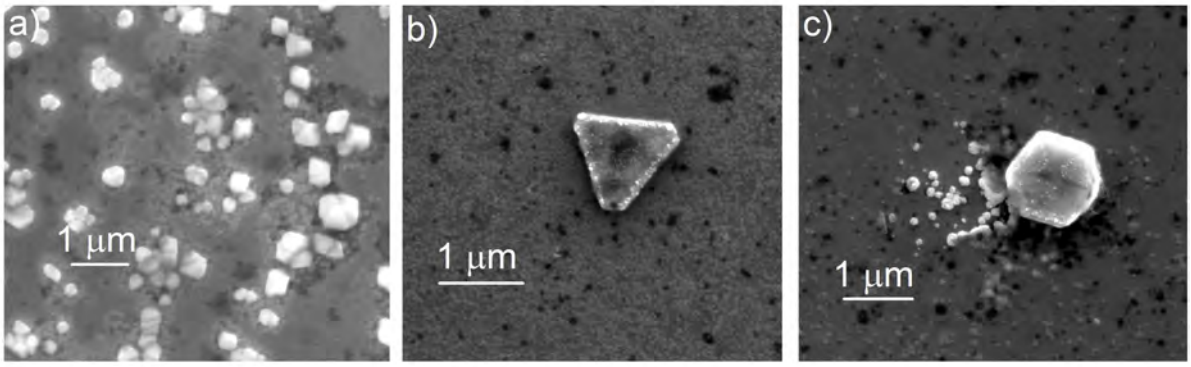

Figure 42: SEM analysis of three 50 nm Cu films after treatment with a) distilled water and b) & c) plasma-activated water generated at +20 kV at 10 Hz for 1 hour, sample treated for 4 h. Adapted from [95] and [89].

Since the effect of the microsecond plasma is more pronounced than of the nanosecond plasma in the voltammograms, the difference between them is again investigated using SEM. In figure 43, two images are shown, 43 a) shows again a sample treated with nanosecond PAW and b) treated with microsecond PAW. The nanosecond sample again shows an oxide crystal in a tetrahedral shape and a diameter of over 1 µm surrounded by much smaller oxide structures around 0.1 µm in size. The microsecond sample also displays copper oxide crystals of a similar size and shape while the smaller oxide structures surrounding the large crystals are around 0.2 - 0.25 µm in diameter, twice the size as in the nanosecond case. This may explain the larger reduction signal in the CV measurements. The larger oxide structures may result in a larger current during reduction.

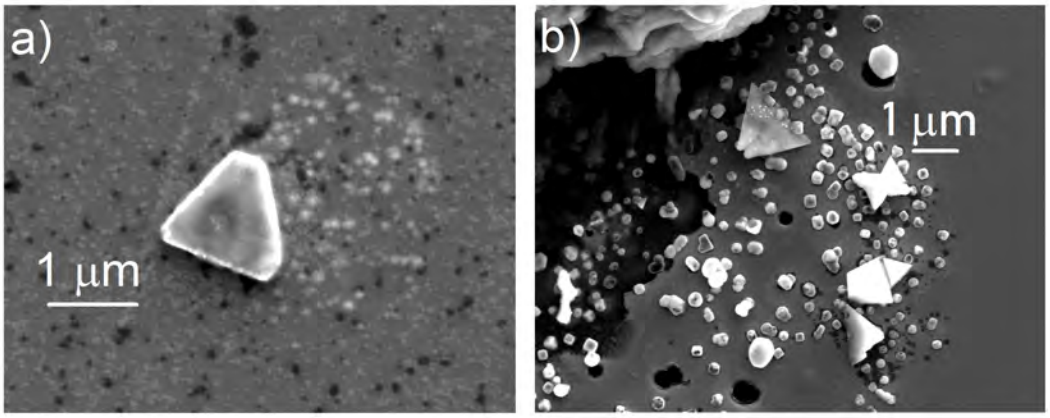

Figure 43: SEM images of two 100 nm Cu films after treatment with a) ns plasma activated water and b) µs plasma activated water. The ns plasma was operated for one hour at 10 Hz and 20 kV and the µs plasma for one hour at 100 Hz and 20 kV. The samples were treated for 3 hours.

In previous sections, the reason for the larger influence of the PAW compared to distilled water alone has been linked to the creation of reactive species by the plasma treatment. The most long-lived species present in the PAW is hydrogen peroxide. Since the treatment times to analyse the long-term effects lay in the range of hours, it is reasonable to assume that the effect of the PAW is really just the effect of the solvated H_2O_2 and could be achieved by a hydrogen peroxide solution in a similar concentration. This is examined by the next series of SEM images in figure 44, where three copper samples were treated with a) & b) distilled water, c) & d) a 0.2 mmol/l hydrogen peroxide solution and e) & f) plasma activated water produced by the nanosecond plasma. The concentration of the H_2O_2 solution corresponds to the concentration of H_2O_2 in the PAW produced by the nanosecond plasma after one hour and 50 Hz.

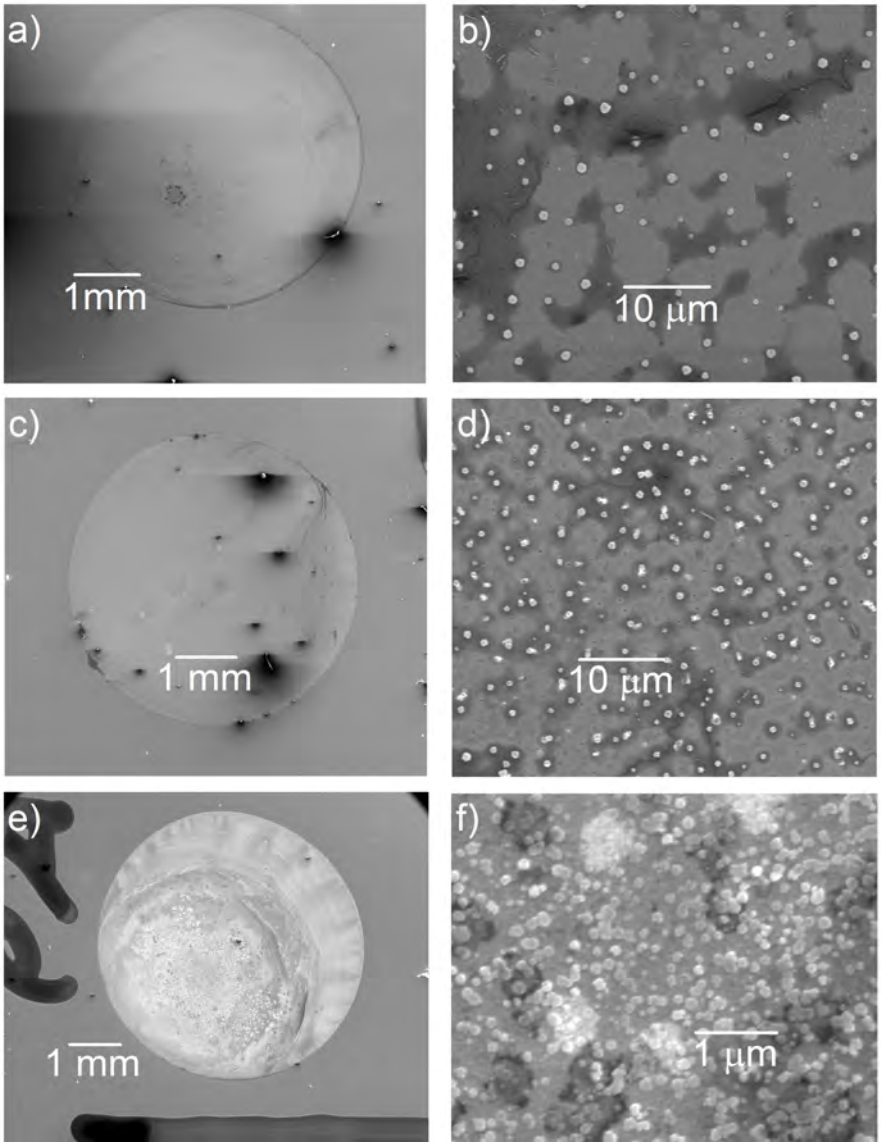

Figure 44: SEM images of three 50 nm Cu films after treatment with a) & b) distilled water, c) & d) 0.2 mmol/l hydrogen peroxide solution and e) % f) plasma-activated water, at two different magnifications. The PAW was generated at +20 kV at 10 Hz for 1 hour, the samples were treated for 4 hours.

In 44 a) the effect of distilled water on copper can be seen at the smallest magnification. The outline of the droplet is clearly visible. The affected area is slightly brighter than the untreated area, indicating oxidation. In 44 b) the magnification on the same sample has been increased, and now small copper oxide structures become discernable.
In 44 c) again the outline of the droplet is clearly visible but there is no apparent

difference to the water-treated surface at this magnification. However, in 44 d) the disparity between the two samples becomes clearer, there are more oxide structures present on the sample and they are slightly larger than in the distilled water case. The largest change on the surface can be seen in the PAW treated sample. In 44 e) the surface impacted by the drop is clearly oxidized and much brighter than the other two samples. In 44 f) again the magnification is increased and the amount of copper oxide crystals is much higher. At a treatment time of 1 hour and operation settings of 10 Hz and 20 kV the concentration of hydrogen peroxide in the PAW used in this measurement would be about 0.05 mmol/l according to the previously shown H_2O_2 measurements. This is only 1/4 of the prepared H_2O_2 solution used on the other sample. This indicates, that even on long timescales not just the H_2O_2 but also other reactive species must be involved in the oxidation process, since the diluted hydrogen peroxide does not have the same effect on the copper than the PAW, even at higher concentrations.
Based on the findings presented in this chapter, a possible oxidation mechanism of copper under the influence of plasma activated liquid can be constructed. This mechanism needs to take into account both the short-term and long-term effects of the PAW and the possible chemical reactions between the copper and the many different reactive species produced by the plasma treatment. This oxidation mechanism is presented in the next section.

4.5 Copper Oxide Growth Mechanism

From the measurements presented above, one can construct a possible oxidation mechanism of copper under the influence of plasma activated liquid. This scheme needs to fulfil three requirements:

- include an explanation for the reduction of copper on short time scales in the range of minutes and during direct plasma treatment as deduced from the FTIR and XPS results,
- account for the oxidation that takes place on longer timescales in the range of hours and during indirect treatment by the plasma activated liquid evident from the CV and SEM experiments, and
- explain not just the oxidation of the copper but also the formation of oxide crystals as opposed to planar oxidation clearly visible under the SEM.

The presence of these opposing findings implies the existence of two or more competing mechanisms acting on copper on different timescales. An untreated sample always contains oxides from contact with ambient air. The short-term reduction is likely a reduction of copper hydroxide (as it occurs during corrosion) into cuprous oxide and a reduction of the cuprous oxide to metallic Cu both initiated by the reactive short-lived species produced by the plasma. Multiple short-lived species are able to facilitate these reduction reactions such as solvated electrons, molecular hydrogen or hydrogen ions. However, the most likely reduction agent is H, since the reactive species need to be able to traverse the 1 cm distance between plasma and copper surface during the direct treatment. The reduction may follow:

$$2\,\mathrm{Cu(OH)_2} + \mathrm{H_2} \longrightarrow \mathrm{Cu_2O} + 3\,\mathrm{H_2O},$$
$$\mathrm{Cu_2O} + \mathrm{H_2} \longrightarrow 2\,\mathrm{Cu} + \mathrm{H_2O}\,\cdot$$

Additionally, erosion may be initiated by the pressure wave produced by the plasma where $\mathrm{Cu(OH)_2}$ is released into the liquid, revealing the metallic copper underneath. During plasma operation, the short-lived reactive species are continuously supplied to the system and the reduction is upheld during this time.

The long-term oxidation process can be based on the Chemical Mechanical Planarization (PME) process as described in more detail in section 2.4. It is facilitated by long-lived species such as hydrogen peroxide. Some reactions induced by long-lived species include:

$$Cu^{2+} + 2\,H_2O^- \longrightarrow Cu(OH)_2 + H_2 \tag{41}$$

$$2\,Cu + H_2O \longrightarrow Cu_2O + 2\,H^+ + 2\,e^- \tag{42}$$

$$Cu^{2+} + 2\,OH^- \longrightarrow Cu(OH)_2 \tag{43}$$

$$Cu + H_2O_2 \longrightarrow Cu(OH)_2 \tag{44}$$

$$2\,Cu + H_2O_2 \longrightarrow Cu_2O + H_2O\cdot \tag{45}$$

The process is visually represented in figure 45. The fast reduction processes (in red) are dominant as long as the plasma is running and short-lived species are produced in large quantities. When the plasma is turned off and the treatment time is increased, long-lived oxidizing species (in blue) gain a bigger influence resulting in oxidation reactions.

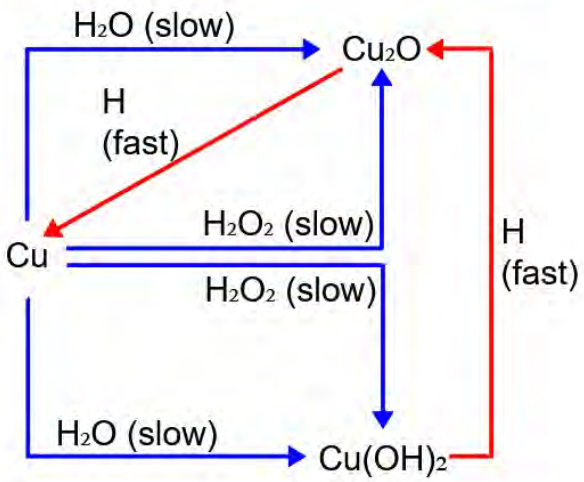

Figure 45: Scheme of dominant reaction processes at the plasma-liquid-solid interface. Oxidation (blue) and reduction (red) mechanisms take place simultaneously.

Since the long-term indirect PAW treatment also yields some CuO, as evident from the XPS and electrochemistry experiments, a pathway for the production of cupric oxide is also considered. At elevated temperatures, the $Cu(OH)_2$ decomposes to CuO and water, following:

$$Cu(OH)_2 \longrightarrow CuO + H_2O \tag{46}$$

As the PAW has room temperature only a small amount of CuO may be formed by this reaction. Another possible reaction to form the small amount of cupric oxide is:

$$2\,Cu(OH)_2 + O_2 \longrightarrow 2\,CuO + H_2O + O_2 \tag{47}$$

This is a double replacement reaction, where the two reactants exchange ions. The oxygen needed for this is formed through the plasma operation and is solvated in the liquid. Either reaction pathway may lead to the formation of the small amount of CuO that can be seen in the CV and XPS measurements.
Since the treatment with pure water or a hydrogen peroxide solution does not yield the same crystal structure as the PAW treatment, the plasma must lead to unique properties in the liquid making it more complex than diluted H_2O_2. The crystal formation mechanism must be a combination of the two processes. A visual representation is depicted in figure 46.

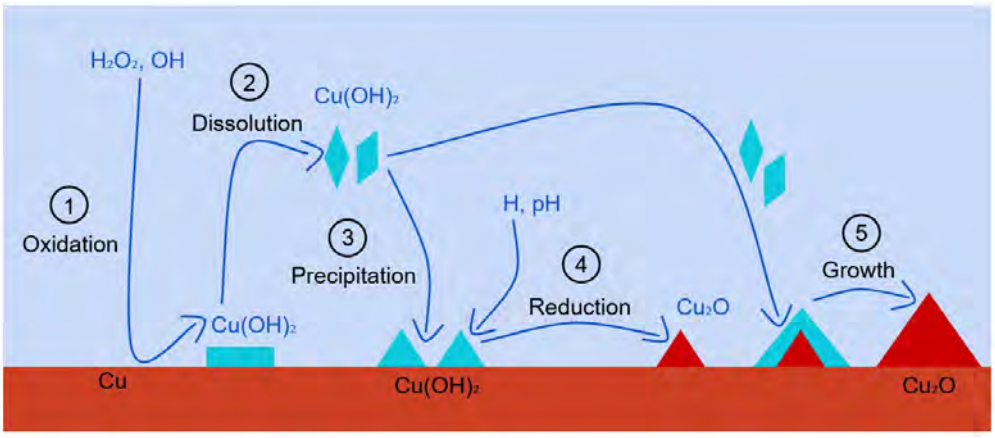

Figure 46: Scheme of a possible growth mechanism of the copper oxide nanocrystals from plasma activated water. A cyclical process consisting of oxidation, dissolution, precipitation reduction and agglomeration lead to particle growth.

A five step process is presented: First, copper is oxidized by oxidizing species of the plasma activated liquid, most likely hydrogen peroxide, though OH may play a minor role. Second, copper hydroxide dissolves in the liquid. Then, the $Cu(OH)_2$ precipitates back onto the copper surface in certain seed regions. These may be impurities or irregularities on the sample. In the next step, the $Cu(OH)_2$ is reduced to Cu_2O. Two possible pathways for this process exist. On one hand, a reducing agent such as H reacts with copper hydroxide. On the other hand, a decomposition reaction may take place. It has been found, that the pH of the plasma activated water does not increase even after long treatment times and the $Cu(OH)_2$ is not stable under these conditions [99]. Therefore, the copper hydroxide may also simply decompose following:

$$2\,Cu(OH)_2 \longrightarrow Cu_2O + H_2O$$

The Cu_2O seeds are now suitable attachment sites for the solvated copper hydroxide and the crystal grows as the $Cu(OH)_2$ attaches and reduces repeatedly. The process ends, when the liquid has been completely evaporated.

5 Summary and Conclusion

In this work, the influence of pulsed-in-liquid plasmas on copper films is explored. The in-liquid plasma is regarded as a possible tool for re-oxidation of copper oxide catalysts, that can be used in the catalysis of the CO_2 reduction reaction.
A distinction is made between a plasma operated with pulse lengths in the microsecond and in the nanosecond range. The ignition mechanisms on these two timescales are different and lead to different chemical properties of the treated liquid, which in turn impacts the copper. In addition, the effect of direct in-liquid plasma treatment and treatment using plasma activated water were investigated separately. The plasma activated liquid contains many reactive species that possess varying lifetimes. By comparing the effect of the plasma to the effect of the liquid, the influence of the short-lived and long-lived species can be separated.

First, the microsecond and the nanosecond plasma are characterized. The microsecond plasma pulse has a rise time of 0.5 µs and a length of 200 µs, the nanosecond pulse has a rise time of 2-3 ns and a length of 12 ns. For both cases, the energies dissipated by the plasma increase with the applied voltage. The dissipated energies of the nanosecond plasma lie in the range of 1-4 mJ while the energy of the microsecond plasma is higher, between 7-25 mJ, depending on the operational settings. This leads to another significant difference between the two plasmas, namely water evaporation and bubble formation, especially over long treatment times. The microsecond plasma causes more Joule heating of the liquid surrounding the electrode, which leads to an accumulation of bubbles at the ignition site. This elicits the transition of the plasma mode from a streamer discharge to a spark-like discharge. When the spark ignites, the dissipated energy abruptly increases to around 100 mJ. Overall, the global temperature of the liquid abruptly increases as well. On the contrary, the nanosecond plasma does not cause significant heating of the liquid and bubble formation, therefore, a streamer-to-spark transition is not observed.

Plasma activated liquids treated with microsecond and nanosecond plasmas are characterized. The temperature, conductivity, pH and hydrogen peroxide concentration are investigated. The global temperature of the liquid increases more steeply over time when the microsecond plasma is used. The conductivity of the liquid also increases more

for the microsecond plasma treatment for the same number of plasma pulses compared to the nanosecond plasma treatment. This can be attributed to the longer pulse lengths and higher dissipated energies. The increase in conductivity indicates an accumulation of positive ions in the liquid. The pH of the treated liquid is not modified by the plasma treatment, indicating that there is no increase in concentration of H^+ ions. As they are a very reactive, short-lived species, it is likely, that they have already decomposed when the plasma is turned off and the measurements can be taken.
The most long lived reactive species present in plasma activated water is hydrogen peroxide. The concentration of H_2O_2 increases with time and plasma frequency, while the concentration that can be reached when the microsecond plasma is used is higher than in the nanosecond case. The concentration increases linearly with frequency for the nanosecond case, while it reaches a plateau for the microsecond case. When the microsecond plasma transitions into a spark, much of the H_2O_2 is destroyed as it is temperature sensitive and the concentration sharply decreases. The production efficiency can be calculated for both cases, 0.5 g/kWh for the nanosecond plasma and 0.2 g/kWh for the microsecond plasma. The fact that the nanosecond plasma is being more than twice as efficient can be explained by the discrepancy in dissipated energies. In sum, the nanosecond plasma produces hydrogen peroxide more efficiently while the use of the microsecond plasma leads to higher absolute concentrations.

During plasma operation, the electrode material erodes and dissolves into the treated liquid. The electrode is made from tungsten, which is chosen for its high melting temperature. Tungsten acts as a catalyst in the decomposition reaction of hydrogen peroxide and therefore has an influence on the liquid chemistry of the plasma activated liquid. In addition, tungsten particles may deposit onto the copper samples and affect the surface changes induced by PAL. After plasma operation, small protrusions can be found on the surface of the electrode. These microstructures are ignition sites where the electrode material locally heats and is transferred into the liquid. The removal of material is determined to be 2-5 nm/ignition for the nanosecond-pulsed plasma. The erosion rate is constant over treatment times up to 30 minutes and increases with increasing voltage. The tungsten nanoparticles can be found in the liquid. Their sizes are generally between 5-25 nm in diameter and their size decreases with increasing voltage. They consist of a combination of metallic tungsten and tungsten oxide, namely WO_3. A nanoparticle production mechanism can be derived from these findings:

As the electrode is locally and rapidly heated, a bubble is formed at the ignition site. The electrode melts and the tungsten oxide evaporates and is expelled into this bubble as it expands. The pressures within the bubble are in the range of 1 GPa and the tungsten oxide is present in the form of a supersaturated vapour. As the bubble expands, nucleation and then coagulation of tungsten oxide takes place. During bubble expansion, the pressure decreases and coagulation is slowed down and eventually vanishes. At higher voltages, bubble expansion is accelerated, giving the tungsten less time to coagulate, leading to smaller particles.

The interaction between in-liquid plasma and copper is the central topic of this work. Copper films deposited onto silicon or silicon oxide substrates are used as samples to study the influence of the plasma and plasma activated water on copper oxide nanostructures. Tungsten from the erosion of the electrode can not be found on the surfaces. It is assumed, that the copper is oxidized by contact with ambient air and with water before the treatment, creating a surface consisting of metallic copper, Cu_2O, $Cu(OH)_2$ and small amounts of CuO. During the direct plasma treatment, the amount of copper oxide decreases. It is suspected, that this is a combination of a reduction and a corrosion process. The plasma creates many reducing species, that are capable of eliciting a reduction reaction.
The effect of the plasma is also compared to the effect of common electrolysis. The plasma ignites at voltages above 16 kV, well-below this threshold water splitting via electrolysis takes place. Under these conditions, the reactive species are produced in smaller concentrations. During electrolysis, the copper surface is not changed significantly. Only when the applied voltage is increased above the ignition threshold, a change is seen on the copper.
When the copper is treated with the plasma activated liquid, an oxidation is observed. This is attributed to the long-lived oxidizing species such as hydrogen peroxide. The oxide can be found in the form of oxide nanocrystals, as opposed to the copper oxides formed by air, where the surface is evenly structured. The water treated with the microsecond plasma has a slightly stronger oxidizing effect on the copper, which can be attributed to the higher concentrations of H_2O_2 and likely other oxidizing species. The effect also seems to be stronger when the plasma is operated at higher voltages, corresponding with the increase in H_2O_2 concentration. The oxide crystals can be found on the surface clustered together as oxide islands. The PAW-formed crystals are

compared to structures formed by contact with distilled water and a H_2O_2 solution. All three liquids lead to the formation of the oxide crystals, but only under the PAW influence, well-ordered copper oxide crystals form. This can be attributed to the presence of the many other reactive species in the PAW, such as H and OH in addition to the H_2O and H_2O_2. The oxide crystals can often be found in tetrahedral and hexahedral shapes.
Based on these findings, an oxidation mechanism for the in-liquid plasma induced copper oxidation can be constructed. The crystal formation is a five step process that is facilitated by the reducing and oxidizing species formed by the plasma. First, the oxidizing species such as H_2O_2 and OH oxidize the copper and $Cu(OH)_2$ is formed. Second, $Cu(OH)_2$ dissolves into the liquid. Third, it precipitates back onto the copper surface in certain seed regions, most likely at surface defects acting as nucleation sites. Here, $Cu(OH)_2$ is reduced to Cu_2O in the fourth step. Lastly, this copper oxide seed serves as a new seed to which $Cu(OH)_2$ can attach, after which it is reduced again. In this cyclical process, copper oxide structures grow into uniformly structured crystals.

In summary, the in-liquid plasma was used to effectively grow copper oxide nano crystals on copper surfaces. Both the microsecond and the nanosecond pulsed plasma are suitable tools to achieve crystal growth. It was determined, that the H_2O_2 produced by the plasma is a significant oxidizing species in this process, but that other oxidizing and reducing species are also required to form well-structured crystals. The nanosecond plasma exhibits a higher H_2O_2 production efficiency, higher absolute concentrations can be achieved with the microsecond plasma. However, other reactive species are also involved in the crystal formation, as diluted hydrogen peroxide does not have the same effect. In-liquid plasmas, or rather the plasma activated water, are a suitable method for copper oxide crystal formation and possibly for reactivation of copper oxide catalysts.

6 Suitability towards Application

In an industrial electrolysis system, (plasma) electrolysis is usually performed in an alkaline environment [2]. Commonly, a continuous voltage is applied. By introducing an electrolyte into the liquid, the conductivity is increased, increasing the current. This is also the standard operational mode during CO_2 reduction processes. However, the introduction of an electrolyte also increases the chemical complexity of the liquid and introduces a large number of reactive species on top of the numerous species created from water. If the pulsed in-liquid plasma should be introduced into such a system, it needs to reliably ignite in more complex liquids with varying conductivities. Over the course of this project, an effort has been made to study the plasma-liquid-solid system not just in distilled water but also in KOH solution as a reference electrolyte. The results are presented in the following section and should serve as a basis for the development of a combined plasma electrolysis system.

6.1 Electrolyte Influence

At first we regard the effect of the nanosecond pulsed plasma operated in KOH solution. In figure 47 the dissipated energies of the nanosecond in-liquid plasma operated in KOH solutions with different concentrations are shown. With the concentration, the conductivity increases. Above 0.5 mmol/l or a conductivity of 70 µS/cm, the medium becomes too conductive for ignition to occur. Charges are able to traverse the liquid more quickly in this case and breakdown is suppressed. The dissipated energy remains unaffected by the increase in conductivity up to 70 µS/cm. This would indicate, that the amount of produced reactive species and therefore the reactivity of the liquid should be similar to distilled water treated with the plasma. It needs to be considered, that now that potassium is introduced into the system, the reaction chemistry becomes more complex.

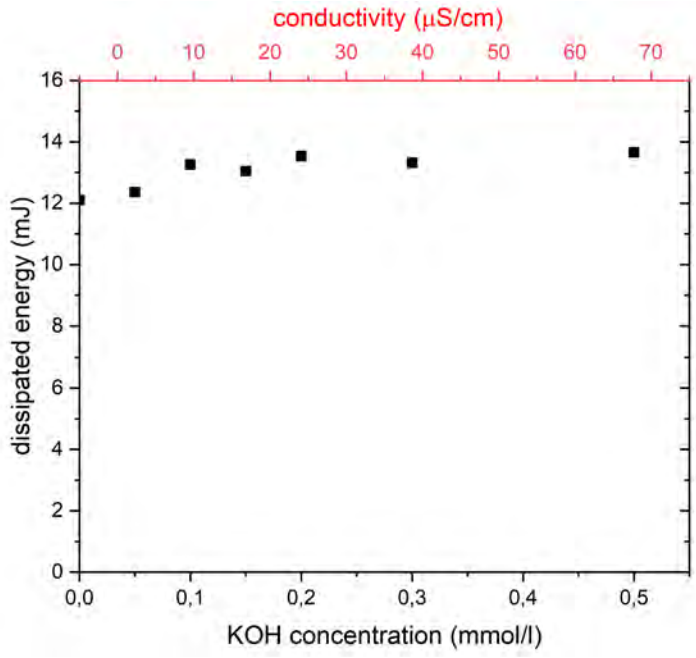

Figure 47: Dissipated energies of the nanosecond plasma ignited in different concentrations and conductivities of KOH solution. The error lies within the dimension of the data points.

Next, the direct treatment of a copper sample in an electrolyte is regarded. In figure 48 in-situ FTIR measurements of a copper sample treated with the nanosecond in-liquid plasma operated in 0.05 mmol/l KOH are shown. This is the highest concentration in which the nanosecond plasma can be operated. The measurement is analogous to the measurement performed in distilled water in figure 32, both samples were treated with a maximum of 1500 pulses at +20 kV. The change in signal in the Cu_2O range is about 0.25% which is similar to the influence of the plasma in water at the same number of pulses. This could be expected from the energy measurements. The reactivity of the plasma activated distilled water and the KOH solution is so similar, that the direct influence on the copper is comparable.

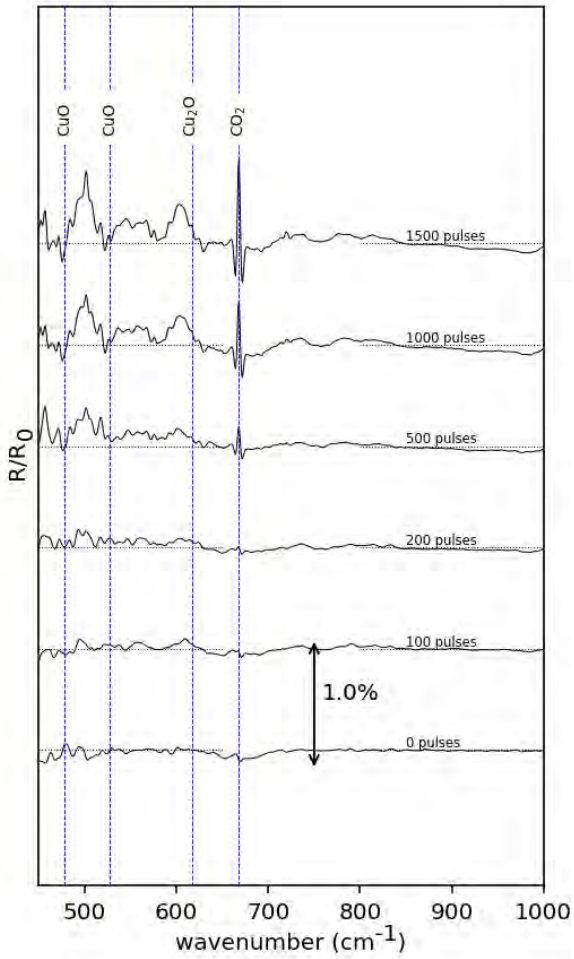

Figure 48: IR spectra of for the in-situ treatment of a 10 nm copper film on a SiO_2 substrate treated with the ns plasma at 20 kV and 10 Hz in 0.5 mmol/l KOH solution, number of pulses as indicated, adapted from [101].

For an application of the in-liquid plasma in an electrolysis system this is beneficial, since the plasma effect needs to be predictable and reproducible. If the plasma treatment yields a similar effect for many conductivities it is suitable for a wider range of applications.

In figure 49 two voltammograms of the same copper sample are shown. The sample was treated with plasma-activated distilled water and the first measurement in figure 49 (in blue) was performed. The main peak B_1 is located at 0.75 V vs. Hg/HgO and the signal from the reduction of Cu^{2+} and a small crystalline Cu_2O peak can be seen. The sample is completely reduced during the measurement, as it ends at -1.2 E_{we}. The sample is then left in the filled CV cell while the OCV measurement is performed which is set to take 35 minutes. Then, the second voltammogram (in red) is recorded. Again, the main peak B_2 is located again at -0.75 V vs. Hg/HgO, but is smaller in comparison. However, no Cu^{2+} reduction signal is visible. This suggests, that the oxide is not restored in an aqueous solution and that the plasma activation is in fact a unique effect.

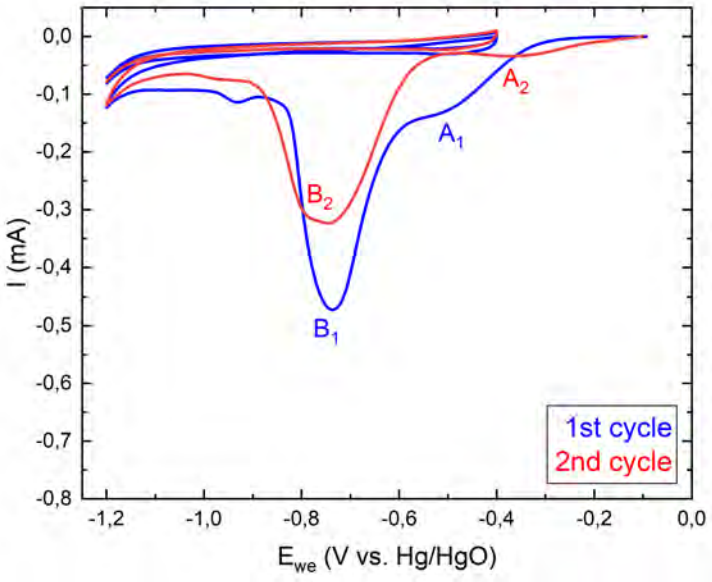

Figure 49: Voltammograms of the first and second cycle of a copper sample treated with nanosecond PAW. The plasma was operated at 20 kV and 10 Hz for one hour. The first cycle (blue) was performed immediately after PAW treatment, the sample then rested in the electrolyte (0.1 M K_2SO_4 & 0.01 M KOH) for 30 minutes before the second cycle was recorded.

To regrow copper oxide crystals, plasma treatment would be necessary in between the first and the second cycle. In a combined plasma electrolysis system, the plasma would need to be ignited in the electrolyte for a certain amount of time, then a period of rest

would follow to give the oxidizing plasma species time to oxidize the copper surface. Here, a challenge presents itself: The cyclic voltammetry is performed at much higher KOH concentrations and conductivities than the 0.5 mmol/l or 70 µS/cm that is the limit for the nanosecond plasma ignition. But since the microsecond plasma ignites in gas bubbles and not directly in the liquid, its ignition limit should be significantly higher. This would make the microsecond plasma more suitable in a combined plasma electrolysis system. In figure 50, the dissipated energy and power of the microsecond pulsed plasma at varying KOH concentrations is shown.

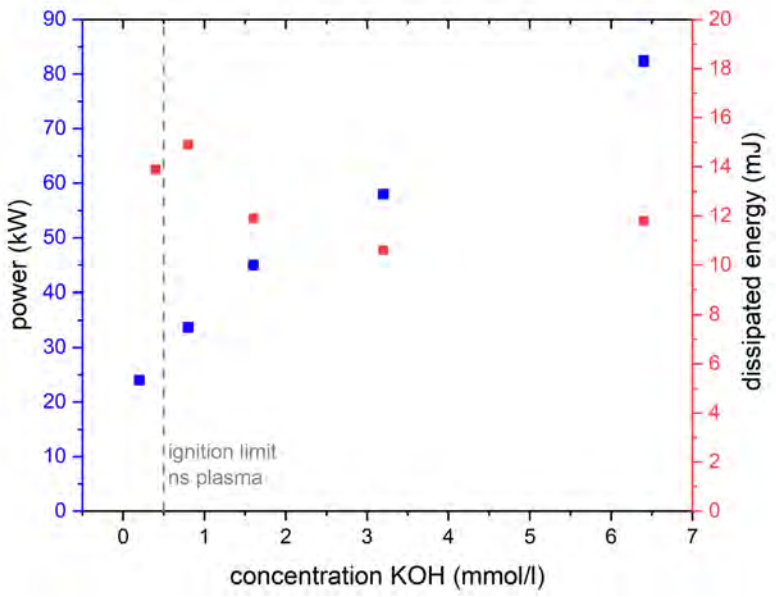

Figure 50: Dissipated energy and power of the microsecond plasma operated in different concentrations of KOH solution. The plasma was operated at 20 kV and 10 Hz. Measurement performed by Sven Weller.

It can be seen, that the microsecond plasma ignites at higher KOH concentrations. The dissipated energy remains between 10 and 14 mJ. The power increases with increasing concentration from 24 to 80 kW. This can be explained by the increasing conductivity of the medium leading to a higher current. At higher powers, larger amounts of electrons are delivered into the liquid by the plasma, which increases the reaction chemistry [102]. This may lead to the expectation, that the effect of the microsecond PAW on the copper may be larger at higher KOH concentrations.

To verify this, cyclic voltammetry is applied again. In figure 51 three voltammograms of three copper samples treated with PAL are presented. The microsecond plasma was ignited in distilled water and KOH solutions with a concentration of 0.05 mmol/l and 3.2 mmol/l. The plasma was operated at +20 kV and 10 Hz for one hour. In all three curves, the main peak is located at around 0.85 V vs. Hg/HgO. No clear trend in peak height or position can be seen. Despite the slight change in plasma power, the effect on the copper is still similar between the distilled water and the treated electrolyte.

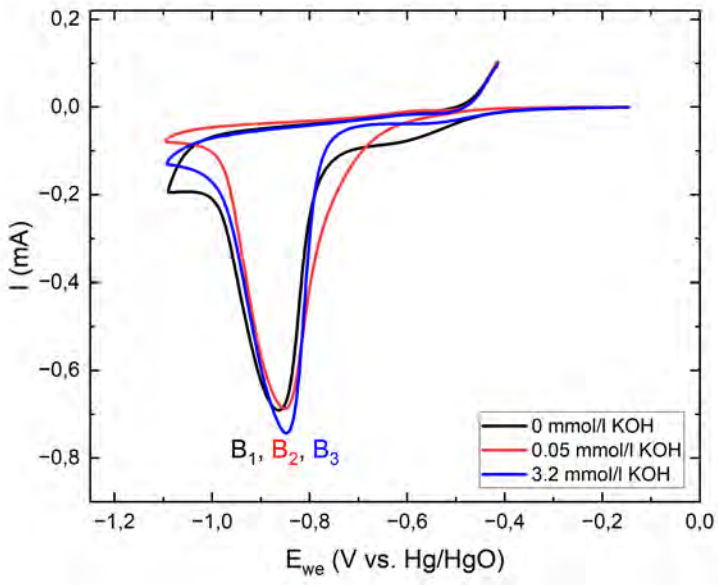

Figure 51: Voltammograms of three 50 nm copper samples treated with plasma activated distilled water (black curve) plasma activated 0.05 mmol/l KOH solution and plasma activated 3.2 mmol/l KOH solution.

Just as in the experiments with distilled water, the temperature of the liquid increases over time. The heat production of the microsecond plasma can be a disadvantage for the process, since KOH has a higher boiling point than water. The water molecules will evaporate more easily and the KOH concentration in the liquid will increase over time [2]. The KOH concentrations indicated in figure 51 represent the concentrations before plasma treatment, they may have been higher during the treatment of the copper.
To examine the surface morphology of the copper, SEM imaging is applied again. In figure 52, SEM images of two different copper samples are shown. Both were treated

with 0.05 mmol/l KOH solution, in the top image the solution was drop-cast as prepared and in the bottom image the solution was treated with the nanosecond pulsed plasma at 20 kV and 10 Hz for one hour, then dropcast onto the copper.

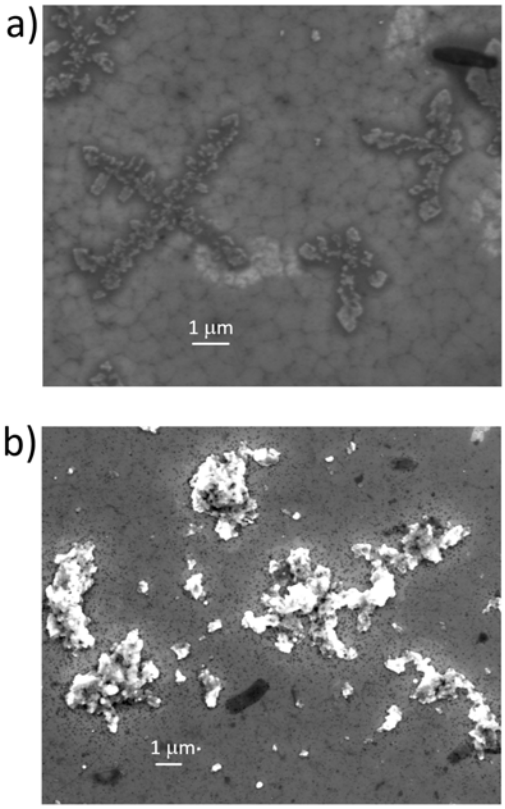

Figure 52: SEM images of two 100 nm copper samples treated with 0.05 mmol/l KOH solution that has been applied directly to the sample a) and has been plasma treated before application b). The plasma was operated at 20 kV, 10 Hz for one hour. Adapted from [89].

A clear difference can be seen between the two surfaces. In the untreated case, the oxides on the surface are present in dendritic structures ranging in size between 5-25 µm. In the plasma treated case, the oxide structures are much smaller between 1-10 µm and more unstructured. Though no well-defined crystals can be found, the plasma treatment still seems to change the properties of the solution. Further investigations are needed to determine whether the in-liquid plasma can be used to create copper oxide nanocrystals by treating an electrolyte under certain experimental conditions.

6.2 Outlook

As copper oxide crystals are used as catalysts, in the future it will be important to further examine the plasma grown crystals from this perspective. In this work, evidence was found that the applied voltage has an effect on the surface structure. Tailoring the number, size and shape of the copper oxide crystals by varying plasma parameters such as voltage, frequency and treatment time of the liquid need to be explored further. It is also known, that the electrode material chosen for this work has an impact on the concentration of H_2O_2 in the PAL as tungsten can catalyse its decomposition and in the future it may be beneficial to investigate other electrode materials to maximize the H_2O_2 production. Additionally, it is essential to evaluate the catalytic performance of the copper oxide crystals during CO_2 conversion.
Based on the findings presented in this thesis, a combined plasma electrolysis system can be developed. The microsecond plasma is more suited for this than the nanosecond plasma due to the higher ignition limit in regards to the solution conductivity. For this, two plasma electrodes, a driven and a grounded one, may be introduced into the electrolysis cell and a plasma may be ignited intermittently between CV cycles. In the voltammogram, restructuring on the surface can be detected. This is illustrated in figure 53. During the CV phase, the crystals are detected and reduced. Then the plasma is applied, eliciting re-oxidation. After a certain amount of time, another voltammogram can be recorded. In this experimental setup, it will be possible to better determine the timescale on which the copper oxide crystals form. In this work, the crystals have been found on the samples after multiple hours of PAW treatment, limited by the time it took for the liquid to fully evaporate. Their size and number may not just depend on the treatment time of the liquid but also on the dwell time of the copper in the PAL. This can be explored using the plasma electrolysis system.

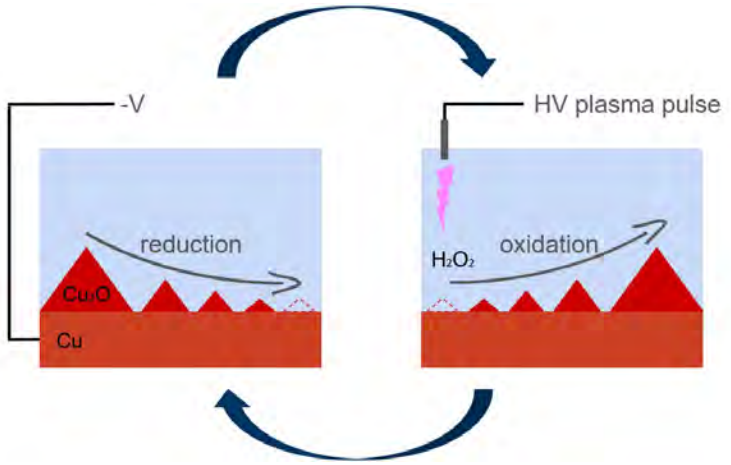

Figure 53: Illustration of the cyclical oxidation and reduction process of copper in a potential combined plasma electrolysis system.

A combined plasma electrolysis system may need to include external cooling to prevent the evaporation of the liquid. This will prevent the change in electrolyte concentration and may suppress bubble formation. Especially if the microsecond plasma is used, the transition of the streamer-like discharge into a spark should be avoided. In this work it is shown, that as the spark ignites, the temperature of the liquid rapidly increases, destroying hydrogen peroxide. This may hinder the formation of copper oxide crystals. For this reason, an effort should be made to determine the conditions under which the spark ignites. The transition is likely dependent on many factors such as voltage, frequency, treatment time, liquid temperature and electrode distance.
In conclusion, the pulsed in-liquid plasmas, especially with pulse lengths in the microsecond range, show potential applicability as catalysts in the field of electrochemistry.

Bibliography

[1] Alexander Navarrete et al. “Harvesting Renewable Energy for Carbon Dioxide Catalysis.” In: *Energy Technology* 5.6 (June 2017), pp. 796–811. ISSN: 2194-4288, 2194-4296. DOI: 10.1002/ente.201600609.

[2] Jia Yue Zhao et al. “A focus on the electrolyte: Realizing CO2 electroreduction from aqueous solution to pure water.” In: *Chem Catalysis* 3.1 (Jan. 2023), p. 100471. ISSN: 26671093. DOI: 10.1016/j.checat.2022.11.010.

[3] Rulle Reske et al. “Particle Size Effects in the Catalytic Electroreduction of CO $_2$ on Cu Nanoparticles.” In: *Journal of the American Chemical Society* 136.19 (May 14, 2014), pp. 6978–6986. ISSN: 0002-7863, 1520-5126. DOI: 10.1021/ja500328k.

[4] Abebe Reda Woldu et al. “Electrochemical CO2 reduction (CO2RR) to multi-carbon products over copper-based catalysts.” In: *Coordination Chemistry Reviews* 454 (Mar. 2022), p. 214340. ISSN: 00108545. DOI: 10.1016/j.ccr.2021.214340.

[5] Paramita Saha, Sk Amanullah, and Abhishek Dey. “Selectivity in Electrochemical CO_2 Reduction.” In: *Accounts of Chemical Research* 55.2 (Jan. 18, 2022), pp. 134–144. ISSN: 0001-4842, 1520-4898. DOI: 10.1021/acs.accounts.1c00678.

[6] Haoyuan Wang et al. “CO2 electrolysis toward acetate: A review.” In: *Current Opinion in Electrochemistry* 39 (June 2023), p. 101253. ISSN: 24519103. DOI: 10.1016/j.coelec.2023.101253.

[7] Dunfeng Gao et al. “Plasma-Activated Copper Nanocube Catalysts for Efficient Carbon Dioxide Electroreduction to Hydrocarbons and Alcohols.” In: *ACS Nano* 11.5 (May 23, 2017). Publisher: American Chemical Society, pp. 4825–4831. ISSN: 1936-0851. DOI: 10.1021/acsnano.7b01257.

[8] Ludovic Zaza, Kevin Rossi, and Raffaella Buonsanti. “Well-Defined Copper-Based Nanocatalysts for Selective Electrochemical Reduction of CO2 to C2 Products.” In: *ACS Energy Letters* 7.4 (Apr. 8, 2022), pp. 1284–1291. DOI: 10.1021/acsenergylett.2c00035.

[9] Rosa M. Arán-Ais et al. “Imaging Electrochemically Synthesized Cu2O Cubes and Their Morphological Evolution under Conditions Relevant to CO2 Electroreduction.” In: *Nature Communications* 11.1 (July 13, 2020), p. 3489. ISSN: 2041-1723. DOI: 10.1038/s41467-020-17220-6.

[10] Rolf Beerthuis et al. “Particle size effects in copper-catalyzed hydrogenation of ethyl acetate.” In: *Journal of Catalysis* 388 (Aug. 2020), pp. 30–37. ISSN: 00219517. DOI: 10.1016/j.jcat.2020.05.006.

[11] Philipp Grosse et al. “Dynamic Changes in the Structure, Chemical State and Catalytic Selectivity of Cu Nanocubes during CO2 Electroreduction: Size and Support Effects.” In: *Angewandte Chemie* 130.21 (2018), pp. 6300–6305. ISSN: 1521-3757. DOI: 10.1002/ange.201802083.

[12] Qingye Ren et al. “Structural Evolution of Cu2O Nanocube Electrocatalysts for the CO2 Reduction Reaction.” In: *Nano Energy* 106 (Feb. 2023), p. 108080. ISSN: 22112855. DOI: 10.1016/j.nanoen.2022.108080.

[13] Aram Yoon et al. “Revealing catalyst restructuring and composition during nitrate electroreduction through correlated operando microscopy and spectroscopy.” In: *Nature Materials* 24.5 (May 2025), pp. 762–769. ISSN: 1476-1122, 1476-4660. DOI: 10.1038/s41563-024-02084-8.

[14] Chobei Yamabe et al. “Water Treatment Using Discharge on the Surface of a Bubble in Water.” In: *Plasma Processes and Polymers* 2.3 (2005), pp. 246–251. ISSN: 1612-8869. DOI: 10.1002/ppap.200400077.

[15] Bo Jiang et al. “Review on Electrical Discharge Plasma Technology for Wastewater Remediation.” In: *Chemical Engineering Journal* 236 (Jan. 2014), pp. 348–368. ISSN: 13858947. DOI: 10.1016/j.cej.2013.09.090.

[16] John Foster et al. “Perspectives on the Interaction of Plasmas With Liquid Water for Water Purification.” In: *IEEE Transactions on Plasma Science* 40.5 (May 2012), pp. 1311–1323. ISSN: 0093-3813, 1939-9375. DOI: 10.1109/TPS.2011.2180028.

[17] Francesco Tampieri, Yury Gorbanev, and Eloisa Sardella. “Plasma-treated Liquids in Medicine: Let’s Get Chemical.” In: *Plasma Processes and Polymers* 20.9 (Sept. 2023), e2300077. ISSN: 1612-8850, 1612-8869. DOI: 10.1002/ppap.202300077.

[18] Muhammad Arif Malik, Abdul Ghaffar, and Salman Akbar Malik. "Water Purification by Electrical Discharges." In: *Plasma Sources Science and Technology* 10.1 (Feb. 1, 2001), pp. 82–91. ISSN: 0963-0252, 1361-6595. DOI: 10.1088/0963-0252/10/1/311.

[19] S. Horikoshi and N. Serpone. "In-Liquid Plasma: A Novel Tool in the Fabrication of Nanomaterials and in the Treatment of Wastewaters." In: *RSC Adv.* 7.75 (2017), pp. 47196–47218. ISSN: 2046-2069. DOI: 10.1039/C7RA09600C.

[20] Peter J. Bruggeman and Christophe Leys. "Non-Thermal Plasmas in and in Contact with Liquids." In: *Journal of Physics D: Applied Physics* 42.5 (2009), p. 053001. ISSN: 0022-3727. DOI: 10.1088/0022-3727/42/5/053001.

[21] P J Bruggeman et al. "Plasma–Liquid Interactions: A Review and Roadmap." In: *Plasma Sources Science and Technology* 25.5 (Sept. 30, 2016), p. 053002. ISSN: 1361-6595. DOI: 10.1088/0963-0252/25/5/053002.

[22] Gao Jinzhang et al. "Analysis of Energetic Species Caused by Contact Glow Discharge Electrolysis in Aqueous Solution." In: *Plasma Science and Technology* 10.1 (Feb. 2008), pp. 30–38. ISSN: 1009-0630. DOI: 10.1088/1009-0630/10/1/07.

[23] K Grosse et al. "Nanosecond Plasmas in Water: Ignition, Cavitation and Plasma Parameters." In: *Plasma Sources Science and Technology* 28.8 (Aug. 8, 2019), p. 085003. ISSN: 1361-6595. DOI: 10.1088/1361-6595/ab26fc.

[24] S Medodovic and B R Locke. "Primary Chemical Reactions in Pulsed Electrical Discharge Channels in Water." In: *Journal of Physics D: Applied Physics* 42.4 (Feb. 21, 2009), pp. 049801–049801. ISSN: 0022-3727, 1361-6463. DOI: 10.1088/0022-3727/42/4/049801.

[25] Bruce R Locke and Kai-Yuan Shih. "Review of the Methods to Form Hydrogen Peroxide in Electrical Discharge Plasma with Liquid Water." In: *Plasma Sources Science and Technology* 20.3 (June 1, 2011), p. 034006. ISSN: 0963-0252, 1361-6595. DOI: 10.1088/0963-0252/20/3/034006.

[26] D. DeNardis et al. "Studying the Effect of Temperature on the Copper Oxidation Process Using Hydrogen Peroxide for Use in Multi-Step Chemical Mechanical Planarization Models." In: *Thin Solid Films* 518.14 (May 2010), pp. 3903–3909. ISSN: 00406090. DOI: 10.1016/j.tsf.2009.12.089.

[27] Robert J. Wandell et al. *The Effects of Pulse Frequency on Chemical Species Formation in a Nanosecond Pulsed Plasma Gas-Liquid Film Reactor*. 2020. DOI: 10.34343/ijpest.2020.14.e01008. The Institute of Electrostatics Japan: 01. URL: https://doi.org/10.34343/ijpest.2020.14.e01008 (visited on 03/19/2024). Pre-published.

[28] A. V. Nominé et al. "Synthesis of Nanomaterials by Electrode Erosion Using Discharges in Liquids." In: *Journal of Applied Physics* 130.15 (Oct. 21, 2021), p. 151101. ISSN: 0021-8979, 1089-7550. DOI: 10.1063/5.0040587.

[29] Steffen Schüttler, Niklas Eichstaedt, and Judith Golda. "Tuning Plasma Chemistry by Various Excitation Mechanisms for the H 2 O 2 Production of Atmospheric Pressure Plasma Jets." In: *Journal of Physics D: Applied Physics* 58.2 (Jan. 13, 2025), p. 025203. ISSN: 0022-3727, 1361-6463. DOI: 10.1088/1361-6463/ad816a.

[30] Kai-Yuan Shih and Bruce R. Locke. "Chemical and Physical Characteristics of Pulsed Electrical Discharge Within Gas Bubbles in Aqueous Solutions." In: *Plasma Chemistry and Plasma Processing* 30.1 (Feb. 2010), pp. 1–20. ISSN: 0272-4324, 1572-8986. DOI: 10.1007/s11090-009-9207-x.

[31] Bruce R. Locke and Selma Mededovic Thagard. "Analysis and Review of Chemical Reactions and Transport Processes in Pulsed Electrical Discharge Plasma Formed Directly in Liquid Water." In: *Plasma Chemistry and Plasma Processing* 32.5 (Oct. 2012), pp. 875–917. ISSN: 0272-4324, 1572-8986. DOI: 10.1007/s11090-012-9403-y.

[32] Marien Simeni Simeni, Yuchen Luo, and Peter J Bruggeman. "On the origins of the continuum radiation of an underwater nanosecond pulsed discharge: an absolute-intensity optical emission spectroscopy study." In: *Plasma Sources Science and Technology* 34.2 (Feb. 1, 2025), p. 025003. ISSN: 0963-0252, 1361-6595. DOI: 10.1088/1361-6595/adac0b.

[33] Pavel Šunka. "Pulse Electrical Discharges in Water and Their Applications." In: *Physics of Plasmas* 8.5 (May 2001), pp. 2587–2594. ISSN: 1070-664X, 1089-7674. DOI: 10.1063/1.1356742.

[34] Yohan Seepersad, Alexander Fridman, and Danil Dobrynin. "Anode Initiated Impulse Breakdown in Water: The Dependence on Pulse Rise Time for Nanosecond and Sub-Nanosecond Pulses and Initiation Mechanism Based on Electrostriction." In: *Journal of Physics D: Applied Physics* 48.42 (Oct. 28, 2015), p. 424012. ISSN: 0022-3727, 1361-6463. DOI: 10.1088/0022-3727/48/42/424012.

[35] M. N. Shneider and M. Pekker. "Dielectric Fluid in Inhomogeneous Pulsed Electric Field." In: *Physical Review E* 87.4 (Apr. 9, 2013). ISSN: 1539-3755, 1550-2376. DOI: 10.1103/PhysRevE.87.043004.

[36] Robert Gomer. "Field Emission, Field Ionization, and Field Desorption." In: *Surface Science* 299–300 (Jan. 1994), pp. 129–152. ISSN: 00396028. DOI: 10.1016/0039-6028(94)90651-3.

[37] K. Grosse, M. Falke, and A. von Keudell. "Ignition and Propagation of Nanosecond Pulsed Plasmas in Distilled Water—Negative vs Positive Polarity Applied to a Pin Electrode." In: *Journal of Applied Physics* 129.21 (June 7, 2021), p. 213302. ISSN: 0021-8979, 1089-7550. DOI: 10.1063/5.0045697.

[38] P. Lukeš et al. "Erosion of Needle Electrodes in Pulsed Corona Discharge in Water." In: *Czechoslovak Journal of Physics* 56.S2 (Oct. 2006), B916–B924. ISSN: 0011-4626, 1572-9486. DOI: 10.1007/s10582-006-0304-2.

[39] B. R. Locke et al. "Electrohydraulic Discharge and Nonthermal Plasma for Water Treatment." In: *Industrial & Engineering Chemistry Research* 45.3 (Feb. 2006), pp. 882–905. ISSN: 0888-5885, 1520-5045. DOI: 10.1021/ie050981u.

[40] Thiery Belmonte and Peter Bruggeman. "Optical Diagnostics of Discharges in and in Contact With Liquids." In: *Plasma Processes and Polymers* (Nov. 24, 2024), e2400213. ISSN: 1612-8850, 1612-8869. DOI: 10.1002/ppap.202400213.

[41] Nicholas L Sponsel, Sophia Gershman, and Katharina Stapelmann. "Electrical Breakdown Dynamics in an Argon Bubble Submerged in Conductive Liquid for Nanosecond Pulsed Discharges." In: *Journal of Physics D: Applied Physics* 56.50 (Dec. 14, 2023), p. 505202. ISSN: 0022-3727, 1361-6463. DOI: 10.1088/1361-6463/acfb1b.

[42] Emmanuel Zoulias et al. "A review on water electrolysis." In: (2004).

[43] Allen J. Bard, Larry R. Faulkner, and Henry S. White. *Electrochemical methods fundamentals and applications*. eng. Third edition. Hoboken, NJ: Wiley, 2022. ISBN: 9781119334064.

[44] Nashmil Karimian et al. "The Principles of Bipolar Electrochemistry and Its Electroanalysis Applications." In: *Current Opinion in Electrochemistry*. Environmental Electrochemistry • Surface Electrochemistry 17 (Oct. 1, 2019), pp. 30–37. ISSN: 2451-9103. DOI: 10.1016/j.coelec.2019.04.015.

[45] Stephen E. Fosdick et al. "Bipolar Electrochemistry." In: *Angewandte Chemie International Edition* 52.40 (2013), pp. 10438–10456. ISSN: 1521-3773. DOI: 10.1002/anie.201300947.

[46] Jie Ren et al. "Recent Progress in the Application of Glow-Discharge Electrolysis Plasma." In: *Open Chemistry* 12.12 (Dec. 1, 2014), pp. 1213–1221. ISSN: 2391-5420. DOI: 10.2478/s11532-014-0575-6.

[47] Laura Chauvet et al. "Chemistry in Nanosecond Plasmas in Water." In: *Plasma Processes and Polymers* 17.6 (June 2020), p. 1900192. ISSN: 1612-8850, 1612-8869. DOI: 10.1002/ppap.201900192.

[48] W G Graham and K R Stalder. "Plasmas in Liquids and Some of Their Applications in Nanoscience." In: *Journal of Physics D: Applied Physics* 44.17 (May 4, 2011), p. 174037. ISSN: 0022-3727, 1361-6463. DOI: 10.1088/0022-3727/44/17/174037.

[49] M. Sato, T. Ohgiyama, and J.S. Clements. "Formation of Chemical Species and Their Effects on Microorganisms Using a Pulsed High-Voltage Discharge in Water." In: *IEEE Transactions on Industry Applications* 32.1 (Jan. 1996), pp. 106–112. ISSN: 1939-9367. DOI: 10.1109/28.485820.

[50] H Christensen, K Sehested, and T Logager. "Temperature Dependence of the Rate Constant for Reactions of Hydrated Electons with H, OH and H202." In: 43.6 (1993), p. 527. DOI: 10.1016/0969-806X(94)90163-5.

[51] J. Troe. "The Thermal Dissociation/Recombination Reaction of Hydrogen Peroxide H 2 O 2 (+ M) 2 OH (+ M) III." In: *Combustion and Flame* 158.4 (Apr. 2011), pp. 594–601. ISSN: 00102180. DOI: 10.1016/j.combustflame.2010.08.013.

[52] Eric Croiset, Steven F. Rice, and Russell G. Hanush. “Hydrogen peroxide decomposition in supercritical water.” In: *AIChE Journal* 43.9 (1997). _eprint: https://aiche.onlinelibrary.wiley.com/doi/pdf/10.1002/aic.690430919, pp. 2343–2352. ISSN: 1547-5905. DOI: 10.1002/aic.690430919.

[53] Igor Štefanić and Jay A. LaVerne. “Temperature Dependence of the Hydrogen Peroxide Production in the -Radiolysis of Water.” In: *The Journal of Physical Chemistry A* 106.2 (Jan. 1, 2002), pp. 447–452. ISSN: 1089-5639. DOI: 10.1021/jp0131830.

[54] Š. Potocký, N. Saito, and O. Takai. “Needle Electrode Erosion in Water Plasma Discharge.” In: *Thin Solid Films* 518.3 (Dec. 2009), pp. 918–923. ISSN: 00406090. DOI: 10.1016/j.tsf.2009.07.172.

[55] Tadahiko Mizuno et al. “Production of Heat during Plasma Electrolysis in Liquid.” In: *Japanese Journal of Applied Physics* 39 (Part 1, No. 10 Oct. 15, 2000), pp. 6055–6061. ISSN: 0021-4922, 1347-4065. DOI: 10.1143/JJAP.39.6055.

[56] K Grosse, V Schulz-von der Gathen, and A von Keudell. “Nanosecond Pulsed Discharges in Distilled Water: I. Continuum Radiation and Plasma Ignition.” In: *Plasma Sources Science and Technology* 29.9 (Sept. 16, 2020), p. 095008. ISSN: 1361-6595. DOI: 10.1088/1361-6595/aba487.

[57] Frank Holzer and Bruce R. Locke. “Influence of High Voltage Needle Electrode Material on Hydrogen Peroxide Formation and Electrode Erosion in a Hybrid Gas–Liquid Series Electrical Discharge Reactor.” In: *Plasma Chemistry and Plasma Processing* 28.1 (Feb. 2008), pp. 1–13. ISSN: 0272-4324, 1572-8986. DOI: 10.1007/s11090-007-9107-x.

[58] Osamu Takai. “Solution Plasma Processing (SPP).” In: *Pure and Applied Chemistry* 80.9 (Jan. 1, 2008), pp. 2003–2011. ISSN: 1365-3075, 0033-4545. DOI: 10.1351/pac200880092003.

[59] T. Abdul Kareem and A. Anu Kaliani. “Glow Discharge Plasma Electrolysis for Nanoparticles Synthesis.” In: *Ionics* 18.3 (Mar. 1, 2012), pp. 315–327. ISSN: 1862-0760. DOI: 10.1007/s11581-011-0639-y.

[60] Geonja Lim et al. “Oxidation Behavior of Tungsten in H[sub 2]O[sub 2]- and Fe(NO[sub 3])[sub 3]-Base Aqueous Slurries.” In: *Journal of The Electrochemical Society* 153.5 (2006), B169. ISSN: 00134651. DOI: 10.1149/1.2181433.

[61] Petr Lukes et al. “The Catalytic Role of Tungsten Electrode Material in the Plasmachemical Activity of a Pulsed Corona Discharge in Water.” In: *Plasma Sources Science and Technology* 20.3 (June 1, 2011), p. 034011. ISSN: 0963-0252, 1361-6595. DOI: 10.1088/0963-0252/20/3/034011.

[62] Guangwen Zhou and Judith C. Yang. “Initial Oxidation Kinetics of Copper (110) Film Investigated by in Situ UHV-TEM.” In: *Surface Science* 531.3 (June 2003), pp. 359–367. ISSN: 00396028. DOI: 10.1016/S0039-6028(03)00539-9.

[63] Guangwen Zhou and Judith C. Yang. “In Situ UHV-TEM Investigation of the Kinetics of Initial Stages of Oxidation on the Roughened Cu(1 1 0) Surface.” In: *Surface Science* 559.2–3 (June 2004), pp. 100–110. ISSN: 00396028. DOI: 10.1016/j.susc.2004.04.046.

[64] Jari Aromaa et al. “The Oxidation of Copper in Air at Temperatures up to 100 °C.” In: *Corrosion and Materials Degradation* 2.4 (4 Dec. 2021), pp. 625–640. ISSN: 2624-5558. DOI: 10.3390/cmd2040033.

[65] P. Zhou and K. Ogle. “The Corrosion of Copper and Copper Alloys.” In: *Encyclopedia of Interfacial Chemistry*. Elsevier, 2018, pp. 478–489. ISBN: 978-0-12-809894-3. DOI: 10.1016/B978-0-12-409547-2.13429-8.

[66] Nawzat S. Saadi, Laylan B. Hassan, and Tansel Karabacak. “Metal oxide nanostructures by a simple hot water treatment.” In: *Scientific Reports* 7.1 (Aug. 2, 2017), p. 7158. ISSN: 2045-2322. DOI: 10.1038/s41598-017-07783-8.

[67] Daoyuan Wang et al. “Cyclic voltammetry and specific capacitance studies of copper oxide nanostructures grown by hot water treatment.” In: *MRS Advances* 9.12 (Nov. 22, 2023), pp. 979–985. ISSN: 2059-8521. DOI: 10.1557/s43580-023-00712-0.

[68] D. DeNardis et al. “Characterization of Copper-Hydrogen Peroxide Film Growth Kinetics.” In: *Thin Solid Films* 513.1–2 (Aug. 2006), pp. 311–318. ISSN: 00406090. DOI: 10.1016/j.tsf.2006.02.010.

[69] Asep Bayu Dani Nandiyanto, Rosi Oktiani, and Risti Ragadhita. “How to Read and Interpret FTIR Spectroscope of Organic Material.” In: *Indonesian Journal of Science and Technology* 4.1 (Mar. 7, 2019), p. 97. ISSN: 2527-8045, 2528-1410. DOI: 10.17509/ijost.v4i1.15806.

[70] Catherine Berthomieu and Rainer Hienerwadel. “Fourier transform infrared (FTIR) spectroscopy.” In: *Photosynthesis Research* 101.2 (Sept. 2009), pp. 157–170. ISSN: 0166-8595, 1573-5079. DOI: 10.1007/s11120-009-9439-x.

[71] Bruker. *Benutzer-Handbuch IFS 28 / IFS 55 Equinox*. Bruker.

[72] Noémie Elgrishi et al. “A Practical Beginner’s Guide to Cyclic Voltammetry.” In: *Journal of Chemical Education* 95.2 (Feb. 13, 2018), pp. 197–206. ISSN: 0021-9584. DOI: 10.1021/acs.jchemed.7b00361.

[73] Alexandros Ch. Lazanas and Mamas I. Prodromidis. “Electrochemical Impedance Spectroscopy A Tutorial.” In: *ACS Measurement Science Au* 3.3 (June 21, 2023), pp. 162–193. ISSN: 2694-250X, 2694-250X. DOI: 10.1021/acsmeasuresciau.2c00070.

[74] H. Gil, A. Echavarría, and F. Echeverría. “Electrochemical Reduction Modeling of Copper Oxides Obtained during in Situ and Ex Situ Conditions in the Presence of Acetic Acid.” In: *Electrochimica Acta* 54.20 (Aug. 2009), pp. 4676–4681. ISSN: 00134686. DOI: 10.1016/j.electacta.2009.03.082.

[75] Fred A. Stevie and Carrie L. Donley. “Introduction to x-ray photoelectron spectroscopy.” In: *Journal of Vacuum Science & Technology A: Vacuum, Surfaces, and Films* 38.6 (Dec. 1, 2020), p. 063204. ISSN: 0734-2101, 1520-8559. DOI: 10.1116/6.0000412.

[76] Manoj B. Gawande et al. “Cu and Cu-Based Nanoparticles: Synthesis and Applications in Catalysis.” In: *Chemical Reviews* 116.6 (Mar. 23, 2016), pp. 3722–3811. ISSN: 0009-2665, 1520-6890. DOI: 10.1021/acs.chemrev.5b00482.

[77] Mark C. Biesinger. “Advanced Analysis of Copper X-ray Photoelectron Spectra.” In: *Surface and Interface Analysis* 49.13 (2017), pp. 1325–1334. ISSN: 1096-9918. DOI: 10.1002/sia.6239.

[78] Yohan Seepersad et al. “Investigation of Positive and Negative Modes of Nanosecond Pulsed Discharge in Water and Electrostriction Model of Initiation.” In: *Journal of Physics D: Applied Physics* 46.35 (2013), p. 355201. ISSN: 0022-3727. DOI: 10.1088/0022-3727/46/35/355201.

[79] Tamilselvan Velusamy et al. "Ultra-Small CuO Nanoparticles with Tailored Energy-Band Diagram Synthesized by a Hybrid Plasma-Liquid Process." In: *Plasma Processes and Polymers* 14.7 (July 2017), p. 1600224. ISSN: 16128850. DOI: 10.1002/ppap.201600224.

[80] G. Papadimitropoulos et al. "Optical and Structural Properties of Copper Oxide Thin Films Grown by Oxidation of Metal Layers." In: *Thin Solid Films* 515.4 (Dec. 2006), pp. 2428–2432. ISSN: 00406090. DOI: 10.1016/j.tsf.2006.06.002.

[81] M Johan et al. "Annelaing Effects on the Properties of CuO Films Prepared by CVD." In: *Int. J. Electrochem. Sci.* 6 (2011), p. 6094. DOI: 10.1016/S1452-3981(23)19665-9.

[82] Yong Cai Zhang et al. "Facile Synthesis of Submicron Cu2O and CuO Crystallites from a Solid Metallorganic Molecular Precursor." In: *Journal of Crystal Growth* 294.2 (Sept. 2006), pp. 278–282. ISSN: 00220248. DOI: 10.1016/j.jcrysgro.2006.06.038.

[83] Necmi Serin et al. "Annealing Effects on the Properties of Copper Oxide Thin Films Prepared by Chemical Deposition." In: *Semiconductor Science and Technology* 20.5 (May 1, 2005), pp. 398–401. ISSN: 0268-1242, 1361-6641. DOI: 10.1088/0268-1242/20/5/012.

[84] Perumal Naveenkumar et al. "Solvothermal Synthesis of CuS/Cu(OH)2 Nanocomposite Electrode Materials for Supercapacitor Applications." In: *Journal of Materials Science: Materials in Electronics* 29.19 (Oct. 2018), pp. 16853–16863. ISSN: 0957-4522, 1573-482X. DOI: 10.1007/s10854-018-9780-y.

[85] E.R. Lippincott et al. "Infrared Studies on Polymorphs of Silicon Dioxide and Germanium Dioxide." In: *Journal of Research of the National Bureau of Standards* 61.1 (July 1958), p. 61. ISSN: 0091-0635. DOI: 10.6028/jres.061.009.

[86] Marta Klanjšek Gunde. "Vibrational Modes in Amorphous Silicon Dioxide." In: *Physica B: Condensed Matter* 292.3–4 (Nov. 2000), pp. 286–295. ISSN: 09214526. DOI: 10.1016/S0921-4526(00)00475-0.

[87] Kenta Kawashima et al. "Accurate Potentials of Hg/HgO Electrodes: Practical Parameters for Reporting Alkaline Water Electrolysis Overpotentials." In: *ACS Catalysis* 13.3 (Feb. 3, 2023), pp. 1893–1898. ISSN: 2155-5435, 2155-5435. DOI: 10.1021/acscatal.2c05655.

[88] Sengeni Anantharaj et al. “The reference electrode dilemma in energy conversion electrocatalysis: “right *vs.* okay *vs.* wrong”.” In: *Journal of Materials Chemistry A* 11.33 (2023), pp. 17699–17709. ISSN: 2050-7488, 2050-7496. DOI: 10.1039/D3TA03145D.

[89] P Pottkämper et al. “Nanosecond and microsecond-pulsed plasma-in-liquid treated copper oxide surfaces.” In: *Journal of Physics D: Applied Physics* 58.30 (July 28, 2025), p. 305201. ISSN: 0022-3727, 1361-6463. DOI: 10.1088/1361-6463/adebfc.

[90] Jeol Ltd. “JEOL JSM-7200F Operation Manual.” In: (2021).

[91] Neil Unteregge. *Electrochemical Investigation of Microsecond Plasma-in-Liquid Treated Copper Surfaces*. Master Thesis. 2025.

[92] Nils Huber. *Influence of µs-Pulsed Plasma Treated Liquids on Copper-Oxide Catalysts*. Bachelor Thesis. 2025.

[93] O Krettek et al. “Creation of Tungsten and Platinum Nanoparticles from Nanosecond Plasmas in Water.” In: *Journal of Physics D: Applied Physics* 57.48 (Dec. 6, 2024), p. 485201. ISSN: 0022-3727, 1361-6463. DOI: 10.1088/1361-6463/ad7301.

[94] Oliver Krettek. *Investigation of Plasma-Assisted Nanoparticle Production at the Liquid-Solid Interface*. Bachelor Thesis. 2023.

[95] P Pottkämper and A Von Keudell. “Plasma in Liquids Induced Modification of Cu Surfaces.” In: *Journal of Physics D: Applied Physics* 57.34 (Aug. 30, 2024), p. 345201. ISSN: 0022-3727, 1361-6463. DOI: 10.1088/1361-6463/ad4b2d.

[96] Singuru Rajesh and Adhidesh S. Kumawat. “Designing a heavy metal electrochemical sensor for Pb detection in water—A generalized approach for electrochemical sensing using low-cost materials.” In: *The Canadian Journal of Chemical Engineering* 102.12 (Dec. 2024), pp. 4203–4215. ISSN: 0008-4034, 1939-019X. DOI: 10.1002/cjce.25353.

[97] J Ambrose, R G Barradas, and D W Shoesmith. “Investigations of Copper in Aqueous Alkaline Solutions by Cyclic Voltammetry.” In: *Journal of Electroanalytical Chemistry and Interfacial Electrochemistry* (). DOI: 10.1016/S0022-0728(73)80344-4.

[98] David Reyter et al. “Electrochemically Activated Copper Electrodes.” In: *Journal of The Electrochemical Society* 154.8 (2007), K36. ISSN: 00134651. DOI: 10.1149/1.2746805.

[99] Sachin D. Giri and A. Sarkar. “Electrochemical Study of Bulk and Monolayer Copper in Alkaline Solution.” In: *Journal of The Electrochemical Society* 163.3 (2016), H252–H259. ISSN: 0013-4651, 1945-7111. DOI: 10.1149/2.0071605jes.

[100] T.T.M Tran et al. “The Atmospheric Corrosion of Copper by Hydrogen Sulphide in Underground Conditions.” In: *Corrosion Science* 45.12 (Dec. 2003), pp. 2787–2802. ISSN: 0010938X. DOI: 10.1016/S0010-938X(03)00112-4.

[101] Sven Weller. *Investigation of plasma-in-liquid induced copper oxidation*. Bachelor Thesis. 2024.

[102] Peter J. Bruggeman et al. “Plasma-Driven Solution Electrolysis.” In: *Journal of Applied Physics* 129.20 (May 28, 2021), p. 200902. ISSN: 0021-8979. DOI: 10.1063/5.0044261.

Acknowledgements

Finally, I would like to thank the many people who supported me during my time as a doctoral student and in the creation of this work. In particular i would like to mention:

- Prof. Dr. Achim von Keudell, for the opportunity to carry out this dissertation at the Chair of Experimental Physics II and for the excellent supervision and support.
- Prof. Dr. Judith Golda, for taking on the role of second supervisor and examiner, for providing me my first teaching opportunities and for her support and advice.
- Oliver Krettek, Neil Unteregge, Sven Weller and Nils Huber, who prepared their bachelor and master theses within this project and contributed to this work. Special thanks go to Oliver, for thoroughly proofreading this thesis.
- The technicians of the Chair of Experimental Physics II, Michael Konkowski, Björn Redeker and Kai Fiegler, for their support with any problems concerning the experimental setups.
- My office mate Sascha Chur, for his support with the XPS measurements, the HiPIMS setup, the assembly of the CV experiment and the fantastic working atmosphere.
- Dr. Gabriel Boitel-Aullen for his support and expertise regarding the electrochemistry measurements.
- Dr. Marina Prenzel, for her support with the XPS measurements and providing her expert opinion on the topic of gardening.
- Dr. Paolo Cignoni for providing the TEM analysis.
- Sabrina Klopsch and Dr. Tim Dirks for their support with the hydrogen peroxide measurements and providing us with deionized water.
- Dr. Steffen Schüttler and Steijn Vervloedt for proofreading this thesis and being wonderful lab neighbours.
- Fatma-Nur Seferoglu for being a great conference roommate and taking care of my many plants when i was on vacation.

- My predecessor Dr. Katharina Laake, for her supervision and support and laying the foundation for this thesis both by her scientific research and organisational talent.
- All members of the Chair of Experimental Physics II and Plasma Interface Physics who always maintained a wonderful atmosphere and work environment.
- Lastly, i want to thank my family and my friends and especially my parents for their support throughout my time as a doctoral student and my entire studies. Thank you for everything! ♡

Curriculum Vitae

Name: Pia-Victoria Pottkämper
Date of Birth: 27.11.1995
Place of Birth: Krefeld, Germany

Higher Education

since 06/2022 PhD Student, Physics
at Ruhr University Bochum
10/2019 - 05/2022 Master of Science, Medical Physics
at Dortmund University
10/2015 - 09/2019 Bachelor of Science, Medical Physics
at Dortmund University

Education

20.06.2015 Abitur
09/2006 - 06/2015 Secondary School, Gesamtschule Kaiserplatz, Krefeld

International Presentations and Conference Participations

07/2025 International Conference on Phenomena in Ionised Gases, Aix en Provence, France, Poster Presentation
05/2024 Frontiers in Low Temperature Plasma Diagnostics, Prague, Czech Republic, Poster Presentation
02/2024 Spring Meeting of the German Physical Society, Greifswald, Germany, Invited Presentation
05/2023 International Symposium on Plasma Chemistry, Kyoto, Japan, Poster Presentation